



This electronic thesis or dissertation has been downloaded from Explore Bristol Research, http://research-information.bristol.ac.uk

Author: Scott, Elliott J

Title: A biologically-inspired artificial lateral line

Observations of collective behaviour in fish lead to the development of a novel design of simple and low-cost artificial lateral line sensor

General rights

Access to the thesis is subject to the Creative Commons Attribution - NonCommercial-No Derivatives 4.0 International Public License. A copy of this may be found at https://creativecommons.org/licenses/by-nc-nd/4.0/legalcode This license sets out your rights and the restrictions that apply to your access to the thesis so it is important you read this before proceeding.

Take down policy

Some pages of this thesis may have been removed for copyright restrictions prior to having it been deposited in Explore Bristol Research. However, if you have discovered material within the thesis that you consider to be unlawful e.g. breaches of copyright (either yours or that of a third party) or any other law, including but not limited to those relating to patent, trademark, confidentiality, data protection, obscenity, defamation, libel, then please contact collections-metadata@bristol.ac.uk and include the following information in your message:

· Your contact details

Bibliographic details for the item, including a URL

• An outline nature of the complaint

Your claim will be investigated and, where appropriate, the item in question will be removed from public view as soon as possible.

A biologically-inspired artificial lateral line

Observations of collective behaviour in fish lead to the development of a novel design of simple and low-cost artificial lateral line sensor

By

Elliott J. Scott



Department of Engineering Mathematics UNIVERSITY OF BRISTOL

A dissertation submitted to the University of Bristol in accordance with the requirements of the degree of DOCTOR OF PHILOSOPHY in the Faculty of Engineering.

JANUARY 2021

Word count: 39211

ABSTRACT

F ish use their lateral line to extract information from the hydrodynamic world around them. The lateral line, comprised of velocity-sensitive superficial neuromasts and acceleration-sensitive canal neuromasts, plays a role in mediating many behaviours, from feeding to shoaling. However, even now, the precise functional mechanisms at work remain unclear. Given the complex, and often cluttered, underwater environment, if we were able to better understand the mechanisms behind this, and emulate such a sense, it could aid underwater vehicles as they traverse the deep.

In this study, 96 cichlid hybrids were bred to generate a spectrum of lateral line characteristics. Cichlids have a relatively recent common ancestor, with species sharing many common traits. The well-developed 'widened' lateral line of the *Aulonocara stuartgranti* was chosen as one extreme of this spectrum and the underdeveloped 'narrow' lateral line of the *Otopharynx lithobates* as the other; the *Aulonocara* has been observed hunting benthic prey using these canals in dimly lit conditions, while the *Otopharynx* is a species that feeds visually in brightly lit environments.

Individuals were placed into a shoal of companion fish and shoaling tendencies were observed in both laminar and turbulent flow. Neuromasts were stained in all individuals and their location and number recorded. Using Generalised Linear Mixed Models (GLMMs), we found individuals with greater numbers of head canal neuromasts or with larger head canal pores tended to swim closer to neighbours while those with greater numbers of head superficial neuromasts swam in looser shoals.

A novel design of bio-inspired sensor that is able to detect a fish-like vortex wake was then created and optimised, both in simulation and experiment. This minimalist sensor is low-cost, low-power, and easy to manufacture, with a number of potential applications including flow monitoring in pipes, supplementary navigation systems in Autonomous Underwater Vehicles (AUVs) or simple flow sensing robots.

ACKNOWLEDGEMENTS

would like to offer my sincerest thanks to:

My supervisors, Sabine Hauert, Christos Ioannou and Martin Genner, for their advice and support throughout my PhD.

Duncan Edgely, for his efforts in CT scanning and morphometrics.

Natalia Gonzalez Cadiente, for her efforts in the design, construction, and testing of the first sensor prototypes.

Bristol Robotics Lab, for their equipment and expertise in all things robotic.

To Alan Smith and Domino Joyce, along with the Hull University aquarium unit, for breeding and raising our hybrids.

The Bristol University Animal Services Unit, and its team, Clare Sims and Peter Gardiner, for their efforts in the care and well-being of our fish.

All reviewers, for their helpful feedback.

Friends and family, for their support throughout.

AUTHOR'S DECLARATION

declare that the work in this dissertation was carried out in accordance with the requirements of the University's Regulations and Code of Practice for Research Degree Programmes and that it has not been submitted for any other academic award. Except where indicated by specific reference in the text, the work is the candidate's own work. Work done in collaboration with, or with the assistance of, others, is indicated as such. Any views expressed in the dissertation are those of the author.

SIGNED: ELLIOTT SCOTT

DATE: 14/04/2021

PUBLICATION STATEMENT

lements of the work contained in this thesis are also present in currently unpublished papers. The two papers are as follows:

"The mechanosensory lateral line mediates collective behaviour in African cichlid fish"

"A simple bio-inspired artificial lateral line sensor for swarming"

The first of the two papers contains material spread across chapter 3: "The creation and characterisation of a new data set" and chapter 4: "The effect of morphology on behaviour". Specifically, it contains the methodology of the experimental design and set-up from the behavioural trials through to the CT scanning, as well as presenting the results from the behavioural trials, the neuromast imaging and the pore morphometrics. It also presents the raincloud plots seen at the end of this chapter.

The second paper contains material from chapter 5: "The design and optimisation of an artificial lateral line sensor". Specifically, it includes the key design elements identified as being important in designing an artificial canal. It presents the results of the optimised sensor and the comparisons other designs. It also presents the work with the physical sensor in the flow tank.

TABLE OF CONTENTS

		P	age
Li	st of	Tables	xiii
Li	st of	Figures	xvii
1	Intr	oduction	1
	1.1	The lateral line	1
	1.2	Shoaling	2
	1.3	Swarms	2
	1.4	Motivation	3
	1.5	Overview	4
	1.6	Contributions	5
2	Stat	e of the Art	7
	2.1	The lateral line	7
		2.1.1 Canal versus superficial neuromasts	8
		2.1.2 The lateral line mediates many behaviours	8
		2.1.3 The lateral line is necessary for accurate control	11
	2.2	A lateral line inspired sensor	14
	2.3	Underwater platforms	30
	2.4	Swarms	31
		2.4.1 Underwater swarms	32
3	The	creation and characterisation of a new data set	35
	3.1	Introduction	35
		3.1.1 Cichlids	35
		3.1.2 Hybrids	36
		3.1.3 The lateral line	36
		3.1.4 Experimental set-up	38
	3.2	Tank design	39
		3.2.1 Tank simulations	40

		3.2.2	Tank construction	42
		3.2.3	Experimental arena	42
	3.3	Tank o	haracterisation	43
		3.3.1	Simulations	43
		3.3.2	Particle Image Velocimetry	45
	3.4	Experi	ment methodology	45
		3.4.1	Housing and maintenance	45
		3.4.2	Experimental conditions	46
		3.4.3	Recording conditions and video analysis	46
		3.4.4	Quantifying behavioral parameters from video	47
		3.4.5	DASPEI staining and lateral line imaging	47
		3.4.6	CT scanning and pore structure analysis	47
	3.5	Experi	ment results	48
		3.5.1	Behaviour	48
		3.5.2	Neuromast Imaging	50
		3.5.3	Pore Structure	50
		3.5.4	Characterisation	50
	3.6	Conclu	sion	52
4			of morphology on behaviour	59
	4.1		uction	59
	4.2		tical Analysis	62
	4.3		cical Analysis Results	65
		4.3.1	Anterior neuromast number and collective behavior covary	65
		4.3.2	Fish with larger anterior canal pores swim closer to their nearest neighbors	
	4.4		of-concept simulations of the canal system	
		4.4.1	Simulating flow behind a cylinder	71
	4.5		in vortex street	72
		4.5.1	Simulating a canal structure and varying pore size	73
	4.6		ation results	73
		4.6.1	Vortex shedding behind a cylinder	73
		4.6.2	Finding the optimum position	77
		4.6.3	Canal structures filter flow information	78
		4.6.4	Canal pore size affects sensitivity	79
	4.7	Conclu	usion	79
5	The	design	and optimisation of an artificial lateral line sensor	81
	5.1	Introd	uction	81
	5.2	0	ising the lateral line	83

TABLE OF CONTENTS

Bi	bliog	raphy		147
D	Арр	endix]	D	145
С	Арр	endix	C	141
В	Арр	endix]	В	115
A	Арр	endix .	Α	111
	6.5	Future	e work	108
	6.4	-	ising the sensor	
	6.3		ning an artificial lateral line	
	6.2		ling relationships	
		6.1.3	CT scanning and morphometrics	106
		6.1.2	DASPEI staining and photography	106
		6.1.1	Flow tank and shoaling	105
	6.1	Biolog	ical experiments	105
6	Con	clusio	18	105
	5.5	Conclu	ision	103
		5.4.1	Experimental results	100
	5.4	Artific	ial lateral line production and testing	97
		5.3.5	Sensor operational envelope	
		5.3.4	Further spaced pores result in less interference	
		5.3.3	Rear facing pores reduce noise	91
		5.3.2	Fixed diameter internal channels prevent internal turbulence	
	0.0	5.3.1	Verifying the design	
	5.3		isation results	
		5.2.1 5.2.2	Simulation-based experiments	
		5.2.1	Artificial lateral line design	84

LIST OF TABLES

Тав	LE Page
3.1	The mean and standard deviation of the behavioural variables for all study individuals and for each of the groups
3.2	The mean and standard deviation of the neuromast variables for all study individuals and for each of the groups. 49
3.3	The mean and standard deviation of the pore structure variables for all study individ- uals and for each of the groups
B.1	Model comparisons using the Akaike Information Criterion scores for neuromast models that explain variability in mean nearest neighbour distance, for the dataset that includes all individuals (hybrids and parent species), where total body length is included as a covariate term in all models
B.2	Model comparisons using the Akaike Information Criterion scores for neuromast models that explain variability in mean nearest neighbour distance, for the dataset that includes only hybrids, where total body length is included as a covariate term in all models
B.3	Model comparisons using the Akaike Information Criterion scores for neuromast models that explain variability in mean group radius, for the dataset that includes all individuals (hybrids and parent species), where total body length is included as a covariate term in all models
B.4	Model comparisons using the Akaike Information Criterion scores for neuromast models that explain variability in mean group radius, for the dataset that includes only hybrids, where total body length is included as a covariate term in all models 119
B.5	Model comparisons using the Akaike Information Criterion scores for neuromast models that explain variability in mean distance to nearest upstream neighbour, for the dataset that includes all individuals (hybrids and parent species), where total body length is included as a covariate term in all models

B.6	Model comparisons using the Akaike Information Criterion scores for neuromast models that explain variability in mean distance to nearest upstream neighbour, for the dataset that includes only hybrids, where total body length is included as a covariate term in all models.	121
B.7	Model comparisons using the Akaike Information Criterion scores for neuromast models that explain variability in mean distance to nearest neighbour in 'field of flow detection', for the dataset that includes all individuals (hybrids and parent species), where total body length is included as a covariate term in all models	122
B.8	Model comparisons using the Akaike Information Criterion scores for neuromast models that explain variability in mean distance to nearest neighbour in 'field of flow detection', for the dataset that includes only hybrids, where total body length is included as a covariate term in all models	123
B.9	Model comparisons using the Akaike Information Criterion scores for neuromast models that explain variability in mean nearest neighbour distance, for the dataset that all individuals (hybrids and parent species). Total body length is only considered as a stand-alone main effect.	124
B.10	Model comparisons using the Akaike Information Criterion scores for neuromast models that explain variability in mean nearest neighbour distance radius, for the dataset that includes only hybrids. Total body length is only considered as a stand- alone main effect.	125
B.11	Model comparisons using the Akaike Information Criterion scores for neuromast models that explain variability in mean group radius, for the dataset that includes all individuals (hybrids and parent species). Total body length is only considered as a stand-alone main effect.	126
B.12	Model comparisons using the Akaike Information Criterion scores for neuromast models that explain variability in mean group radius, for the dataset that includes only hybrids. Total body length is only considered as a stand-alone main effect	127
B.13	Model comparisons using the Akaike Information Criterion scores for pore size models that explain variability in mean nearest neighbour distance, for the dataset that includes all individuals (hybrids and parent species), where total body length is included as a covariate term in all models.	128
B.14	Model comparisons using the Akaike Information Criterion scores for pore size models that explain variability in mean nearest neighbour distance, for the dataset that includes only hybrids, where total body length is included as a covariate term in all models	129

B.15	Model comparisons using the Akaike Information Criterion scores for pore size models	
	that explain variability in mean group radius, for the dataset that includes all individ-	
	uals (hybrids and parent species), where total body length is included as a covariate	
	term in all models	130
B.16	Model comparisons using the Akaike Information Criterion scores for pore size models	
	that explain variability in mean group radius, for the dataset that includes only	
	hybrids, where total body length is included as a covariate term in all models.	131
B.17	Model comparisons using the Akaike Information Criterion scores for pore size models	
	that explain variability in mean distance to nearest upstream neighbour, for the	
	dataset that includes all individuals (hybrids and parent species), where total body	
	length is included as a covariate term in all models.	132
B.18	Model comparisons using the Akaike Information Criterion scores for pore size models	
	that explain variability in mean distance to nearest upstream neighbour, for the	
	dataset that includes only hybrids, where total body length is included as a covariate	
	term in all models	133
B.19	Model comparisons using the Akaike Information Criterion scores for pore size models	
	that explain variability in mean distance to nearest neighbour in 'field of flow detection'	
	, for the dataset that includes all individuals (hybrids and parent species), where total	
	body length is included as a covariate term in all models	134
B.20	Model comparisons using the Akaike Information Criterion scores for pore size models	
	that explain variability in mean distance to nearest neighbour in 'field of flow detec-	
	tion', for the dataset that includes only hybrids, where total body length is included as	
	a covariate term in all models	135
B.21	Model comparisons using the Akaike Information Criterion scores for pore size models	
	that explain variability in mean nearest neighbour distance, for the dataset that all	
	individuals (hybrids and parent species). Total body length is only considered as a	
	stand-alone main effect.	136
B.22	Model comparisons using the Akaike Information Criterion scores for pore size models	
	that explain variability in mean nearest neighbour distance, for the dataset that	
	includes only hybrids. Total body length is only considered as a stand-alone main effect.	137
B.23	Model comparisons using the Akaike Information Criterion scores for pore size mod-	
	els that explain variability in mean group radius, for the dataset that includes all	
	individuals (hybrids and parent species). Total body length is only considered as a	
	stand-alone main effect.	138
B.24	Model comparisons using the Akaike Information Criterion scores for pore size models	
	that explain variability in mean group radius, for the dataset that includes only	
	hybrids. Total body length is only considered as a stand-alone main effect	139

LIST OF FIGURES

FIGURE

Page

37

38

- The process by which hybridisation results in a range of characteristics. Individual 1 3.1has genes that express as expanded pores and expanded canals, while individual 2 has genes that express as narrow pores and narrow canals. Individuals in generation 1 (the middle row) will receive half of the genes for pore (1) and canal (2) size from one parent and half from the other, resulting in all of them possessing genes for both expanded and narrow pores and expanded and narrow canals. This will typically result in pores and canals that are intermediate between the extremes. The subsequent generation however will then have every combination of the available genes, resulting in some individuals with expanded pores and expanded canals, some with narrow pores and narrow canals, some with expanded pores but narrow canals, and some with narrow pores but expanded canals. A further 12 combinations exist than what are shown in the bottom row, which include combinations such as intermediate pore size and expanded canals, or narrow pore size and intermediate canal size. In this way, a wide range of lateral line morphologies will be seen in the second generation hybrids. In reality, the morphology of the lateral line is affected by more than just two gene pairs, and so significantly more combinations will exist and therefore much more 3.2
- 3.2 Differences in lateral line morphology of the parent species. (a) The morphology of the *Otopharynx lithobates*, showing reduced pore size and reduced visibility of canal neuromasts. (b) The morphology of the *Aulonocara stuartgranti*, showing larger pore size and increased visibility of canal neuromasts. (c) Comparisons of the relative mandibular pore areas of 53 species of cichlids, with the relative location of the *Otopharynx* highlighted in blue and the relative location of the *Aulonocara* shown in red. Jitter is added in the y axis to prevent excessive overlap of points. Data for this graph is taken from Edgely *et al.* [49].
- 3.3 Differences in laminar and turbulent flow. a) Graphical representation of laminar flow, showing straight streamlines and no rotational motions. b) Graphical representation of turbulent flow, showing the rotational motions in the water and the formation of eddies and vortices.
 40

- 3.6 Tests of the experimental area of the flow tank. (a) Simulated predictions of laminar flow in the test area, k = 0.25617. (b) Simulated predictions of the turbulent flow in the test area, k = 0.30121. (c) A still from footage of an experimental PIV test of laminar flow in the test area, where particles appear to be moving relatively smoothly downstream. (d) A still from footage of an experimental PIV test of turbulent flow in the test area, where the swirl patterns in the particles seem to indicate vortices present. 44
- 3.8 Behavioural data for each of the individuals in the study, organised into groups based on species for (a) The mean nearest neighbour distance. (b) The mean group radius. (c) The mean distance to nearest upstream neighbour. (d) The mean distance to nearest neighbour within the flow detection field. Graphs here use data from both laminar and turbulent trials. The raincloud plots consist of a probability density function (top in light grey), a boxplot (central in black) and a jittered scatter plot using the raw data (bottom in colour).

55

56

57

61

- 3.9 Superficial neuromast data for each of the individuals in the study, organised into groups based on species for (a) The number of anterior superficial neuromasts. (b) The number of posterior superficial neuromasts. (c) The number of lower posterior superficial neuromasts. (d) The number of tail neuromasts. Graphs here use data only from the laminar trials; turbulent trials are not included to avoid duplicate results. The raincloud plots consist of a probability density function (top in light grey), a boxplot (central in black) and a jittered scatter plot using the raw data (bottom in colour).
- 3.10 Canal neuromast data for each of the individuals in the study, organised into groups based on species for (a) The number of anterior canal neuromasts. (b) The number of posterior canal neuromasts. (c) The number of lower posterior canal neuromasts. Graphs here use data only from the laminar trials; turbulent trials are not included to avoid duplicate results. The raincloud plots consist of a probability density function (top in light grey), a boxplot (central in black) and a jittered scatter plot using the raw data (bottom in colour).
- 3.11 Pore size data for each of the individuals in the study, organised into groups based on species for (a) The mean size of the pores in the otic lateral line. (b) The mean size of the pores in the orbital lateral line. (c) The mean size of the pores in the mandibular lateral line. (d) The mean size of the pores in the preopercular lateral line. Graphs here use data only from the laminar trials; turbulent trials are not included to avoid duplicate results. The raincloud plots consist of a probability density function (top in light grey), a boxplot (central in black) and a jittered scatter plot using the raw data (bottom in colour).
- 4.1 Schematic diagram summarizing the different elements of the study: (a) Group of fish shedding vortices with the response variables used in the experiment marked (nearest neighbor distance and group radius). (b) Response of superficial and canal neuromasts to a vortex when in the presence of background flow. The superficial neuromast is saturated by background flow, whereas the canal neuromast is unaffected by the background flow. The canal structure filters out any background laminar flow (pale grey lines) while allowing turbulent flows like shed vortices to be detected more clearly. (c) A cylinder can be used to generate vortices (approximate to those generated by an upstream fish, albeit in different positions), and an artificial canal structure containing an artificial neuromast can detect them.

- 4.2 The output of a GLMM when computed and called in R (version 3.6.1 [146]). The first shows the formula used; next is the AIC score; the 'coefficients' section gives the contribution that each of the different terms has on the final model, where scale() terms affect the slope and all other terms affect the intercept position; the following section shows the effect of the random term(s); the negative binomial dispersion parameter is next and measures how much the model fluctuates around a mean value; finally, the log-likelihood value is shown, which gives an estimate of the goodness of fit. 64
- 4.4 The best supported associations between the behavioural variables and the morphological variables pertaining to the visible neuromast counts: (a) the effect of number of visible anterior superficial neuromasts on the group radius and (b) the effect of the number of visible anterior canal neuromasts on the mean nearest neighbour distance. In both, *Otopharynx lithobates* is shown by blue crosses, *Aulonocara stuartgranti* is shown by black pluses, and the hybrids are shown by red dots. The black line shows the line of fit for the entire data set, while the red line shows the line of fit for a data set of only hybrid individuals.
- 4.5 The best supported associations between the behavioural variables and the morphological variables pertaining to the pore size: the effect of the size of the otic canal pores on the mean nearest neighbour distance. *Otopharynx lithobates* is shown by blue crosses, *Aulonocara stuartgranti* is shown by black pluses, and the hybrids are shown by red dots. The black line shows the line of fit for the entire data set, while the red line shows the line of fit for a data set of only hybrid individuals. 70

- 4.8 Simulated flow behind different cylinders at 0.5m/s, with glyphs showing the flow velocities and contour lines showing the different pressure levels. a) Simulation of a cylinder with diameter 50mm. b) Simulation of a cylinder with diameter 150mm.

4.9	Simulated flow behind cylinders with 100m diameter at different speeds, with glyphs	
	showing the flow velocities and contour lines showing the different pressure levels. a) Simulation of a cylinder at flow speed 0.1m/s. b) Simulation of a cylinder at flow speed	
	1m/s	76
4.10	The variation in x velocities surrounding a cylinder with 0.1m diameter in flow at	
	0.5m/s. Blue dots represent the minimum level of variation and red dots represent the	
	maximum variation. Variation is taken over the entire 400 second simulation.	78
4.11	A comparison of the velocities experienced in open flow and within the 20mm pore size	
	prototype. Diagrammatic representations of a neuromast in the different locations are	
	included for context. The resulting waveforms show the changes in velocity over the	
	full 400 seconds of the simulation. Both simulations have freestream velocity set to	
	0.5m/s	79
4.12	Violin plots of the velocity that was recorded within the prototype at each of the	
	different pore sizes tested, where the 'Open pore' indicates that the entire pore-side	
	face is removed and is meant to represent an infinitely large pore size. Freestream	
	flow velocity was set at 0.5m/s for all cases. Data is extracted at the point where flow	
	is reversed and so a greater response is measured with a greater negative velocity.	
	A violin plot consists of a vertically oriented probability density function (mirrored	
	around the centreline) and a boxplot, with the white dot giving the median, the thick	
	black bar giving the interquartile range and the full length of the bar giving the total	
	range	80
5.1	Graphical representation of a lateral line system in teleost fish.	84
5.2	Artificial lateral line sensor design and mechanism. (a) CAD design of the artificial	
	lateral line sensor. The sensor has two pores, a cylindrical canal of 15mm diameter,	
	and an artificial neuromast positioned 10mm from the pore on the shorter side. (b)	
	Artificial lateral line mechanism capturing shed vortices on the neuromast while	
	filtering water flow. Flow is accelerated out of the sensor when the negative pressure	
	at the centre of the vortex causes a pressure differential with the neutral pressure in	
	the long section of canal.	85
5.3	Simulated environment in OpenFOAM, including the 100mm diameter cylinder that	
	generates the vortices and our optimised sensor design.	86
5.4	The iterative process that the sensor went through to arrive at the final optimised	
	design	87
5.5	A graphical representation of the different mechanisms that affect how a passing	
	vortex is detected. Black arrows show motion in and out of the sensor due to sur-	
	rounding fluid motion, while blue arrows show motion in and out of the sensor due to	
	surrounding fluid pressures. (a)-(c) show the time progression of a vortex passing the	
	prototype detailed in Chapter 4, while (d)-(f) show the same for the optimised sensor.	88

5.6	Comparisons between the velocities detected by the optimised sensor design (red) and the expected velocities (black) without the sensor present in simulation. a) The	
	time-series b) The normalised time-series	90
5.7	Impact of canal shape on sensory readout. (a) Comparisons between the (a) time-series and (b) normalised time-series detected by the optimised sensor design (red) and the square canal design (blue) against the original time-series (black) in the simulation. (c) The optimised sensor, with residual error between the detected and expected time- series equal to 0.0155. (d) The design with a square canal, with residual error between the detected and expected time-series equal to 0.0214	91
5.8	Impact of canal shape on sensory readout. (a) Comparisons between the (a) time-series	
	and (b) normalised time-series detected by the optimised sensor design (red), the forward-facing pore design (blue) and the side-facing pore design (green) against the original time-series (black) in the simulation. (c) The optimised sensor, with residual error between the detected and expected time-series equal to 0.0155. (d) The forward-facing pore design, with residual error between the detected and expected time-series equal to 0.0199. (e) The side-facing pore design, with residual error between the	92
5.9	Impact of canal shape on sensory readout. (a) Comparisons between the (a) time- series and (b) normalised time-series detected by the optimised sensor design (red), the narrowly spaced pore design (green) and the widely spaced pore design (blue) against the original time-series (black) in the simulation. (c) The optimised sensor, with residual error between the detected and expected time-series equal to 0.0155. (d) The narrowly spaced pore design, with residual error between the detected and expected time-series equal to 0.0195. (e) The widely spaced pore design, with residual error between the detected and expected time-series equal to 0.0216	93
5.10	Comparisons between the time-series detected by the optimised sensor design (red) and the original waveform expected (black) in simulation, both normalised, at a) flow speed at 0.1m/s, with total residuals calculated at 0.0243 b) flow speed at 1 m/s, with	
	total residuals calculated at 0.0178	94
5.11	Comparisons between normalised time-series detected by the optimised sensor design (red) and the original waveform expected (black) in simulation. a) channel diameter at 10mm and at 0.1m/s, total residuals = 0.0210 b) channel diameter at 20mm and 0.1m/s, total residuals = 0.0206 (c) channel diameter at 10mm, total residuals = 0.0193. (d) channel diameter at 20mm, total residuals = 0.0213 (e) channel diameter at 10mm and at 1m/s, total residuals = 0.0189 (f) channel diameter a 20mm and at 1m/s, total residuals = 0.0191	96
5.12	3D printed physical sensor, with the elastic skin (red), artificial neuromast, and	
	corresponding visual tracker (black)	98

5.13	The custom built tank used for the sensor flow experiments. Tank walls were made of twin-wall polycarbonate sheeting, that was attached together using duct tape and silicone sealant. A thick plastic board with holes drilled in was used to cover the exit. These holes were covered to allow the resevoir to fill and then uncovered to allow water to flow through the test area. This set-up was used in a home environment during the Covid-19 pandemic.	99
5.14	3 still images taken from a video of the sensor being moved in static water to demon- strate the filtering effect of the sensor. Time progresses from the initial frame of the video (a) to the final frame of the video (c). A ruler is included in the background to better illustrate the motion of the sensor. The final position of the visual tracker is 8mm further forward than the starting position, but this can be attributed to parallax, because firstly, the tracker moves forward into the flow which it would not do if it was being affected by the sensor movement, and secondly, it does not return its (neutral) starting position, which it would do if the motion was being caused by negative pres- sure at the mouth of the sensor. Additionally, the apparent distance between the top and bottom edges of the mouth of the sensor go from 0mm to 4mm	100
5.15	4 still images taken from a video demonstrating the sensor's ability to detect passing vortices. Time progresses from (a) to (d). Each still image has a zoomed in call out showing the deflection of the neuromast at that time. As the cylinder passes in (c), there is a deflection of 1cm (from 1 to 0 on the markings above), before the tracker returns to 1 again in (d).	101
5.16	Breakdown of the experimental set-up used in the custom flow tank that was used to test for the ability of the sensor to detect shed vortices. Vortices are shed upstream by the black cylinder (Approximately 10cm diameter) Red circles mark the locations at which the sensor was positioned. Flow moves from left to right.	102
5.17	Results from the video analysis of the sensor response. Letter labels in this diagram correspond to the letter labelled positions seen in Fig. 5.16, such that results from the sensor being in position (a) correspond to the graph here labelled (a), etc. Each graph shows the response of the visual tracker to a passing vortex over 3 separate trials	103
5.18	The average of the deflection across the three trials	104
A.1	The associations between body length and the different canal neuromast morphological variables: the number of anterior canal neuromasts, the number of posterior canal neuromasts and the number of lower posterior canal neuromasts (below/left of variable histogram), and the associated Spearman's rank correlation coefficient (above/right of variable histogram).	111

- A.2 The associations between body length and the different superficial neuromast morphological variables : the number of anterior superficial neuromasts, the number posterior superficial neuromasts, the number of lower posterior superficial neuromasts and the number of tail neuromasts (below/left of variable histogram), and the associated Spearman's rank correlation coefficient (above/right) of variable histogram). 112

- C.3 Simulated flow behind a cylinder with 100mm diameter at 1m/s, with glyphs showing the flow velocities and contour lines showing the different pressure levels. 142
- C.4 Simulated flow behind a cylinder with 150 mm diameter at 0.5 m/s, with glyphs showing the flow velocities and contour lines showing the different pressure levels. 143
- C.6 Simulated flow behind a cylinder with 150mm diameter at 0.5m/s, with glyphs showing the flow velocities and contour lines showing the different pressure levels. 144
- D.1 Preliminary CAD design showing (a) an enclosure containing an elastic and conductive haircell and bearing strips of wiring embedded in one wall and (b) the haircell deflecting in response to a flow stimuli affecting its other end (not pictured) and being pressed against the strips of wiring. This action then complets the circuit and allows resistance to be measured, with that being dependent on how many strips of wiring in the wall the haircell crosses.
 D.2 Deliminary CAD design showing (a) an enclosure containing an elastic and conductive haircell crosses.



INTRODUCTION

F ish, and some other aquatic animals, possess a remarkable ability that is not seen in the terrestrial world [42, 194]: a series of specialised, hair-like cells allows them to extract and interpret hydrodynamic data from the surrounding water [45, 99]. This sense is sophisticated enough that it is effective in both turbulent flows [102, 199] and without the need for visual input, with studies showing this across a multitude of species [20, 33, 80, 83, 106, 136, 142, 152, 163–167]. In fact, some species have done away with vision altogether, relying solely on the lateral line for navigation [83, 106, 175]. Naturally, such a powerful sense plays a huge role in the lives of aquatic individuals, influencing critical behaviours such as shoaling [55, 136, 142] and feeding [33, 69, 80, 81, 106, 126, 128, 152, 163–167]. We can take inspiration from the mechanisms involved in locating prey [43, 88, 163, 165] to aid underwater vehicles that are tasked with locating certain types of object [4, 6, 54, 63, 71, 83, 94, 207]. Understanding and emulating the aspects of the lateral line that mediate shoaling behaviour can help in giving the field of underwater swarm robotics new options for control [82, 211], options that are both simpler and more robust.

1.1 The lateral line

The lateral line is a body wide sensory organ found in most fishes, and is comprised of superficial and canal neuromasts. Superficial neuromasts are located on the skin of the fish, while canal neuromasts are found in hollow structures, called canals, beneath the skin. The canal structures run throughout the head of the fish and down the side of the trunk as well [17, 42, 45, 69, 99, 162]. The neuromasts themselves are hair-like structures that move in response to flows, with the superficial neuromasts being more sensitive to flow velocities and the canal neuromasts being more sensitive to flow velocities and the canal neuromasts being more sensitive to flow structures [45, 99, 190, 194]. The lateral line has been shown to be

essential for accurate control of shoaling behaviours [55, 136, 142], and this is one of the main drivers behind this project's desire to better understand its precise role in this, as well as the attempts to emulate it for robotic swarm sensing.

1.2 Shoaling

Shoaling is a behaviour that the majority of teleost fishes will exhibit over the course of their lifetimes [143, 144, 169]. A shoal is defined by Pitcher as '...a group of fish that remains together for social reasons.' [143] and there are significant benefits to be gained from shoaling and other similar collective behaviours. Studies have shown that all individuals experience reduced energy costs in a shoal, regardless of position [58, 115]. It has also been shown that shoaling has antipredation benefits [74, 151] and that the turbulence generated in a shoal can even help when it comes to foraging [199]. Applying these benefits to underwater robots has so far proved difficult however, due to the salt water medium's low optical transparency interfering with signals across the light spectrum, making visual navigation difficult, and preventing the transmission of microand radio wave signals for communication [133]. The addition of an artificial lateral line system can overcome these issues. If the technology were to advance far enough, it could even allow for a swarm of simple robots that relies solely on an artificial lateral line system.

1.3 Swarms

In a robotics context, swarming can be seen as using large numbers of simple robots to generate a desired behaviour on a global scale. The desired behaviour can take a range of forms across a range of different scales, from tiny engineered nanoparticles whose collective actions can help to fight cancer [67] to the new global Starlink constellation of satellites. In both cases, a single one of the base units in each of these systems would be ineffective on its own. In the former example, the particles must be nano-scale because of the scale of systems within the body, but millions and millions of these nanoparticles are required before a sufficient level of coverage can be achieved to produce the desired effect. In the latter, a single satellite will never have the field of view needed to provide its services globally. In both cases, system failure can have catastrophic effect, and so the presence of large numbers of each unit also provides the system with improved resilience. Hence, we see the power of swarms.

In his review, Brambilla defines swarm robotics as a bio-inspired approach to collective robotics, based on the behaviours seen in self-organising social animals [27]. Typically, the goal is a robust, scalable and flexible way to organise any number of robots through the use of:

Simple agents

A focus on simple agents makes the swarm more scalable and robust. The easier an agent is to mass produce, the easier it is make more agents and to replace any that become compromised.

Another element of simple agents lies in keeping the swarm itself simple through homogeneity. If every agent is the same, this again makes the swarm more easily mass produced, as well as reducing the complexity required for the control algorithms. It also allows for any swarm member to take on the role of another if required.

• Large numbers of agents

Having large numbers of agents gives a swarm benefits in parallel processing power and sensing. Allowing multiple agents to tackle the same problem can result in faster completion, allow exploration of a larger area, create the potential for multiple different viewpoints, or solve problems that would be impossible for an individual, or small group. It also gives swarms improved fault tolerance, as losing one agent from a swarm of 100 does not significantly detract from its ability to perform a function.

• Local information

Keeping the amount of information that an agent has to process to a minimum helps to keep agents simple. Relying solely on local information and communication also removes the need for a central processing point, which increases the swarm's robustness as there is no single point required to maintain functionality. It also allows for unlimited scalability, as there are no computational or logistical limitations that having all information flow through a central hub would impose, and given that individuals are only aware of a limited area around themselves, the total size of the swarm is not a factor.

As mentioned above, swarm robotics seeks to take inspiration from the natural world, and in fact a few underwater robot swarms do exist [65, 76, 134, 160, 161], and while some of these do take inspiration from nature in their control mechanisms, there has yet to be a swarm that combines both the physical design and the control elements found in fish shoals. Creating a simple and robust artificial lateral line sensor will be a good first step in making that happen.

1.4 Motivation

The overall motivation for this project was the creation of a minimalist and bio-inspired underwater flow sensor that could then be used in simple and low-cost robots for shoaling. The ability that fish have to sense and react to minute changes in water pressure and flow around them is far beyond anything that humanity has been able to replicate thus far. Additionally, the behaviour that actually governs how individuals interact is still not completely understood. The aim of this research was to study the morphology and collective behaviour of fish to generate an extensive database of information about the lateral line and potential associated behaviours; this was to better understand their lateral line morphology and to explore the effect that variation within the lateral line has on interactions between individuals. This work was done with the intention of developing a novel design of flow sensor, inspired by the lateral line, that was simple and easy to mass produce. In the future, robots would then perform simple swarm tasks using only this artificial lateral line sensor and the information it can glean from the local hydrodynamics. It is hoped that such a swarm would be able to demonstrate basic formation control and following functions using said sensors and be able to locate a flow stimulus. A simple, low-cost swarm like this would be useful for environmental monitoring tasks, where large areas need to be surveyed for long periods of time, due to the ease with which many units can be deployed and the low power requirements of a passive artificial lateral line sensor or for tasks with more difficult conditions, such as in dark, turbid or turbulent waters, where hydrodynamic data is more useful than optical. Additionally, this artificial lateral line sensor on its own may have other benefits commercially, as they could be used to monitor flow within difficult to access pipes for irregularities, potentially saving time and money on repair works.

1.5 Overview

In the coming chapters I will:

• State-of-the-Art:

Review the available literature on lateral line morphology and associated behavioural experiments, on artificial lateral line development and deployment, and finally on underwater swarm robotics and the current existing swarms.

• Hybrid data generation and characterisation

Detail the generation of a rich, new, open database containing information about the lateral line morphology of 96 hybrid cichlids and a sample of their parent species, with associated behavioural data captured from within a custom built flow tank, along with proof of concept figures showing the spread of both morphological and behavioural characteristics seen within the hybrids.

• Shoaling experimental work

Analyse the relationships between the morphology and the behaviour seen in the hybrid and parent groups through the use of generalised linear mixed models and investigate, in simulation, the ability of a canal structure to filter background flow and the effect that varying pore size has on ability to detect a fish-like wake of shed vortices.

Sensor development and testing

Identify the key design elements required to effectively optimise a sensor using the groundwork described in the previous chapter, and demonstrate the improvements that follow, both in simulation and then experimentally, with a 3D printed sensor and another custom built flow tank. • Discussion, future work and conclusions Discuss the work that has been done, note significant achievements, comment on directions the project could take next, and make concluding remarks.

1.6 Contributions

The key contributions made by this thesis are as follows:

- Generated a new and comprehensive data set containing lateral line morphology and collective behaviour information from 96 F2 hybrids (*Aulonocara stuartgranti* X *Otopharynx lithobates*) and 10 each of the two parent species. Data was collected through behavioural experiments in a flow tank, through neuromast staining with DASPEI dye and through microCT scanning. The dataset exhibits a significant amount of variation and is a useful resource in the study of morphology and behaviour. Dataset will be available on Dryad.
- Identified relationships between morphology and behaviour, namely that having increased numbers of visible anterior canal neuromasts tend to result in an individual swimming closer to its neighbour, that increased numbers of visible anterior superficial neuromasts tend to lead to looser groups, and that larger canal pore openings also tend to result in swimming closer to a neighbour. This expands upon previous work identifying the importance of the lateral line in mediating shoaling behaviours [55, 136, 142], and begins to explore the more novel territory of attempting to associate different regions of the lateral line with specific behaviours. So far, this has only seen associations being drawn between the mandibular pores and feeding behaviours [49, 92, 163–166].
- Identified key design elements that make a simple, macro-scale artificial lateral line system effective and designed and optimised a novel type of minimalist artificial lateral line sensor that is shown to be able to detect shed vortices akin to those generated by a swimming fish, both in simulation and experimentally. This marks a move towards an artificial lateral line system that is more easily mass produced than its predecessors, which until now have used complex manufacturing processes to develop sensing systems that are both bio-mimetic and at the same scales as seen in biological systems [54, 63, 71, 84, 94, 207]. Such a move is an important step in being able to make artificial lateral line sensors commonplace in the field of underwater swarm robotics.



STATE OF THE ART

any of the problems we face today have been faced by organisms in the past who have already successfully evolved effective solutions, solutions that we can emulate. Take, for example, the problems associated with underwater exploration, and the multitude of ways that fish have evolved to deal with them. Such adaptations include modified eyes for increased light collection, bodily changes to deal with the increased pressure, swim bladders to control buoyancy and the development of the octavo-lateralis senses. Two additional senses exist in fishes, the first is electroreception, the detection of the weak electric fields that every living creature emits constantly, and the other is the lateral line.

2.1 The lateral line

The lateral line system is a body-wide sensory organ that can detect changes in the surrounding water pressure to give an individual an awareness of the hydrodynamic environment around it. The sensory unit of the lateral line is called a neuromast, comprised of a patch of hair cells, support cells and a cupula, or gel-structure. These neuromasts are found in one of two sub-systems: the skin-based superficial neuromast system and the sub-dermal canal neuromast system, both of which run all over the head and trunk of most species of fish. The canal systems are a series of hollow fluid-filled structures that exist beneath the skin, with a series of membrane covered openings, called pores, through which flow information is transmitted. Canal neuromasts are spread throughout here [17, 42, 69, 162, 194]. The different sub-systems do seem to have different modalities, with the superficial neuromasts being stimulated by flow velocities, and the canal neuromasts being stimulated by flow accelerations [99].

2.1.1 Canal versus superficial neuromasts

Kroese and Schellart used a vibrating sphere to generate sinusoidal water motion in an attempt to determine if the afferents (nerves that carry signals towards the brain) in the lateral line of a rainbow trout, *Oncorhynchus mykiss*, respond differently. It was found that there were two groups of afferents which responded with differing levels of sensitivity to different frequency ranges. They concluded that the afferents that responded to low-frequency water motions enervated the superficial neuromasts while the group that responded to high-frequency water motions enervated the canal neuromasts. They further conclude that this makes the canal neuromasts sensitive to water accelerations, and the superficial neuromasts sensitive to water velocities [99]

Voigt *et al.* performed similar work, testing the afferents associated with neuromasts all over the body of an eel (*Anguilla dieffenbachia*) and found that a number of them have a linear response to increasing flow speed when angled to be facing directly into the flow, while a number of others had no significant response to changes in flow. They similarly concluded that the former class were likely to be for the surface neuromasts while the latter enervated the canal neuromasts [190].

Further investigations in this vein compared differences in the still water fish *Carassius auratus* and the riverine fish *Oncorhyncus mykiss*. A vibrating sphere was used to test the responses of the different nerve fibres in running water, and it was found again that type 1 fibres are stimulated by flowing water, but type 2 fibres were not. Type 1 fibres were unable to detect the sphere due to the stimulation of the running water, while the type 2 fibres were able to [53].

As is to be expected, there is much variation in the lateral line between species: the more easily overloaded superficial neuromasts are less present in those fish that live in fast flowing water, as they are less useful here, whereas those fish living in calmer waters have more. Fish in fast-flowing water also have typically narrower canals to better filter information, while wider canals are present in stiller waters [123]. Deep-sea fish take this to a further extreme, with very wide canals with only a membranous cover, as well as having a great deal of superficial neuromasts, some even on specialist papillae [125]. The still waters of the deep mean that there is little need to filter out the low frequency signals; these adaptations allow the individual to optimise the way that they can detect and interpret signals given the 'noise' of their environment [123, 125].

Studies on the common bully (*Gobiomorphus cotidianus*) reveal similar results: the high number of superficial neuromasts found on this still water living species were sensitive to a vibrating sphere when in still water, however, with increasing flow velocities, the sensitivity to the sphere decreased significantly [15].

2.1.2 The lateral line mediates many behaviours

The superficial neuromasts are mostly associated with behaviours that monitor and react to surrounding background flows, such as station holding in steady flow or rheotaxis [41, 99, 178,

190].

Rheotaxis is the tendency of fish in flow to face into the current and is considered a behaviour for energy conservation. The importance of the superficial neuromasts in mediating this behaviour was demonstrated experimentally by Montgomery *et al.*: three diverse species of fish *(Cheimarrichthys fosteri, Pagothenia borchgrevinki & Astyanax fasciatus)* were subjected to a variety of chemical and physical treatments to disable aspects of the lateral line system to study the effect that this would have on the fish's ability to maintain rheotaxis [127]. It was shown that without an intact lateral line, there was a marked increase in the flow threshold after which rheotactic behaviour would start to take place. Additional chemical treatments were used to damage canal neuromasts while leaving superficial ones intact, and in this case rheotactic behaviour [127]. This was again demonstrated in an Antarctic fish, *Pagothenia borchgrevinki*, where the same process of disabling the entire lateral line or just the superficial neuromasts causes a significant rise in the speed at which rheotaxis begins to take place versus just the canal neuromasts where there is no effect [13].

Further work on rheotaxis has been done more recently by Elder and Coombs in which the Mexican tetra (*Astyanax mexicanus*), a stream-dwelling species, was placed into uniform and turbulent flow conditions. Some subjects were visually deprived, while others were deprived of their lateral line; a third group was given access to information from both sensory systems. It was seen that turbulence lowers the threshold at which rheotactic behaviours begin to appear in all groups. Fish without access to visual information were seen to lose the accuracy with which they were able to orient themselves facing upstream, while, interestingly, those that lost the information from their lateral line exhibited no measurable detriment. This study concludes that rheotactic abilities are still present, even in the absence of lateral line and vision, in both turbulent and non-turbulent flows [51].

The subdermal canals are used to detect the turbulent flows that might be generated by other animals, such as during predation when they are used independently to detect a punctuate vibrating stimulus. This was demonstrated in an experiment that used mottled sculpin (*Cottus bairdi*) that had had either their canal or superficial neuromasts disabled [41]. Their responses to a vibrating sphere were tested and those fish whose canal neuromasts remained intact were able to orient themselves towards the source [41]. Further work involved mottled sculpin that had been surgically blinded that were then placed into a tank where flow was slowly introduced [88]. All fish began to exhibit rheotaxis after a threshold flow speed. Further to this, an artificial prey item, a periodically vibrating sphere, was introduced upstream and feeding responses were recorded. It was shown that even very weak oscillating signals, generated by the artificial prey item, can be detected in strong uniform flows, which follows the idea that the canals act as a filter to the low-frequency background flows, allowing the subdermal canals to detect high-frequency turbulent flows [88]. For wake following behaviours or for station holding in a more turbulent

flow then information from both sub-systems are required. Rainbow trout (*Oncorhynchus mykiss*) were subjected to one of several chemical treatments that either disabled the head canal lateral line system, the trunk canal lateral line system or the superficial neuromasts and were then placed in a flow containing an object. The amount of time that the trout spent station-keeping behind that object, known as entraining, was recorded and it was shown that fish that were not treated spent significantly more time entraining than those that were, and that between the treated groups there was no significant difference [124].

The lateral line also has the ability to detect flow fields around objects. Determining the precise meaning of the signals detected can be very helpful in understanding the surrounding environment and locating a signal's source. Curcic-Blake and van Netten used a vibrating sphere to test the lateral line's ability to detect and locate stimuli. The sphere was placed in a variety of positions around a fish (Ruffe, *Gymnocephalus cernuus* L.) and neural responses were measured. It was found that the experimental results matched very closely with the predicted results and that the greatest response occurred when the vibrating sphere was directly next to, i.e. perpendicular to, the neuromasts. Further analysis of information from the all neuromasts allowed for accurate location of the source [43]. Work by Chagnaud et al. helped further the understanding of the way that neuromasts respond to vortices and the responses that these signals generate in the brain [35]. They used artificial apparatus to generate vortex rings that were similar to those generated by the undulatory motion of a swimming fish, before placing a goldfish into this ring and measuring the responses of the afferents associated with those neuromasts stimulated by the vortex. It was shown that neural responses peaked as the vortex passed the neuromast, before reversing as the ring passed and the water direction reversed [35].

Chagnaud later went on to study the effect on goldfish (Carassius auratus) behaviour of placing it behind a cylinder in flow [36]. The cylinder was shown to generate a repeating pattern of vortices that alternately form and are shed from either side of the cylinder (where the front of the cylinder is facing upstream) via use of particle image velocimetry (PIV); this type of wake is known as a Kármán vortex street. It is similar to the wake that would be experienced behind a swimming fish, but the rotational direction of the vortices that are shed behind a fish are reversed [46, 103, 199]. The goldfish were placed into 3 types of environment: still water, laminar flow and a Kármán vortex street. Responses of the afferents associated with the neuromasts in the lateral line system were recorded. It was found that both the laminar and turbulent flow caused a similar increase in the activity among the nerve fibres under study when compared to the relative inactivity of the fibres in still water. Specifically, in the case of the Kármán vortex street, it was found that the amplitude of the spikes in nerve activity increased at the frequency at which vortex shedding occurred. Further, this relationship was especially noticeable if the fish was positioned at the edge of a vortex street. From the data in this study, it appears that this is the best position from which to gain the most data, particularly information regarding the vortex shedding frequency, or about the object or organism causing the vortex street [36].

2.1.3 The lateral line is necessary for accurate control

All of the above work demonstrates the ability of a fish's lateral line to detect water currents in their immediate surroundings, but it does not show the ways that this information is processed and used to the fish's benefit. Several studies by Schwalbe *et al.* worked with a variety of species of cichlids and studied their ability to detect prey using their neuromasts, in both light and dark conditions [163–166]. Initial work focused on peacock cichlids (*Aulonocara*) and asked the question whether *Aulonocara stuartgranti* was able to detect the changes in water pressure caused by the movement of prey items, in this case tethered brine shrimp. Cobalt chloride was used to deactivate the lateral line system temporarily [89] to create four different sets of conditions: in the light with and without a functioning lateral line, and in the dark with and without a functioning lateral line. The subjects were presented with six pairs of live and dead tethered brine shrimp and then their feeding behaviours were recorded. Results demonstrated 1) that *Aulonocara stuartgranti* is able to detect prey that are generating hydrodynamic stimuli in the dark, and 2) that once a cobalt chloride treatment has been applied, there is a reduced rate of stimuli detection and consequently feeding success, particularly in the dark. The study thus concludes that the lateral line must play a role in the detection and capture of prey [164].

Following this study, Schwalbe *et al.* performed a comparative study between the *Aulonocara stuartgranti* and *Tramitichromis sp.*, which differ substantially in the morphology of their lateral lines, with the *Aulonocara* possessing well developed 'widened' canal structures and pores and the *Tramitichromis* having underdeveloped 'narrow' canal structures and pores. It was theorised that these morphological differences would lead to measurable functional differences in foraging ability between the species. The *Tramitichromis* was subjected to the same behavioural trials as in the study above: assessment of ability to detect six pairs of live and dead brine shrimp in light and dark conditions, followed by exposure to cobalt chloride before further trials to reassess ability to detect brine shrimp in the same conditions. Results showed that the *Tramitichromis* was unable to detect prey in the dark before or after chemical ablation of the lateral line, and that its behaviour while hunting in the light was unaffected by the cobalt chloride. The study concluded that the *Tramitichromis* is a solely visual predator, and is, as a result, distinct from the *Aulonocara*, which uses its lateral line, or a combination of the lateral line and eyesight, to hunt, depending on the surrounding light conditions [163].

This work was taken even further, again by Schwalbe and Webb, to analyse in more depth the effect of varying light intensity on the hunting ability of the *Aulonocara stuartgranti* and the *Tramitichromis sp.* [166]. The prey detection ability of both species was tested over a range of light intensities deemed to be ecologically relevant, 0-800 lux, and it was found that both species were able to feed at light intensities exceeding 1 lux; Aulonocara was able to feed at light intensities all the way down to 0 lux. *Tramitichromis*'s inability to detect prey below 1 lux versus the *Aulonocara*'s ability to do so is indicative of the *Aulonocara*'s integration of non-visual hunting methods, most likely the lateral line given the context of the previous studies. The study goes on to speculate that the differences could be due to the wider ecological distribution of the *Aulonocara* and that being able to feed in darkness removes the need for competition over food with the *Tramitichromis* [166].

Having established the ability of the A. stuartgranti to detect hydrodynamic stimuli, a new study was carried out to test the importance of its lateral line in feeding behaviours. A. stuartgranti were used again, and they were trained to respond to artificial flows that originated from within a sandy substrate in which the Aulonocara might typically expect to find its prey; the importance of using the artificial water flows over still (dead) prey items is that it removes any visual or chemical stimuli that might have otherwise caused the fish to exhibit feeding behaviour. Test subjects were seen to respond to the five flow rates presented, as well as showing an unconditioned bite response upon detection of a 'pulsed' flow: the Aulonocara were seen to hover and bite when detecting a 'pulsed' flow, which is more similar to a prey stimuli, but were much less likely to bite when detecting a laminar flow. This shows the ability to detect a range of different types of stimuli. The test subjects were then treated with cobalt chloride and immediately after, they were seen to be almost completely non-responsive to the artificial flows. Within two days, some flow sensing ability returned and within a week, response levels were the same as recorded before treatment. This study shows a clear role of the lateral line in detecting benthic prey among members of the Aulonocara stuartgranti species, and more than that, that they have a quantifiable response to a range of different types of flow stimuli [165].

Other work on cichlids has shown that the lateral line is also used in mediating aggressive behaviours and assessing potential opponents during disputes over territory. Ablated fish are less likely to engage in conflict than their non-ablated counter parts when attempting to claim new territory [30]. Conflicts between ablated and non-ablated fish were almost always considered no-contest wins in favour of the non-ablated individual as well, implying that without the lateral line, assessments cannot be made about the potential opponent and the likelihood of victory, and as such, individuals back down in favour of avoiding injury [30]

With regards to collective behaviour and shoaling, it has long been established that the lateral line plays an important role. Pitcher *et al.* demonstrated the ability of blindfolded saithe (*Pollachius virens*) to accurately remain within a school indefinitely. It was only when the fish had their lateral line disabled (cut at the opercula) that the schooling behaviour stopped completely [142]. Further work with these fish, led by Partridge, was undertaken to better quantify the relative roles that the different senses play in shoaling; the same techniques were used [136]. It was discovered that blinding had relatively little effect on shoaling position, but that loss of the lateral line resulted in increased periods with neighbours at 90 degree bearing, or directly parallel to. Additionally, there was some changes in spacing, with blinded fish tending to swim further from their neighbours and those with a cut lateral line tending to swim closer. Startled schools where members have their opercula cut showed significant relationships between reaction time and the relative location of the object that startles; normal individuals in schools tend to

show similar reaction times regardless of the source of the startle. The previous study observed that blinded fish were only able to react to being startled when the neighbours were within a body length and only did so after the neighbour had accelerated away [142]. The final observation made is that blindfolded fish are more likely to match a neighbour's velocity than control fish, while cutting the operculum has no significant effect on whether a test fish will match a neighbour's speed, likely due to the aforementioned change in relative position allowing for a visuals-only assessment of the neighbour's velocity [136].

A study was also undertaken in which firehead tetras, *Hemmigrammus bleheri*, were monitored for metrics such as nearest neighbour distance, shoal radius, shoal order parameter and number of inter-individual collisions [55]. They were then subjected to a cobalt chloride treatment to temporarily deactivate their lateral lines, and were tested again for the same parameters. It was found that they lose the ability to successfully maintain a shoal, with increased shoal radius, decreased shoal order, and an increase in collisions between test subjects, where initially there had been none. The study concludes that the lateral line plays a significantly more important role than first thought when it comes to shoaling [55].

The above three works clearly show that the lateral line is playing a role in shoaling and more generally in collective behaviour. In theory, the mechanism by which the lateral line helps to mediate shoaling is understood. The beating tail motion that most fish use to swim generates a wake behind them, called a reverse Kármán vortex street, which is a series of alternately shed vortices that form off the trailing edge of the caudal fin during each tail beat [46, 103]. A vortex is defined as a region in flow where the fluid rotates around an axis line; the axis line is marked by a region of low pressure. These vortices rotate such that fluid in the middle of the wake moves downstream away from the fish and fluid on the outside of the wake moves upstream towards the fish; this is in contrast to a regular Kármán vortex street where fluid in the middle of the wake moves upstream [46, 103]. As already discussed, the superficial neuromasts on a fish are able to sense flow velocities while the canal neuromasts can detect flow accelerations [99]. The canal neuromasts are also able to detect pressure gradients as these cause flow accelerations; if a region of high pressure exists at one end of the lateral line and low pressure exists at the other, then fluid will flow through the system from the high pressure area to the low pressure area. In this manner, the lateral line system as a whole is able to detect and identify flow velocities and pressure gradients as the wake behind a neighbouring fish. Similarly, it can be used to detect the wakes that form behind other objects, as well as reading hydrodynamic flow fields and sensing pressure changes caused by approaching objects [35, 36, 103, 164]. However, in reality, given the complex and interconnected nature of all senses, there is still a level of uncertainty in the exact role that the lateral line plays in any behaviour. Additionally, it is unknown if the different regions of the lateral line play different roles in mediating behaviours, with the exception of some evidence linking the mandibular region to feeding behaviours [49, 164, 165].

It should be noted that some studies in the past have used disruptive procedures to create

the variance required to test their hypotheses. Particularly with the physical procedures, i.e. skin scraping [127] and blindfolding [136, 142], it is difficult to say with certainty that this has not had some effect on the behaviour of the affected individual. Recently, even work with cobalt chloride and aminoglycosides has been shown to be less definitive than previously thought. It has been shown that cobalt chloride treatment affects the olfactory systems, as well as exhibiting changes in behaviour [29, 78]. Low concentrations have been shown to have negative effects on a number of vital systems in a species of Mozambique tilapia (Oreochromis mossambicus) [135] and in the common carp (Cyprinus capio) [155], while higher concentrations have proven to be lethal in cavefish [78]. Studies involving zebrafish have shown that they too tend to have negative side effects from cobalt exposure [114], and even what is considered a safe dose for lateral line ablation has a 15% mortality rate [177]. Aminoglycoside antibiotics have been used to ablate just canal neuromasts in the past, but recently, it has been shown that superficial neuromasts and auditory hair cells, are affected too [28, 187]. A study on schooling giant danios Devario aequipinnatus also noticed that normal schooling behaviour was absent even after neuromasts had fully regenerated, indicating behaviour changes may be as a result of more than just the loss of lateral line sense [119]. More recent studies too have raised the issue of possible muscle damage caused by this class of drugs [66]. Ideally, a new experimental approach would be available to test lateral line characteristics without the potential implications on fish health and behaviour that the toxicity of the chemicals noted above brings with it.

2.2 A lateral line inspired sensor

The ultimate goal of this project was to take inspiration from nature, in this case groups of fish, to develop a simple lateral line inspired sensor that could be integrated into new or existing underwater robots in the future. The focus on a simple design is intended to enable easier mass production to allow the sensor to be used for swarming purposes. So far, other groups working in this field have for the most part chosen to focus on developing either single hair-cell sensors or on developing full lateral lines of off-the-shelf pressure sensors. This section presents an in-depth look at first the hair-cell work before moving onto off-the-shelf pressure sensor lateral lines.

The first work to explore the concept of a hair-cell inspired sensor was a paper by Fan *et al.* detailing hair-like sensors that were able to detect changes in flow speed. The sensor itself was made of a horizontal cantilevered beam with a metal strut fixed vertically at the free end and a strain gauge placed at the cantilevered end. The vertical metal strut is meant to replicate the hair-cell and it extends from the surface of the sensor up into the flow. As water flows past the metal strut, deflections are transferred through the stiff joint at the base of the hair-cell and into the cantilever joint where the strain gauge measures how much deflection is taking place [54]. The paper focuses on the design and fabrication of the sensor, which is made through a process called plastic deformation magnetic assembly (PDMA). Manufacturing begins with a

silicon wafer, on to which the strain gauge is attached, before an oxide layer is grown thermally in areas that will remain in the final sensor. Next, the metallic elements are attached to the top surface, namely the wires, as well as the structures used to create the strut: a thin layer of copper (300nm) followed by a thicker gold layer (600nm) followed by the Permalloy (10 μ m). The backside of the sensor is then etched to create the void over which the cantilevered beam is suspended, before the front is also etched to define the cantilever. The copper layer is then removed with weak HCl solution, and a magnet is used to plastically deform the Permalloy such that it is perpendicular to the cantilever. This is then the vertical hair-cell [54]. The paper does not detail any usage of the sensor to verify functionality.

Following this was work by Chen et al., who also developed an artificial hair-cell sensor, but with a strain gauge placed directly on to the vertical hair-cell [38]; this is in contrast to horizontally on a cantilever as seen above [54]. This device is fabricated from a stiff Permalloy beam fixed vertically and attached at the lower end to a strain gauge made from nichrome sandwiched between thick polyimide film; this film runs the length of the hair-cell. The fabrication process begins with a sacrificial aluminium layer on a substrate before the addition of the polyimide film. After this, the nichrome strain gauge is added, along with a gold chome alloy for the connections and the bending hinge. The permalloy is then electroplated on, and a second layer of polyimide is added as a protective coating. The aluminium layer is removed and a PDMA process is used to position the hair-cell vertically. Extra nickel is added to the bending point for reinforcement [38]. The sensor was deflected with a micromanipulator and it displayed a linear relationship between deflection and resistance. A number of sensors with varying hair-cell geometry were also tested: length $1000\mu m$, width $200\mu m$; length $1000\mu m$, width $150\mu m$; and length $1500\mu m$, width $100\mu m$. The authors found the longest hair-cell design to be the most sensitive. They note the sign of the change in resistance could be used to determine flow direction, but that responses are not symmetrical because the PDMA process does not reliably place the hair-cells at 90°.

This work was furthered by Engel *et al.* who designed an artificial hair-cell made entirely from polymers [52]. They promote the use of polyurethane over the more often used Polydimethylsiloxane (PDMS) for its improved tear resistance and ability to adhere to the base layer. The hair-cell is positioned on top of a ring of 4 evenly-spaced, carbon impregnated polyurethane sensors: these act as piezoresistive elements. Their positioning allows for 2-axis sensing, as the differential changes in resistance across the 4 sensors will give an indication as to the direction of the deflection. The hair-cell is designed to be 3000μ m tall and 500μ m wide. Fabrication of the sensor starts with the deposition of a gold layer onto the substrate to act as the conductor, before a photoresist mold is spun on for the piezoresistive sensors. The carbon-impregnated polyurethane sensors are then manually applied to the molds. The photoresist mold is then removed and a wax mold is added to define the hair-cell then the polyurethane is added. After allowing everything to fully cure, the wax mold is removed in a hot water bath [52]. Characterisation tests found the sensor to be approximately 20 times more sensitive than existing polymer artificial hair-cell sensors, and found that the sensor was able to detect as little as 0.1° of deflection [52].

Later work by Chen also developed a bio-inspired cantilevered flow sensor [39]. Fabrication also begins with a silicon wafer on to which a strain gauge is attached. The wafer is then oxidised to give it insulation, before contact windows are opened to allow connections to be made. Etching is then used to create the cavity behind the cantilever and to define the cantilever itself from the rest of the wafer. The hair-cell itself is made from an epoxy called SU-8 that is created in a monolithically integrated process [39]. This sensor was then characterised in a number of tests including determining the resonant frequency, the gauge-factor and the noise. The sensor was then exposed to a vibrating sphere while underwater to test its response to AC signals, and it was found that the sensor has an effective range of about 45-90Hz, and in this range the standard deviation across 10 trials was within 5% of nominal values. The sensor was also placed into steady flow to test the DC response, both in air and in water. At lower speeds response values matched well with those predicted by simulation, but at higher velocities these began to deviate significantly with the sensor reporting much lower velocities than expected. A final test was carried out to test how effective the sensor was at determining the direction of incoming flow in which the sensor was mounted to a rotating stage within a wind tunnel and a steady flow was directed at it. It was found that the sensor has an average angular resolution of 2.16° [39].

Peleshanko investigated how including a polyethylene glycol (PEG) hydrogel cap affects sensitivity to flow of a SU-8 photoresist hair-cell coupled with a piezoresistive strain gauge on a cantilevered beam [138]. The process to create the artificial hair-cell sensors is described as 'a conventional CMOS microfabrication technology', while the process to form the hydrogel cupula simply involved dripping the polymer solution on to the aforementioned sensors and then exposing them to UV light to cure them [138]. This design was tested in two ways, first with an oscillating sphere then with controlled laminar flow. Three sensors were tested, each initially as a 'naked' hair-cell, then covered with the hydrogel cupula. In the first experiment, the sphere was oscillated at a selection of frequencies between 10 and 110Hz; the threshold sensitivity was also tested, decreasing rms flow velocity from 10 to 0.01mm/s. The addition of the hydrogel cap saw signal intensity increase by 10-30 times, with an estimated amplification factor of 20-70. The threshold detection limit is reduced from 0.3mm/s (0.1mm/s at best) to 75μ m/s, marking a 2-4 factor improvement. In the second experiment, the 'naked' hair-cell displayed a range from 0.3mm/s up to 80mm/s while the capped hair-cell offered half a magnitude of improvement to dynamic range, 0.075mm/s up to 100mm/s, and 4 times the sensitivity of the original design [138].

Further work on adding a hydrogel cap to a hair-cell was done by McConney who studied real biological cupula to gain a more in-depth understanding of how to make a cupula that properly mimics a neuromast, specifically a superficial neuromast [116]. This focus was centred on providing a bending mechanism on a high aspect ratio hair-cell, as opposed to the low-aspect ratio, sliding mechanism that the previous work builds on [138]. PEG is used again for the hydrogel material, and a syringe is used to place the hydrogel solution at the desired position on the hair-cell, such that it does not wet the base. It is held in the correct place and allowed to dry, before another drop is added above. UV light is then used to fully cure the hydrogel. Hair-cells with caps were reported to be about 825μ m tall [116]. Sensors were tested in a tank of water with a dipole source, first without a hydrogel cap and then with. Bare sensors were not able to detect a dipole source vibrating 15mm away at 50Hz, but after the addition of the cupula, this distance increased massively to 45mm; flow velocity at these values is 85μ m/s. The cupula is reported to increase the sensitivity of the sensor by 38 times, and improve the minimum threshold velocity by 40 times, over frequencies ranging from 10 to 90Hz. It also marks a 30 times improvement over the dome like cupula in the previous work [116, 138].

Yang et al. and sought to demonstrate that the artificial lateral line that they had constructed could effectively locate an artificial dipole source and the motions of a real crayfish's flicking tail [207]. Their lateral line set-up consisted of a series of 15 of Chen's artificial hair-cell structures [39] located along the length of a tube, which represented the body of a fish. 9 of these artificial neuromasts were located along the length of the tube with a spacing of 30mm between them, with the remaining 7 perpendicular to the length with angular spacing of 30° between them. The two lines intersect in the middle of the tube, where they share a neuromast. To verify their artificial lateral line, they performed an experiment in which a minishaker is attached to a ball and vibrated to create an artificial dipole source of pressure waves. The artificial lateral line was able to sense the pressure field created by this dipole source and the results matched almost perfectly with those predicted by analytical models. Furthering this, they attempted to use the artificial lateral line to sense a real crayfish that was tethered to a wooden rod; this allowed the crayfish to be held at the correct distance from the artificial lateral line. For the experiment, the crayfish was placed near the artificial lateral line and held there until it no longer flapped its tail. The stimuli generated by the flapping tail were recorded as being quite different from those generated by the dipole, but the artificial lateral line was still successful in localising the source [207].

Another type of hair-cell sensor used ionic polymer-metal composites (IPMC) as part of an artificial lateral line [3]. IPMC materials consist of a ionic polymer plated with a conductor such as gold or platinum; voltage applied externally causes a redistribution of the ions within the polymer that causes a deflection in the material. Alternatively, a physical deformation causes an output voltage. An IPMC material using Li+ ions was selected; six sensors were constructed measuring $8\text{mm x } 2\text{mm x } 200\mu\text{m}$ and arranged in a line with 2cm between them, resulting in a 10cm long artificial lateral line [3]. Experiments using this design were tested in water with a dipole source vibrating at 40Hz with amplitude 1.91mm. By using a neural network, this artificial lateral line was able to locate the dipole source to within 0.3cm of its actual location when within 10cm of the lateral line [3].

Another type of sensor designed to serve a similar purpose can be seen in the development of

a flexible liquid crystal polymer pressure sensor [95]. These sensors differ from the previous ones as they are not hair-cell inspired, instead being referred to as diaphragm sensor: a flexible LCP membrane positioned in a free space between two contact pads on a PCB for the background. The LCP membrane is backed by a strain gauge that is able to detect any flexion that occurs across the membrane due to pressure changes. Several proof-of-concept experiments were carried out to verify the viability of the sensor in underwater pressure sensing tasks [95]. The first task tested a 2x5 array of the sensors detailed above and showed clear correlation between decreasing water pressure, expected with increasing flow speed over the diaphragm sensors, and decreasing voltage, a result of diaphragm deflection. Further tests were undertaken to determine the array's ability to detect objects as well. An object was towed past the array, resulting in clear spikes in pressure for each individual sensor at the point at which the towed object was closest to it. From the overall data generated by the array, it was also possible to determine the velocity of the towed object, as the distance between each sensor and the time between spikes were known; the results were shown to be accurate to within 2.5 percent [95].

Kottapalli et al. also designed, fabricated and characterised a micro electro mechanical system (MEMS) artificial whisker sensor that imitated the harbour seal whisker; this was chosen for its ability to suppress vortex induced vibrations (VIV) [93]. The design consisted of an artificial whisker printed using stereolithography and a piezoresistive sensing base. The whisker shape is unusual, with an oval cross-section and a unique undulatory geometry that makes it difficult to fabricate using more conventional methods, but stereolithography can overcome this and is used here to accurately recreate a whisker. The base consists of a lead zirconate titanate (PZT) sensing membrane, connected to gold electrodes and sitting on a cytop polymer layer. A silicon substrate is used as the base layer, and a cavity is etched in this, underneath where the whisker sits [93]. The whisker sensor was tested in water using a minishaker set-up with an 8mm diameter ball; vibration frequency was set to 35Hz and the velocity of the vibration was varied from a few μ m/s to 250mm/s. It was found that the output voltage from the sensor displayed a linear response to increasing velocity, and that the threshold velocity detection limit was 193μ m/s; this rivals that of the harbour seal itself. They did additional tests to measure how the orientation of the whisker affected the response to the dipole source. Results showed that when the whisker was oriented so that the long axis of the ellipse was at 90° to the dipole, the response was almost twice what was seen when the long axis was aligned [93].

Asadnia *et al.* also developed hair-cell sensors that used a PZT sensing membrane [10]. The design consisted of a PZT layer with a gold top electrode and platinum bottom electrode; this is bonded to a silicon layer on a silicon oxide layer on a substrate layer of silicon that has been etched with a cavity. A micro-stereolithographic process is used to fabricate a pillar onto the sensing membrane, such that the cavity sits directly beneath it. These sensors were then grouped together to form 1- and 2-D flexible sensor arrays by mounting them onto LCP substrates, patterned with metal interconnects, in a 1 x 10 array with 5cm spacing and a 4 x 5 array with 30 x 40mm total

footprint, respectively [10]. The first experiment sought to find the response of the sensor array to steady state flow. The velocity was varied between 0 and 80mm/s, in both water and air. In water, it was seen that at 20mm/s, there was a significant change in the slope of the response. This value corresponded to Re = 50, before which skin friction has the greatest effect on voltage output and after which pressure gradient does. Such is not the case in air, as Re < 50 at all times. Threshold sensing limits are recorded as 8.2μ m/s and 2.5mm/s in water and air respectively. The arrays demonstrate high sensitivity and have half the threshold sensing limit when compared to sensing systems in fish. The second experiment tested the ability of the array to localise a source. The 1D array was used to determine distance to the dipole source; extra data points were generated by shifting the array slightly, giving 20 points from which to begin to localise. Results show that distance could be estimated to within 1% of actual position for 25 and 35mm, but that this increased to 28% error for 55mm. Moving the dipole source parallel to the lateral line resulted in a shift in the position at which maximum sensor output was recorded. The final experiment saw the hair-cell sensors housed in a canal structure. Comparative tests between the now superficial hair-cell sensors and canal hair-cells sensors were undertaken to measure response to oscillating and steady state flows. Results showed that the superficial hair-cells respond independently of frequency while the canal hair-cells do not respond to steady state flows at all, and effectively filter anything less than 10Hz [10].

Kottapalli et al. went further to test both this PZT flow sensor [10] and the LCP diaphragm sensor mentioned earlier [95] for real time sensing of flow dynamics on a kayak, on a robotic fishtail and on a robotic stingray [96]. In the first experiment, two 2 x 5 sensory arrays were placed onto the hull of a kayak, one on each side; a large 5 x 6 x 1.5m water tank was used. First the kayak was moved vertically up and down on the surface of the water, which resulted in a near sinusoidal response from the sensor. Secondly, the kayak was yawed from side to side, with one end held fixed (the end without sensors). In this case, the response showed the two sensors were out of phase, as yawing the kayak left caused an increase in pressure on the left side sensor and a decrease on the right, and then vice versa as the kayak is yawed back right. The final test moved the whole kayak laterally back and forth at constant frequency and with amplitude 50cm. Output from a single sensor in this case again showed a sinusoidal response, but with an additional local peak located in the trough of the wave. This is indicative of the formation of a vortex being shed from the kayak [96]. Tests with the fish tail saw 3 sensors placed either side at 3, 6 and 9cm from the tip of the tail. The tail was then flapped between +/- 30° at 0.5Hz. All six sensors showed sinusoidal outputs of varying amplitude and phase, according to their position on the tail. Finally, these arrays were used on a robotic stingray to measure the velocity of the stingray and to track the flapping amplitude of the fins, as well as the frequency and phase. Increasing flapping frequency saw an increase in overall velocity, as measured by the on-board sensors [96].

A interesting design was conceived by Chon *et al.* who used a '4-legged octopus' shaped hair-cell connected to a PCB by a ball joint, such that the ball joint sat at the centre of the radial,

equidistantly-spread legs [40]. The hair-cell itself is teardrop-like in shape, with the narrow end connecting to the ball joint. The foot of each leg rests on a pressure sensor and so as flow deflects the hair-cell, force is transferred into the legs and then the sensor, which outputs an electrical signal in response. The 4-legged nature of the hair-cell also then allows determination of flow direction in 2D. The design was tested in a water flow tunnel and it was found that the sensor could detect flow rate above 106mm/s as well as being able to resolve angle of deflection to within 10° [40].

Asadnia *et al.* went on to develop a novel type of flow sensor that employed multiple flexible PDMS hair-cells in a bundle, designed to more closely mimic the bundles of cilia seen in nature [9]. These hair-cells were also of different lengths and arranged in a pyramidal shape, with one edge containing 10 of the shortest length hair-cells ($400\mu m$) and its opposite point containing a single instance of the tallest pillar (800 μ m); there is a consistent step-wise change of 45μ m between rows. Each pillar has a 50μ m diameter and rows are spaced 75μ m apart. These hair cells are situated on a PDMS substrate. The tip of each hair-cell is linked to surrounding hair-cells by electrospun polyvinylidene flouride (PVDF) nanofibres. The deflection of the different length hair-cells causes changes in the length of these fibres, which have strong piezoelectric properties, causing an output voltage; this is the primary sensing mechanism at work. The pyramidal layout of the hair-cells also gives the sensor as a whole directionality, as if flow is incident on the tallest pillar, fibres relax (inhibitory direction) and if flow is incident on the shorter pillars first, fibres are stretched (excitatory direction). Additionally, all of the hair-cells are covered with a hydrogel cupula, which protects them and increases sensitivity due to its greater height and width increasing surface area and raising the sensor out of the boundary layer [9]. To test this design, an 8mm diameter sphere was vibrated between 0 and 100Hz in a tank of water. The sensor was shown to be sensitive to frequencies as low as 2Hz, although the authors note that below 20Hz there is some distortion in the output. The sensor was also exposed to a range of dipole velocities between 1μ m/s and 80mm/s: it was able to detect signals above a threshold of 8μ m/s, with extremely high sensitivity. It is noted that the threshold value is half of that seen in some species of fish. To test how the sensor responds to flow from different directions, the dipole is moved between 0 and 180° , with 0° being aligned with the excitatory direction. As expected, the maximum sensor output occurred at 0° , with almost no response at 180° [9].

Kottapalli *et al.* also attempted to recreate the cupula of superficial neuromasts [97]. Development of this structure required 6 main steps: bonding a silicon layer to a layer of liquid crystal polymer (LCP) with a layer of epoxy (SU-8), patterning the LCP side with strain gauges and creating cavities in the silicon side, forming hair cells, positioning these hair cells correctly on the LCP, creating a nanofabril scaffold formation through electrospinning and finally drop-casting the hyaluronic acid methacrylic anhydride (HA-MA) hydrogel cupula. This resulted in a prolate sheroid-shaped cupula, that maximised surface-area exposed to flow while preventing contact with the sensing membrane. Addition of this cupula resulted in a 5 fold increase in sensitivity in air and 3 and a half fold increase in water. It also roughly halved the minimum flow resolution i.e. the smallest detectable change in flow velocity [97].

In a follow on paper by Bora *et al.*, work was done to create a hydrogel cupula mimicking those seen on canal neuromasts; these are hemispherical in shape instead of elliptical [25]. This artificial canal neuromast consisted of a lead zirconate titanate (PZT) piezoelectric membrane, a copper pillar and a hydrogel cupula. The piezoelectric membrane was attached to a top electrode, that was layered onto the bottom electrode, and beneath this were layers of cytop, silicon, and silicon dioxide, which sat above another layer of silicon in which a cavity had been etched. The hydrogel in this work was modified through the addition of methacrylic anhydride to give it the higher stiffness that canal neuromast cupula have in nature [25]. When tested against a 'naked' artificial neuromast (of the same design but without the hydrogel covering), the hydrogel covered neuromast exhibited over twice the sensitivity to the same stimulus. The authors also note that this design is able to detect and determine the velocity of a steady-state flow. Fluid interactions with the hydrogel dome generate a vortex wake with a set shedding frequency, which in turn causes vibrations that can be detected by the sensor membrane.

$$St = f^*L/U,$$

where St is the Strouhal number, f is shedding frequency, L is the characteristic length and U is the flow velocity

The Strouhal number is a dimensionless constant, used to describe oscillating flow mechanisms, that is typically taken as 0.2 for cylinders in flow, the shedding frequency is the frequency at which vortices are shed and will be the frequency detected by the neuromast and the characteristic length is the diameter of the cylinder. Flow velocity can then be calculated. The authors note this as the first piezoelectric artificial neuromast capable of such a feat [25].

Furthering this again, Bora *et al.* improves upon the superficial neuromast design above [97] through use of a high aspect-ratio, vertically aligned carbon nanotube (VACNT) bundle and an electrospun PVDF sensing membrane [24]. The VACNT bundle is 4000μ m tall and 350μ m in diameter, and is attached to the sensing membrane at one end and free to move at the other. The free end is covered with a hyaluronic acid (HA) hydrogel modified with tyramine that is the same height as the bundle and 4.3 times its width for three-quarters of its height. Tests in air and water show that the sensor has a velocity detection threshold of 5mm/s for both. In response to a dipole source, a VACNT bundle covered with a cupula shows a 2.5 and 8 times increased output in air and water, respectively, over one without. This is reported as an increase in sensitivity over the previous work with an HA-MA hydrogel cupula [24, 97]. Further tests were done using biological sources, such as the wake generated by a person walking past, a leaf falling past the sensor, and even falling micro droplets of water, and in each case, the sensor was able to detect and give the expected response [24].

Another novel type of neuromast design uses optical fibres bearing a sphere [201]. The sphere is situated in the flow and acts as the force recipient. 4 fibres are positioned in a square formation within a larger structure. They are inscribed with fibre Bragg gratings (FBG), a type of reflector that reflects different wavelengths depending on its physical properties. As a fibre deflects in response to flow, the spacing within the grating is varied. The changes in the grating result in shifts in the wavelengths within the fibre [201]. The design was tested in a tank of water with a minishaker positioned some distance away from the fibre structure; this was connected to optical interrogator channels to measure wavelength shifts. The set-up was tested between 2 and 100Hz and the response from the fibre structure showed a good match with the predicted models. Additionally, the fibres were not positioned in a perfect square within the fibre structure, creating slight differences in bending stiffness depending on the direction of the bending. This allows the sensor to determine the direction of flow, as long as information can be collected from at least 3 fibres. The resolution of this directionality is said to be within a few degrees of the actual flow direction [201].

Another team that used light in an artificial hair-cell sensor was led by Wiesmayr, who designed a PDMS waveguide with a low refractive index cladding to act as a hair-cell; as this is bent by flow there is then a measurable loss of light [198]. The PDMS waveguide has a Sylgard 184 core, with a RTV 615 cladding; a sealing layer of RTV 3145 was applied as well. Sylgard 184 has a 620nm absorption minimum so red light is used for the optical path. The slight difference in refractive indices between the core and cladding (1.4299 vs. 1.4286) results in high sensitivity to bending [198]. This design was tested first using weights to bend the waveguide, starting at 0.1g and going up to 5g: a linear relationship was observed with a 46.7% light loss at 5g. The design was then tested in air between 0.48 and 7.45m/s: a quadratic relationship is observed, with light loss varying between 0.05% and 5.04%. The authors go on to note that due to the complexity of fluid flow around a fibre, there may be some uncertainties that would require further study to fully unravel [198].

A novel design was created by Zhang *et al.* who used a radial field piezoelectric diaphragm to act as a self-powered sensing element that exhibited high sensitivity [210]. This is not a hair-cell sensor but instead more similar to the diaphragm sensor developed by Kottapalli mentioned earlier [95]. The radial field piezoelectric diaphragm consisted of two sets of two concentrically spiralling electrodes, one on top of the piezoelectric membrane and one underneath, attached to a piezoelectric membrane operating in the d_{33} mode. Being in d_{33} mode means that when force is applied perpendicular to the material plane, an electric field is generated within the material plane. In each set of electrodes, one is considered the 'high voltage electrode' and the other is the 'grounding electrode', and when the piezoelectric membrane is deformed, current flows from the former to the latter [210]. Finite element analysis is used to show that the design of the sensor is suitable for underwater disturbances as it is intended for. The sensor was tested in water with a dipole source at 35Hz with a range of oscillatory velocities and was found to be able to detect

oscillatory flow velocity as low as 4mm/s with high sensitivity. Additional tests for low frequency flows were done with the dipole source oscillating between 10 and 200Hz, and all values could be sensed. Finally, the dipole was fixed at 35Hz again, with fixed oscillatory velocity, and the distance to the sensor was varied. The sensor output decreased with increasing distance to the dipole [210].

Materials advances have resulted in teams exploring new materials to act as the sensing layer. An electrospun nanofiber mat made from polarized poly (vinylidene fluoride-trifluoroethylene) [P(VDF-TrFE)]/barium titanate (BTO) was coupled with a cavitated PI substrate and a poly(methyl methylacrylate) PMMA hair-cell by Hu *et al.* [71]. The P(VDF-TrFE)/BTO mat has a thickness of 40 μ m, and sits between a top and bottom Au/Cr electrode with 2 and 2.4mm diameter respectively. The PMMA pillar has 500 μ m diameter and 5mm height. The P(VDF-TrFE)/BTO is highly directional giving it the additional functionality of being able to sense flow direction [71]. The sensor was tested in water through the use of a dipole source of 15mm diameter, and it was found that the sensor had a velocity detection limit of 0.23mm/s. Directionality was tested with the dipole source fixed at a distance of 9.5mm/s and moved 360° around the sensor. Output was 3 times greater when the dipole source was in the plane of the material alignment than when perpendicular to it, showing the sensor to be capable of determining direction [71].

Kamat et al. developed a sensor that uses graphene as the sensing element, a design process consisting of 3D printing a metallic mold, possessing complex features such as a micropillar and a microchannel, into which PDMS could be cast to create a flexible artificial lateral line of the desired structure, and then drop casting piezoresistive graphene platelets into the microchannel to form a strain gauge [87]. This marks a simplification in the manufacturing process over previous designs, as the majority of the structure is simply cast from a single material (PDMS) with only the graphene strain gauge needing to be added. The sensor was tested while in contact with a dipole stimulus oscillating at 35Hz over a range of amplitudes from 26 to 241μ m, and in each case, the sensor showed a clear voltage peak at the associated amplitude. It was also found that the lowest detectable amplitude was 12μ m. Additional tests to assess the sensor's response to steady and dynamic flow saw an air stream manually swept past the sensor with air stream velocities of 2, 7 and 10m/s: increases in air speed saw increases in output voltage. The final test had the sensor positioned a distance from the dipole source in water, and responses to the dipole operating with fixed frequency, but varying velocity or varying frequency, but fixed velocity were recorded. The sensor demonstrated good sensitivity to the stimulus and was able to detect sphere velocity as low as 58mm/s [87].

This was furthered by Sengupta *et al.* who also used a carbon layer as their piezoresistive material [168]. They used electrospun carbon nanofibres, held in place between two optically clear adhesive films, as the sensing element to which a titanium pillar is attached at the free end. The titanium pillar in this design is 8mm long, extending it outside of the boundary layer and giving it exposure to higher velocity flow [168]. The design's response to a dipole source it

was in contact with was first characterised, followed by its response to steady state air flow, and finally, its ability to detect a dipole source in water was assessed. The minimum amplitude that was detectable in the first test was found to be 50μ m, but due to the wind tunnel used to assess steady state flow having a minimum velocity of 1.8mm/s, minimum detectable velocity could not be assessed. However, the sensor was reported to have high sensitivity over the ranges tested. When sensing the oscillatory motions of the dipole source in water, high sensitivity was again reported, with the minimum oscillation velocity detectable said to be 12.1mm/s [168].

A study by Tran and Park focused on making a hair-cell sensor that was both easier to manufacture and more robust than some of the earlier designs mentioned here [184]. They use 4 off-the-shelf piezoresistive pressure sensors, a printed circuit board (PCB), a hair-cell, and a PDMS cupula. The 4 pressure sensors are positioned at cardinal points of the PCB, and the 3D printed hair-cell has 4 perpendicular appendages at the base that sit on each of these sensors. The PDMS cupula is made in a 3D printed mold and attached to the top of the hair-cell. A layer of Ecoflex is poured over the PCB to waterproof it all and hold the hair-cell in place [184]. The sensor was tested first using a load cell, which gave an approximately linear relationship between force and output voltage. It was next tested in water at flow rates between 0 and 500mm/s, where the expected quadratic relationship was observed. Below 231mm/s however, the flow was observed to be approximately linear. Initially, readings were taken from one of the 4 pressure sensors at a time, but it was found that by taking a differential reading between opposite sensors, they were able to double the sensitivity. Further experiments were done to test directionality by placing the sensor on a rotating base and moving it through 360° while exposing it to airflow. Plotting the outputs of each of the 4 piezoresistive sensors resulted in 4 sinusoidal waves, each approximately 90° out of phase with each other, with each sensor exhibiting a peak when it was furthest from the incoming airflow. This indicates that the sensor can determine direction [184].

More recent work in this field furthers the development of the bio-mimetic artificial neuromast, placing multiple hair cells of differing length inside a hydrogel cupula structure[62]. This design uses a dynamic pillar that measures 1000μ m in height and 150μ m in diameter in combination with a number of stereo pillars, the shortest of which are 40μ m and the longest of which are 90μ m. The stereo pillars only occur on one side of the dynamic pillar, meaning that flow approaching from this side will move through these before reaching the dynamic pillar, resulting in reduced flow and a lag in response time [62]. To create the sensor, a silicon wafer was oxidised and then covered with a platinum layer as the bottom electrode, before being given a PZT film to act as the piezoresistive material. A second platinum layer made up the top electrode. The stereo pillars were made from SU-8 and were electrospun onto the top electrode while the dynamic pillar was fabricated from an optical fibre. A hydrogel cap was then dripped on to the design with a syringe [62]. The design was tested in constant air flow at 2, 4, 6, 8, 10, and 12mm/s and compared against the same design without a hydrogel cap. The hydrogel cap was reported to increase sensitivity by 107%. Additionally, directionality is tested, and it was found that the

response when flow approached the sensor from the stereo pillar side was significantly reduced, and also displayed a lag in response time. As such, they conclude that the sensor is capable of determining the direction [62].

On the other side is work on developing full artificial lateral line systems that use off-theshelf pressure sensors. Yang *et al.* adapted the concept of the lateral line for use with an already existing type of flow sensor called a hot wire anemometer (HWA) [206]. These sensors work by measuring the heat loss from the hot wire to the passing fluid, and inferring from this how much fluid is passing per unit time. The artificial lateral line they have developed consists of 16 HWA sensors: these are made through surface micromachining on the substrate before being rotated out of plane magnetically [206]. This artificial lateral line was tested on its ability to detect a dipole source in water and to characterise a wake behind a cylinder. The dipole was given 3 different paths to move along: parallel to the body, perpendicular to the body, and in a complex path in the plane of the body. In each of these cases, the artificial lateral line displayed measured locations that were very similar to the actual ones, with increasingly poor accuracy as the sensor moved further from the body. To characterise the wake behind a cylinder, the artificial lateral line was swept through a region of the downstream flow, and it was seen that the main features of the wake were captured: these being two large peaks in velocity fluctuations with a valley between in the region immediately behind the cylinder [206].

Another team was able to develop an artificial lateral line using off-the-shelf pressure sensors on a fish-shaped body that could detect and localise a dipole source [82]. A 3D printed fish shaped body was mounted with 2 arrays, each bearing 4 pressure sensors, that were positioned symmetrically along the vertical mid-line of the body. The design was tested in a tank of water containing a vibrating sphere. The sphere was placed at a total of 21 different points alongside the body of the fish, either in-line with one of the pressure sensors or between two of them, and then at either 10, 20 or 30mm from the body. After correction mapping was applied, overall localisation was reduced to 0.06 body lengths [82].

Further work with pressure sensors on a fish-like body was undertaken by Zheng *et al.*. It was found that this new system was not only able to detect and determine distance to a neighbouring robotic fish, but also the relative roll, pitch and yaw angles between them [211]. This fish-like body is designed to resemble the cube boxfish (*Ostracion cubicus*) and it uses a network of off-the-shelf pressure sensors to act as the lateral line: a single sensor is positioned at nose of the fish, with another pair located on each 'cheek' of the fish, and a further 3 pairs found evenly-spaced up high along the trunk of the fish. Additionally, it has a camera and an infrared sensor to help with obstacle avoidance [211]. 7 experiments were run to test the sensing ability of the lateral line in a flume tank at 17.5cm/s. Firstly, determining the vertical distance between the robotic fish and an adjacent caudal fin; secondly, determining the oscillation amplitude of the upstream caudal fin; third, determining the oscillation frequency of the fin; fourth, determining the offset between the robot body,

sixth, determining the relative pitch between the body and the fin; and finally, determining the relative roll angle between the fin and the body. For each experiment, the body of the robotic fish was fixed to a pole and held in place behind a beating caudal fin; pressure values were recorded as the element being tested was varied over a given range and plots were made to characterise the responses. From these responses, the authors conclude that their lateral line is able to accurately sense the vortex wake caused by the upstream caudal fin, and determine the relative states of both the fin and the robot [211].

A novel system using differential pressure sensors, instead of absolute or gauge, was trialled by Xu and Mohensi [205]. Two designs were conceived to test the effectiveness of the system in both estimating forces acting on the vehicle while it is in motion, and detecting a nearby wall at different approach angles. In the first test, a PVC testing cylinder, oriented horizontally and measuring 16.8cm in diameter and 81.3cm in length, was given 20 differential pressure sensors distributed across one half of the cylinder's length. The sensors were arranged in pairs, such that half detected pressure differentials along the length of the cylinder and half along the circumference. This set-up is attached by a vertical rod to a sliding cart that drags the cylinder through the water at which point pressure readings are taken. In the tests, the cart is accelerated to 0.1m/s before being decelerated to a stop. Over 4 trials, the standard deviation in estimation error (the error between the measured force and the actual force) was about 0.8N. The second test used a 76cm long vertical PVC cylinder, again with 20 differential pressure sensors, this time in a line around the circumference of the cylinder; the sensors only cover the forward facing 180° of the cylinder. The cylinder is accelerated towards a wall of 1.2x1.2m that is angled at either 90, 60 or 30° relative to the motion before being decelerated and stopped. Results saw a greater pressure acting on the cylinder when the wall was present, and saw that with decreasing angle, the pressure distribution moved from symmetric at 90° to being more and more asymmetric. Attempts to estimate distance to the wall found that across 5 trials the standard deviation was 0.83r (where r is the distance to the wall). A non-linear relationship was found when trying to determine wall angle, where uncertainty increased as the angle tended away from 90°. The authors conclude that results from the experiments above agree with data collected from simulations, and that such a system would aid in underwater exploration [205].

Ahrari *et al.* focused on optimising the design of the lateral line system by considering alternative ways to arrange the neuromasts to better locate a dipole source in 3D [6]. The work considers the use of a lateral line system that incorporates neuromasts that are offset from the lateral line plane of symmetry or use an out-of-plane angle, or one that uses multiple lateral lines in parallel. Maximum offset is set to be either 0, 0.5, 1 or 1.5cm from the lateral line's plane, and maximum rotation can be $0, 30^{\circ}, 60^{\circ}, \text{ or } 90^{\circ}$. The different cases (offset and rotational) are tested for both a single lateral line and for multiple in parallel. Two cases are also considered where the dipole is in plane with the lateral line and vibrating towards it, and another where it is out of plane. Fitness functions are used to determine which of 32 test cases is best. They found that

when the dipole source was in plane, a single lateral line with angled neuromasts gave the best results, while if the dipole is out of plane, multiple lateral lines all using angled neuromasts is the most effective [6].

Liu *et al.* used the FLUENT software to simulate the response of a proposed artificial lateral line to a dipole source positioned in a number of locations in the surrounding fluid, before going on to build and test the design [105]. A dipole source was simulated directly in front of the lateral line system over a range of distances, at a 45° angle to the system, in a number of positions parallel to the system, and at a range of distances perpendicular to the system. Using an equation for vibration source location, they found that angle could be calculated to within 3% of actual location. Moving the dipole parallel to the artificial lateral line showed a shift in where the peak was detected, while changing the distance to the source both at the front and to the side of the system gave an inversely proportional response [105]. The system was then built in real life, using pressure sensors as the sensory units, and tested. Comparisons were made with the experimental data, but poor similarity was observed; this is attributed to the assumption that flow is incompressible and non-rotational used in the vibration source location. A neural network is then employed to gain better accuracy, and the system is tested again, with results now showing 96% accuracy in identifying dipole source frequency, 98% accuracy in identifying amplitude and over 93% accuracy in determine dipole location.

Xu *et al.* also attempted to optimise a lateral line consisting of a series of pressure sensors around the outside of a robotic fish-like body [204]. They focused on determining the best positions for the sensors using an Optimal Weight Analysis (OWA) algorithm. The fish body was divided up into a series of potential sensor locations and then simulations were run of the body in flow behind a cylinder with 4 different parameters: flow speed 5, 10, or 20cm/s; deflection angle 0° , 15° , or 30° ; distance offset from cylinder centre line 0, 5 or 10cm; and steady or unsteady flow (varied by addition of a 10cm diameter cylinder upstream). The OWA algorithm relies on combined time and frequency domain inputs into an Analysis Of Variance (ANOVA) algorithm to help distinguish conditions more efficiently. After the sensor positions have been optimised, the relative performances of the new layouts were tested for the ability to determine speed in steady flow and in turbulent flow, and to determine the angle of orientation in steady flow and in turbulent flow. It was found that using the sensor placement[204].

Tang *et al.* also developed a lateral line of off-the-shelf pressure sensors embedded on a 3D printed body inspired by a trout [182]. This design consisted of 8 pressure sensors embedded into holes along the mid-line of the side of the body. The body was then placed in water and a 50mm diameter dipole, oscillating at 2Hz and with amplitude 50mm, was moved around it. Responses from the sensors were recorded separately and it was found that they were consistent with predicted results. They conclude that using this design they are easily able to identify the direction of the dipole [182].

Some teams were able to combine the two branches and develop a full lateral line with haircell inspired sensory units. Klein et al. used a series of optical flow sensors in an artificial lateral line canal to detect an object in air, a vibrating sphere in water, an upstream cylinder in water and to localise said cylinder [91]. The artificial neuromasts in this study were made using transparent silicone bars that were of equivalent density to water, so that any deflection was only as a result of fluid motion. One end of this silicone bar was illuminated using an IR diode; light from this was passed through the bar and illuminated an optical fibre, connected to a phototransistor. Water motion within the canals, as a result of external pressure gradients, caused the silicone bar to deflect which resulted in changes in the amount of light received by the transistor, and in turn a change in voltage. The artificial neuromasts were also given directionality by having the bar not aligned at 0° when at rest, such that different directions cause either a rise in voltage (moving towards 0° first) or a fall (moving away from 0°) [91]. Several experimental set-ups were created to test whether the artificial lateral line canals could detect motion in air, vibrations in water, the wake of an upstream cylinder, and finally to see if an upstream cylinder could be localised. The first used a section of milled PVC with 3 pores and 2 neuromasts to detect the motion of a finger passing by in air. Using just these two neuromasts, velocity could be determined using differences in the time of detection made by each neuromast. A single neuromast between two pores was used to sense the sinusoidal patterns of a vibrating sphere in water, while two sections of canal, hosting 3 neuromasts each between 4 pores, were able to detect, determine size and localise an upstream cylinder. The final set-up used 8 neuromasts and 9 canal pores to accurately determine background flow velocity [91].

A group led by Jiang was able to develop a flexible artificial lateral line that closely imitated the form of a real lateral line and was shown to detect a high frequency dipole source [84]. The lateral line consisted of 4 PVDF/polypropylene laminated cantilevers, each bearing a biomimetic cupula on the free end. PVDF has a high peizoelectric voltage coefficient so acts as the electromechanical transduction material. PDMA is used for the structure of the canal, due to having similar mechanical properties to the natural lateral line. As with the previous examples, external pressure affects the internal fluid through the canal pores. This causes fluid motion within the canal which results in deflections of the cantilevers and generates piezoelectric charges. Canals were made through a molding process, before silver electrodes were selectively deposited and the PVDF layer was laminated to the polypropylene layer before being cut into the required cantilever structures. The PDMS cupula was then attached to the distal end [84]. The design was characterised using a dipole source in water, and it was found that it was more sensitive that other similar designs, but unable to detect static objects due to the use of piezoelectric transduction [84].

The most recent attempts to optimise the design of the canal have seen the introduction of a slight constriction in the canal diameter as a way to increase internal pressure and therefore sensing performance [107]. The canal neuromasts are fabricated using a poly(vinylidene fluoride-

trifluoroethylene) (P(VDF-TrFE)) piezoelectric copolymer cantilever on a layer of polyimide, with a biomimetic hair-cell attached to the free end. The canal itself was made from PDMS, chosen again for its being mechanically similar to a natural lateral line. The canal is a 1 x 1mm channel that is reduced at the position of the cilium from 1mm width to 700μ m. Simulated results suggested that such a constriction would increase signal strength from the artificial neuromast by 59% over a square canal without a restriction; the two canals, constrictred and not, were inspired by eyeless cavefish (*Sinocyclocheilus tianlinsis*) and goldfish (*Carassius auratus*) [107]. The design was characterised through use of a dipole source in a custom-designed closed circuit water tunnel. A 15mm diameter sphere was vibrated at 80Hz with an amplitude of 0.55mm, over a range of vertical distances from the lateral line. It was found that the straight canal sensor was roughly 6 times less sensitive, with a threshold pressure gradient limitation of 4.3Pa/m versus the constricted canal which was 0.64Pa/m. It is also reported that the sensitivity of the constricted design is comparable to the natural system seen in the mottled sculpin (*Cottus bairdi*)[107].

A final lateral line inspired system of note to mention is one developed by Wolf *et al.* who created a large-scale 3.5m long artificial lateral line system of 8 all-optical 2D flow sensors; a neural network is used to interpret flow signals [202]. The flow sensors are detailed in a previously mentioned work [201]. Sensors were situated 1.4m underwater and spaced 0.5m apart and a number of different size and shape objects were towed past. The objects in question were a barrel, a dumbbell, a ball, a capsule and a capsule with a vortex shedding attachment on the back. Some objects were towed past at two distances, and it was seen that when the object was closer, the sensor had a greater response. Each of the objects was seen to have a different hydrodynamic profile, with the ball having a response closest to that predicted by theory. The neural network is identified as being able to classify which object is creating the detected wake, if not perfectly yet. The author highlights the usefulness of being able to sense in 2D, as the neural network actually uses signals from in the y-direction (perpendicular to the length of the lateral line) more than the x-direction to differentiate objects. This study marks the first instance of an artificial lateral line that is larger than anything seen in nature [202].

All of the systems detailed above represent some of the most advanced work in a number of fields, combining manufacturing advances in Micro Electro-Mechanical Sensors (MEMS) with improvements in understanding of fish morphology and fluid dynamics. They show great improvement over what was in the field even just a few years ago. However, with each advance they grow ever more complex and difficult to manufacture, and with these increases in complexity, they become more expensive. Only a single example of a system that prioritises simplicity exists here, and so further work is needed to develop simpler systems, that are cheap and easy to manufacture, if the artificial lateral line is to become more commonplace.

Typically, as well, due to the scales involved in the biological systems, artificial lateral line systems are designed to be on the micro scale. Flow characteristics vary massively as scales change, so for bio-mimetic systems staying small is a necessity, but work towards a bio-inspired system that is still functional at larger scales would significantly increase the ease of manufacture of artificial lateral lines, and potentially increase their functionality too. Work towards this has begun with Wolf *et al.* who demonstrate the feasibility of a large scale system, but their system uses only superficial neuromasts, and so further work is needed on the canal neuromast side [202].

2.3 Underwater platforms

Developing a suite of advanced sensors for detecting pressure fields in the underwater environment is important work for furthering autonomous underwater vehicle technologies, but without suitable robotic platforms on which to mount these sensors, they cannot be properly employed in real world situations. Ideally, the robotic platforms on to which these bio-inspired sensors will be mounted will be bio-inspired themselves. A good example of one is the walking lobster-inspired robot, detailed in a paper by Ayers et al. [11]. This robot also makes use of hair-cell sensors but goes even further in its attempt to mimic biology, using shape memory materials (Nitinol) to more closely mimic the way that crustacean muscle material works, as well as studying the lobster's locomotory patterns closely using video recording and correlating the movement and angles of the lobster's limbs so that the robot's own limbs move in the same way. It is quoted as being superior in shallow and complex inshore environments which are typically more unstable, with irregular currents and a larger number of obstacles. Lobsters are very effective at navigating through environments such as this, with uneven floors and with a multitude of rocks, crevices and plant life. Their body, claws and swimmerets are also effective hydrodynamic surfaces that allow for greater control. These characteristics make them an effective basis for a robot that must navigate the sea bed to find mines [11].

More recent work is the implementation of both types of sensor mentioned above, the hair-cell and the diaphragm, on to a biologically inspired stingray robot [8]. Hair-cell sensors are used to measure the forward velocity of the stingray, while diaphragm sensors are used to measure the various pressures around the fins of the stingray. This information is needed to effectively control the flapping motions of the fins which are the main propulsion method of this robot. The stingray itself is made of silicone polymers and has servo motors embedded in the fins, allowing them to oscillate at a range of frequencies from 0.5Hz to 3Hz. It is shown in the study that the robotic stingray is completely functional and has full control over a range of speeds, as well as being able to turn accurately while remaining on a prescribed trajectory line [8]. It should be noted that this stingray was positively buoyant and only operated at the surface, eliminating the need for 3D control schemes.

Robots that take inspiration from the undulatory swimming mechanism seen in many fish and eels have the added benefit of generating a wake that is similar to that of a swimming fish [36, 46, 91, 95, 103, 199, 204]. This means they can be more easily detected with an artificial lateral line, which can improve coordination in groups. Ayers *et al.* also detail an undulatory robot based on the motions of an eel [11]. This robot is again highly bio-mimetic, with nitinol wires acting as the muscle fibres, and is also proposed as an anti-mine countermeasure, as many of the behaviours that eels and lampreys display when hunting for prey are the same behaviours required by a robot searching for mines. Several other robotic platforms that use an undulatory swimming motion exist, such as a robotic snake, which was tested both experimentally and in simulation, and also used a swimming motion inspired by those seen in swimming eels. Both sets of results showed that a Line-of-Sight guidance controller was able to steer the robot to and along its desired path [90].

Systems also exist that mimic the tail fin beating patterns seen in fish to achieve the required undulatory swimming. This has been achieved in a number of ways, with one study using super coiled polymers to imitate the fish's muscle tissue. The fish robot here used these polymers in an antagonistic set-up. This design was shown to generate a tail beat pattern, with an added bonus that their being used underwater helps dissipate heat build up within the polymers, an issue seen when they are used in air. However, this robot was lacking a control algorithm at this stage [1].

In a similar study, albeit further progressed, a robotic fish used dielectric elastic actuators coupled with a soft body. Here the elastic actuators are the artificial equivalent of the fish's muscle, using an electric current to illicit a change in shape, which in turn cause the swimming motions in the robot. Their use gave swimming speeds very similar to what would be seen in nature [170].

Another robotic fish meant to imitate the body of a trout uses a waterproof servo motor as well as a number of rigid body segments and elastic cables, meant to imitate the bone and muscle one would expect to see in a real fish. This design had the added benefit of having a variable body stiffness, thought to be an important factor in swimming ability. Using body stiffness values similar to those seen in its inspiration, the trout, they found robot and fish to have very similar swimming speeds [171].

Taking soft robotics to the extreme, a robot inspired by the deep-sea snailfish (*Pseudoliparis swirei*) recently used a flapping tail mechanism, in combination with an entirely compliant body, to successfully dive to 10,900 metres, and to swim freely at a depth of 3,224 metres [101].

2.4 Swarms

Swarms offer a level of robustness not seen in typical engineering for multiple reasons: the agents themselves are typically simple and the same, in both form and function [27], and there are a lot of them, so as such the loss of one is unlikely to have a serious negative effect on the swarm as a whole. Consider a system of 100 robots monitoring 10cm^2 each, 100cm^2 total, that loses an agent and is now only able to monitor 99cm^2 , versus a system of two robots that monitor 50cm^2 each and

have their capacity reduced by half if one of them fails. Additionally, as the agents all share the same function, it is easy for them to simply shift positions so that the 1cm² of missing coverage is spread out among the swarm and it becomes easy to infer what is happening in the now very small individual gaps. Another advantage lies in that there is no central processing point, and as such no single failure mode, so no single robot can take down the whole system [27]. Significant challenges are associated with taking this approach however, as having multiple agents adds another layer of difficulty to the control algorithms, where they must be able to interact with each other and their environment, and, from these interactions, generate the desired behaviour [156]. An environment that is known to be particularly difficult to operate in due to low light levels, turbulent waters, and issues in both communications and navigation [133], can potentially benefit from many of the advantages mentioned above. What follows is a brief look at some of the already existing underwater swarms.

2.4.1 Underwater swarms

Recently, a lot of work in the field of underwater robotic swarms has been done, ranging from the development of robotic swarming platforms to the development of control mechanisms, both biologically inspired and not. Some of the earliest mentions of swarms of underwater robots were made by NASA, who proposed a combined effort of both airborne and underwater robots, named 'aerobots' and 'hydrobots', as a means of extra-terrestrial exploration [14]. This concept was further explored when Honary *et al.* were able to use the already developed 'aerobot' platform to simulate potential underwater operations and then also test these operations in reality [70]. These real-world experiments were done in air however.

Another early proposal was a swarm of underwater robots whose purpose is drift on the currents to explore the oceans. Their robots would enable the observation of sea life without disturbance and give information about the natural motion of the oceans [75, 121]. This idea was actually recently taken to completion, successfully deploying 16 vehicles to monitor ocean dynamics. These robots are able to change depth and continuously record their 3D trajectories, as they drift with the currents. The field test of these robots provided interesting information about the dynamics behind the formation of plankton patches [76].

The 'Serafina' robots are a swarm of underwater vehicles that was designed to study large formations, up to hundreds strong. These robots are simplistic but able to form complex shapes that can be defined by the region being explored, or as a shape that can model migration, using only local information to govern their behaviour [86]. They feature again in a project centred around developing a localisation system that relies on acoustics, a system that was tested both in an experimental tank and in an open water lake, showing the usefulness of the system [98].

Another project involving a swarm of underwater robots that is using the concept of exploration of large spaces for a slightly more niche purpose is the THESAURUS project, using the 'Tifone' robot, which seeks to explore new archaeological sites. The design is for a modular system that can be tailored specifically for the mission at hand, and uses autonomous systems for exploration and image analysis [7].

One of the largest underwater swarms is the CoCoRo project [134, 161]. This promised a novel system of robots for search and environmental monitoring purposes. It is comprised of two types of robotic unit, a basestation and the underwater vehicles themselves. CoCoRo takes inspiration from multiple biological sources, including fish and the immune system. Swarm members are designed to be simple, with low-level local processing, and with the whole swarm's purpose being to help study emergent behaviours in simple agents. CoCoRo's design was not the only thing to be bio-inspired, as it will be powered by a novel bio-inspired operating system too [161]. An update to this project proposal was released detailing the plans for one of the robotic units, named 'Jeff'. 'Jeff' is the underwater vehicle element of the CoCoRo project, intended to connect with the basestation element for recharging. 'Jeff''s design is centred around being highly manoeuvrable in the cluttered underwater environment, with energy-efficient propulsion and buoyancy control, as well as bearing a suite of sensors for multi-directional perception and communication [134].

Another study, led by Mintchev, developed the 'MONSUN II', a small and low-cost underwater vehicle designed specifically for use in swarms [120]. Being low-cost allows high numbers to be employed, giving the swarm fault-tolerance through redundancy and parallelisation of tasks. These robots were conceived for environmental monitoring purposes, and their suitability for the task was demonstrated first through simple tests to demonstrate control and then through the completion of a simple following task [120].

The 'HippoCampus' robot is another small and low-cost underwater vehicle for swarm applications, although following a different design, more similar to a quad-copter in form [65]. This quad-rotor design gives the underwater vehicle increased mobility, allowing it to manoeuvre well in a close quarters test tank in experiments. They were able to demonstrate the 'HippoCampus's' autonomous path-finding capabilities in experiment [65].

'Vertex' offers an agile, five degree of freedom platform, with acoustic localisation and communications systems on board [160]. This underwater vehicle also possesses the processing power to run behavioural simulations on board to allow for faster operations underwater and remove the need for communications with the surface [160].

Most recently, a new swarm of underwater robots called the 'BlueSwarm' has been developed [18]. The members of the swarm, known as 'BlueBots' are fish-like in appearance and use a caudal fin for forward motion, two pectoral fins for turning and a dorsal fin for depth control. The 'BlueBots' use 3D visual perception to locate and track the two blue LEDs that each 'BlueBot' bears, and this allows them to effectively coordinate and shoal in a similar fashion to real fish [18].

As it currently stands, none of these swarms have an artificial lateral line as part of their sensing systems. While many of the artificial lateral lines discussed earlier would likely be suitable on a number of these systems, there still exists a number of difficulties with mass

CHAPTER 2. STATE OF THE ART

producing the micro scale artificial lateral line systems. More work needs to be done to create an artificial lateral line that can be easily produced on the scales required for a swarm that covers the oceans.



THE CREATION AND CHARACTERISATION OF A NEW DATA SET

FIGURE ere we examine the possible relationships between behaviour and morphology in our hybrids group, create our experimental environments and establish the procedures to generate all the data required, before then moving on to characterise this data and certify its suitability for use in this study.

3.1 Introduction

This study uses a group of second generation hybrids from the cichlid family (*Cichlidae*). This family was chosen due to its relatively recent diversification that has resulted in a large number of species that are similar with the exception of a pronounced diversifying trait [158, 173]. Second generation hybrids were chosen as they are expected to show a wide range of characteristics spanning between the parent species as extremes [186].

3.1.1 Cichlids

Cichlids are a family of teleost fishes who span a vast area, from South America all the way to India, but within this range, the greatest species diversity occurs within South America and Africa, where over 1,600 species can be found [131]. Lengths can range between a few centimeters up to a meter, and while they are typically shallow water dwellers, species have been recorded as deep as 300m. Diet is also varied, with the family containing herbivores, carnivores, planktivores, omnivores, and detritivores; essentially the full range of feeding behaviours possible. This extreme diversity in feeding behaviour has allowed cichlids to occupy such a wide range and inhabit so many ecological niches [92, 131].

Even more interesting is the rate at which this diversification occurred. This has resulted in an excellent opportunity to help further the understanding of adaptive radiation [49, 72], and they are an important case study for the development of new species in evolutionary processes. Additionally, despite the diversity seen in the radiation, the resulting species have remained closely related, especially within the Lake Malawi radiation [49, 92, 158, 173]. It is this relatedness that we take advantage of.

3.1.2 Hybrids

Inter-specific variation and hybridisation are useful in evolutionary biology to study inherited traits [64, 145]. An individual's genome dictates how inherited traits will express themselves, and so slight variations in the genome will result in variations between individuals within the population. Being able to spot these variations and then associate them to the differences in morphology and/or behaviour can then lead to a greater understanding of how a species has evolved. Hybridisation takes this a step further, as it is possible to essentially isolate a specific trait and then generate variation for it; this can be done by choosing two closely related parent species who exhibit significant differences in only one aspect of their behaviour or morphology and hybridising them to create offspring who will first show intermediary characteristics and then in subsequent generations will show a wide range of characteristics spanning between the two parents [186]. This technique is especially powerful because it allows the manipulation of traits without the need to physically alter individuals which can have unwanted and potentially negative side-effects [32, 100].

3.1.3 The lateral line

The lateral line is a body wide sensory organ found in most of the 26,000 extant teleost fishes [42]. It is comprised of sensory units called neuromasts, that can be either surface based, called superficial, or sub-dermal in hollow structures, where both neuromast and structure are called canals [17, 42, 45, 69, 99, 162]. The lateral line is known to be essential in mediating a number of different aspects of a fish's every day life, from feeding [33, 80, 81, 106, 126, 128, 152, 163–166] to predator avoidance [56, 117] to shoaling [55, 136, 142], however, in each case it is still unknown specifically how an individual uses its lateral line when displaying those behaviours. It is also largely unclear if the different parts of the lateral line play different roles in different behaviours. It has been demonstrated, however, that fish are able to use their lateral lines to sense the wakes shed by the swimming motions of neighbouring fish or behind upstream obstacles [35, 36, 46, 103, 124, 199]; this may contribute to mediating shoaling behaviours and is what we will investigate. By hybridising two closely related cichlid species, *Aulonocara stuartgranti* and *Otopharynx lithobates*, with pronounced differences in their lateral line morphology, offspring that show a range of lateral line characteristics are created, ranging from the well developed

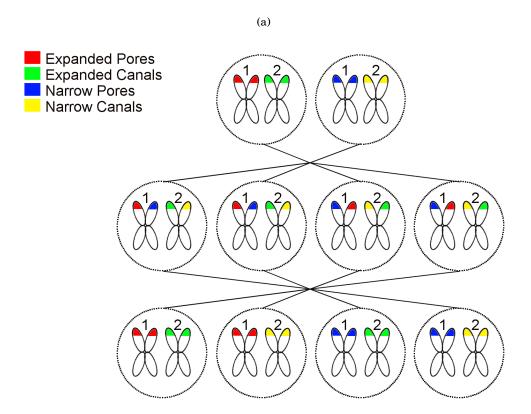


Figure 3.1: The process by which hybridisation results in a range of characteristics. Individual 1 has genes that express as expanded pores and expanded canals, while individual 2 has genes that express as narrow pores and narrow canals. Individuals in generation 1 (the middle row) will receive half of the genes for pore (1) and canal (2) size from one parent and half from the other, resulting in all of them possessing genes for both expanded and narrow pores and expanded and narrow canals. This will typically result in pores and canals that are intermediate between the extremes. The subsequent generation however will then have every combination of the available genes, resulting in some individuals with expanded pores and expanded canals, some with narrow pores and narrow canals. A further 12 combinations exist than what are shown in the bottom row, which include combinations such as intermediate pore size and expanded canals, or narrow pore size and intermediate canal size. In this way, a wide range of lateral line morphologies will be seen in the second generation hybrids. In reality, the morphology of the lateral line is affected by more than just two gene pairs, and so significantly more combinations will exist and therefore much more variation will be seen.

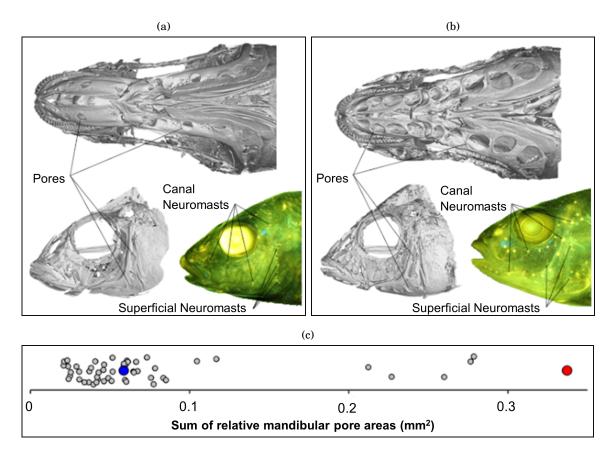


Figure 3.2: Differences in lateral line morphology of the parent species. (a) The morphology of the *Otopharynx lithobates*, showing reduced pore size and reduced visibility of canal neuromasts. (b) The morphology of the *Aulonocara stuartgranti*, showing larger pore size and increased visibility of canal neuromasts. (c) Comparisons of the relative mandibular pore areas of 53 species of cichlids, with the relative location of the *Otopharynx* highlighted in blue and the relative location of the *Aulonocara* shown in red. Jitter is added in the y axis to prevent excessive overlap of points. Data for this graph is taken from Edgely *et al.* [49].

'widened' lateral line morphology seen in the *Aulonocara* to the much less developed 'narrow' lateral line seen in the *Otopharynx*.

3.1.4 Experimental set-up

Groups of fish containing one target individual (hybrid or parent) and four companion fish were subjected to flow to observe their collective behaviour. DASPEI (2-(4-(dimethylamino)styryl)-N-Ethylpyridinium Iodide) dye and CT scanning were then used to analyse lateral line morphology, before statistically validating the variation of morphologies and behaviours. Collective behaviour was analysed through experiments in a custom built tank that was constructed from a PVC plastic tub connected to a re-circulatory system of pipes containing an outboard motor propeller that was used to drive the flow. Flow was laminarised (see Fig. (3.3(a) for a depiction of laminar flow) via the use of a flow straightening mesh and circular tubes could be inserted just downstream of this to generate turbulence (see Fig. 3.3(b) for a depiction of turbulent flow). Behavioural trials took place in flow for two main reasons. Firstly, the flow induced rheotactic behaviours in the fish with the result that individuals faced upstream for the majority of the trial (Fig. 3.4(b)). As such, the majority of the time the wake caused by the fish's swimming motions formed behind the fish and moved directly downstream; any trailing fish would then be exposed to this (Fig. 3.4(b)). This is advantageous over a no-flow situation, where individuals might be swimming at angles to one another, and so trailing fish might not be exposed to the wake fully, if at all (Fig. 3.4(a)). Secondly, the constant flow means that individuals will spend most of the trial period swimming, and in turn generating the wakes that we are interested in. In a no-flow situation, it is possible that individuals would spend large periods of the trial stationary, and in turn give no data. All individuals were tested in both laminar and turbulent flow regimes. The tank was set up to give both laminar and turbulent flow because it was hypothesised that when in laminar flow, the detection of an upstream neighbour's wake would be a much simpler task than in the turbulent flow regime when the vortices being shed by the turbulence generators would cause significant interference (Fig. 3.4(c)). We expected that the Otopharynx would be more affected by the turbulence than the Aulonocara, and that the Otopharynx (and the hybrids with more Otopharynx like traits) would increase the distance to their neighbours to avoid potential collisions in the more confusing environment. All trials were recorded and analysed to determine key parameters. DASPEI dye was used to mark the neuromasts of all test individuals then these were photographed and position and number were recorded to generate lateral line morphology parameters. Parameters of each individual were plotted against all other individuals to determine if there was a spread of behavioural and morphological characteristics.

3.2 Tank design

To test specific aspects of the lateral line, namely how the lateral line system's sensory and morphological make up affects its user's behaviour, a tank capable of generating sustained flow was necessary. The tank also had to be capable of generating both turbulent and laminar flow to extend the study's usefulness and capture a richer data set. Other requirements were that the water be as shallow as possible to prevent fish swimming over each other to aid with IDTracker's algorithms [139], and that the test area be as large as possible to give individuals space to move freely as desired. Added constraints were given by the tank's location: it could not exceed 1m in width, or 2m in length, and that it had to be raised off the floor to allow cleaning to take place underneath. The tank needed to have a strong steel frame as it was built to be able to withstand the 600kg of water that it could hold when full. Internal wall positioning was inspired by convergent nozzles and the design of most wind and water tunnels [26, 34]. This design was employed to help speed up flow coming into the test section as well as helping to laminarize it.

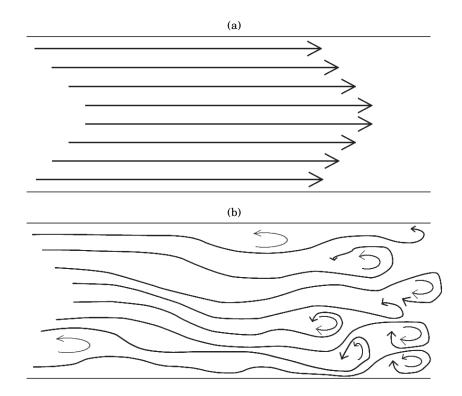


Figure 3.3: Differences in laminar and turbulent flow. a) Graphical representation of laminar flow, showing straight streamlines and no rotational motions. b) Graphical representation of turbulent flow, showing the rotational motions in the water and the formation of eddies and vortices.

Water levels were initially planned to be 0.1m deep, leading to a total water volume of 200L.

3.2.1 Tank simulations

The experimental area of the tank was simulated in OpenFOAM, using blueCFD-Core 2017 for Windows. A simulated mesh measuring $1.25 \ge 0.6 \ge 0.21$ m was generated to house the experimental area. This mesh area was meant to match the width of the area (0.56m) plus the wall thickness (0.02m), and to simulate the water depth (0.2m) while leaving some space above to better represent the freestream flow expected at the water surface in the real tank. 0.05m and 0.1m are included before and after the experimental area respectively to allow flow to interact with the flow straightener grids. Simulations were run for 100 seconds to allow flow to fully develop. Simulations of the turbulent regime included 9 cylindrical gaps in the mesh, positioned 0.003m downstream from the first flow straightener grid and spread equidistantly across the width of the area. The simulations used the Semi-Implicit Method of Pressure Linked Equations (SIMPLE) algorithm coupled with the Reynolds-Averaged Navier-Stokes (RANS) equations and the k-omega turbulence solver.

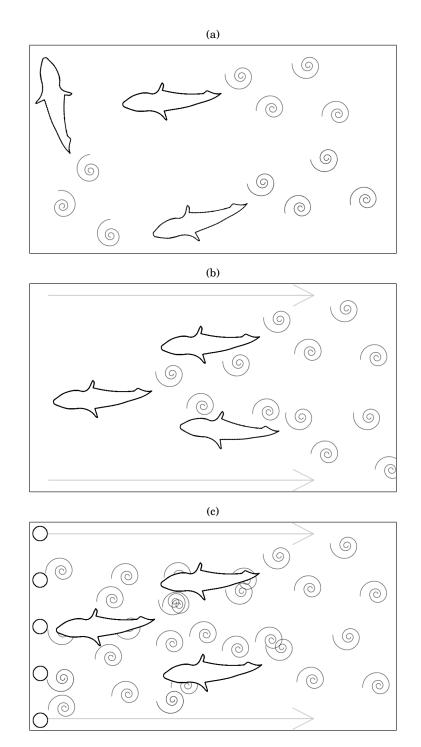


Figure 3.4: Expected flow regimes in different tank set-ups. a) Depiction of expected wakes behind fish swimming in static water. b) Depiction of expected wakes behind fish swimming in laminar flow. c) Depiction of expected wakes behind fish swimming in turbulent flow, where turbulence is generated by a line of cylinders positioned upstream. In b) and c), arrows indicate presence and direction of water flow. In static water, fish are not aligned, making it difficult for wakes to be detected by neighbours. In turbulent water, the vortices shed by the upstream cylinders are interspersed with the vortices shed by neighbouring fish. This makes it difficult for individuals to determine if what they are sensing is caused by a neighbour or is background turbulence.

3.2.2 Tank construction

Initially, a series of pond or aquarium pumps were included to generate the flow within the tank, and a first attempt was made using 2 3000 litre/hour pumps and a 1400 litre/hour pump in series. However, this only achieved a flow rate of 2 litres per second, leading to a flow speed in the tank of approximately 0.02m/s. On top of that, the hoses for the pumps were very narrow, the 1400 litre/hour pump had an inlet of 25mm and an outlet of 20mm while the 3000 litre/hour pump had a 25mm inlet and outlet, which is not a good configuration for moving a large amount of water evenly. When this set-up was tested, it was seen that water left the pump at high speeds creating a jet of water that very quickly came to a standstill, while water entering the pump was only picked up from a few millimetres in front of the hose, and globally, there was no flow within the tank.

To generate a consistent level of flow, a greater volume of water must be moved at slower speeds and so the design above was conceived; this design is similar to what is used by water tunnels and other flow tanks [26, 34, 159]. We used a 40lb/ft outboard motor due to a combination of factors including propeller size, current draw and cost. This motor is expected to be able to move 300kg of boat and occupants at approximately 4mph (1.7m/s) and so it is expected that even after frictional forces and gravitational losses, this motor will be able to generate enough flow for the tank's purposes. A more powerful motor was unsuitable due to having a larger diameter propeller that was unable to fit inside the pipe system. The motor was initially powered by a 12V 100A/h battery, but due to the current of 34A, it proved unable to complete a full day of experiments as well as having a noticeable drop in power, and therefore flow speed, as battery levels decreased. It also required between 18 and 24 hours to fully charge again. A power generator was used after this, running at 13V to give the motor extra power; higher than this caused the motor to overheat and was deemed unsafe. This method was much more sustainable and experiments could run for 10 hours a day comfortably.

3.2.3 Experimental arena

The experimental area measured 1.210 x 0.56m with a water depth of 0.2m. A plastic mesh was placed across the upstream end of the arena to act as a flow straightener and help flow laminarise. A baffle was placed just upstream from this, between the mesh and the inlet pipe, for the same purpose. For the turbulent treatment, turbulence was generated by vertical clear plastic rods of diameter 32mm attached to the downstream side of the flow straightener. A second plastic mesh was positioned at the downstream end of the flow straightener to keep fish from entering the pipes of the re-circulatory system.

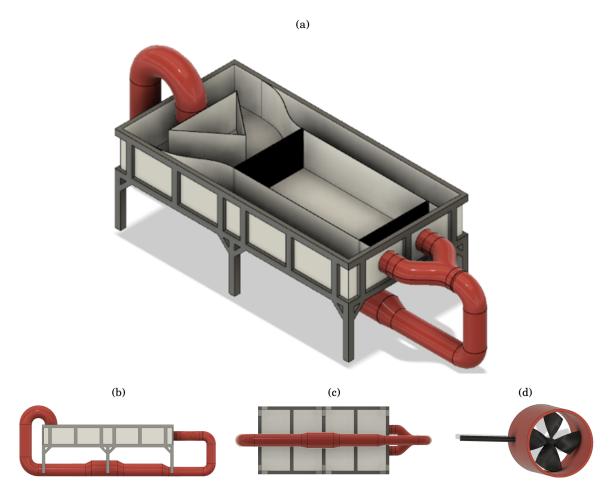


Figure 3.5: CAD design depicting the tank used for behaviour experiments. (a) An isometric view of the flow tank with the downstream end of the tank at the bottom right of the image (b) A side view of the flow tank that more clearly shows the enlarged section of pipe that housed the propeller that drove the flow. (c) A bottom view of the flow tank. (d) A cut out view of the enlarged section with the propeller inserted.

3.3 Tank characterisation

Due to the nature of the experiment, it was important that the tank be able to generate both laminar and turbulent flow, and that the difference between them be noticeable to the test subjects and quantifiable. This was verified in both simulation and practice.

3.3.1 Simulations

Simulations were created to examine the expected flow in the tank in the two different regime types that we hoped to be able to create. This was done using the Semi-Implicit Method for Pressure Linked Equations (SIMPLE) algorithm coupled with the Reynolds-Averaged Navier-Stokes equations, and using the Shear-Stress Transport (SST) k-omega turbulence model. This

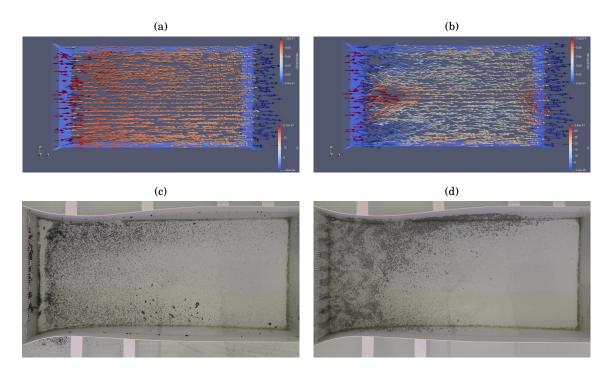


Figure 3.6: Tests of the experimental area of the flow tank. (a) Simulated predictions of laminar flow in the test area, k = 0.25617. (b) Simulated predictions of the turbulent flow in the test area, k = 0.30121. (c) A still from footage of an experimental PIV test of laminar flow in the test area, where particles appear to be moving relatively smoothly downstream. (d) A still from footage of an experimental PIV test of turbulent flow in the test area, where the swirl patterns in the particles seem to indicate vortices present.

set-up was chosen for its improved efficiency in finding a solution, while still remaining accurate. Initial simulations examined the tank for its ability to create laminar flow. Conditions were given as an inflow speed of 0.1m/s and the simulation was allowed to run for 100s. In Fig. 3.6(a), the time shown is at 99 seconds, and flow appears laminar, with a constant flow velocity of about 0.1m/s in the test area. Flow stays this way for the whole simulated time. Here, the average value of k, the turbulence kinetic energy, is 0.25617. The turbulent test area was examined under the same conditions, with cylindrical sections of the simulation mesh removed to imitate placing a cylinder into the flow, seen in Fig. 3.6(b) These cylinders were placed immediately behind the flow straightener grid. As can be seen, the flow in the turbulent test case is noticeably more turbulent than the laminar case, with its average value of k being 0.30121. This verification step is important as it indicates that the design is suitable for use and will be able to generate the necessary flow regimes at the expected speeds when built.

3.3.2 Particle Image Velocimetry

A series of tests were undertaken in the tank using a very basic form Particle Imaging Velocimetry (PIV). Several different particle types were trialled: polystyrene balls, glass beads and plastic flakes. Each proved useful in some respect: the polystyrene floated so provided good surface flow information, the glass beads were heavy and sank giving information about deeper flows, while the plastic flakes both floated and were held in a suspension giving information about a range of depths. All also had drawbacks: the polystyrene and plastic flakes tended to clump due to static, and the glass beads were too heavy for the flows to carry very far thus losing downstream information. Overall though, the plastic flakes were the best for visualising the flows.

In the laminar regime flow test in Fig. 3.6(c), black plastic flakes were added to the tank upstream and allowed to float downstream into the test area with the flow. There is a relatively even distribution of particles spread across the bottom of the area, with some extra deposition along the sides. This could be due to one of several factors including friction with the walls slowing water here causing the flakes to deposit more easily and irregularities in the way that the flakes were added to the flow upstream leading to non-uniform distributions downstream. Conversely, it could also be due to higher flow speeds by the walls carrying particles further before they deposit them; the two outlet pipes are spaced either side of the centre so would contribute to a region of slower flow in the centre towards the back of the tank. Patterns of how the plastic flakes have fallen to the area floor do not show signs of turbulence, as there are no circular or looping patterns.

In the turbulent regime flow test in Fig. 3.6(d), we can see similar trends with more material being present along the edges, particularly the upper edge; this material is floating on the surface and it is likely that static has caused it to be attracted to the walls in this case. Looking at the way that the material has been deposited along the test area floor, there is evidence of vortices being shed by the turbulence generators (plastic tubes) in the looping and curved shapes seen in the flakes.

3.4 Experiment methodology

3.4.1 Housing and maintenance

Cichlids were bred at the University of Hull by Alan Smith and Domino Joyce. A number of adult female *Aulonocara* were added to a tank containing adult *Otopharynx* of both sexes. 2 broods of approximately 33 fish total were taken from this mixing as the F1 hybrids. These fish were then kept together in a separate tank and subsequent broods were collected from there; these were the F2s. 10 individuals from each of the parent species were housed separately in 90L tanks and approximately 100 hybrid individuals were housed in a 720L tank. A further 90L tank held approximately 20 individuals of the species used as companion fish, *Hemitilapia oxyrhynchus*. All tanks were kept on a recirculating water system at 23°C and a 12-12 light-dark cycle. They

were fed a varied diet, consisting of ZM large granular pellets, tetra tropical flake, frozen blood worm, frozen prawn, frozen brine shrimp (+ brine shrimp with supplements such as spirulina, garlic, aloe), vegetarian diet blister packs, cichlid diet blister packs, mysis, krill, daphnia, white mosquito larvae and tubifex.

3.4.2 Experimental conditions

Trials took place between May and August 2018. Each trial consisted of one individual of the hybrid or parent species (the focal individual) and four individuals of the companion species. The five fish were netted from their stock tanks into the experimental tank and given 10 minutes to acclimatize with no flow. Trials were then run for 20 minutes at an average flow speed of 0.07m/s. Flow speed was determined by basic video-based particle image velocimetry (PIV), in which 3 recordings were taken of particles moving with the flow. In each of the 3 video recordings, the distance covered by 3 different particles in a set period was recorded and averaged. The final value is an average across the 3 videos. The system was controlled by a power generator set to 13V so flow speed was easily fixed. After this time period, the flow was switched off again and the fish were given a further 10-minute rest period. During these 10 minutes, the turbulence generators were either removed or inserted, depending on which treatment (turbulent or laminar) was given first. The flow was then switched back on for the second 20-minute trial. Each group was thus tested in both turbulent and laminar treatments, with half experiencing laminar first and half experiencing turbulent first (randomly assigned). Treatment order was also divided such that half of the individuals with blue coloration, assumed to be breeding males, experienced laminar first, with the same approach used for the plain colored individuals, assumed to be females or juveniles. After the testing, the focal individual (i.e. hybrid or parent) was placed in isolation in a smaller 45L tank to await further steps of the experiment, while the companion individuals were kept separate for the remainder of the day to prevent them being tested again. All procedures were approved by the University of Bristol Ethical Review Group (UIN/17/005).

3.4.3 Recording conditions and video analysis

Recordings were made using a Panasonic VX870 camera, filming in 4K at 25 fps. The camera was suspended at a height of 1.48m above the base of the experimental tank. The camera was zoomed so that the experimental arena filled the entirety of the screen. The camera filmed in 9 minute segments, and these were stitched together to form a single 20 minute video per trial, and quality was reduced to 1080p, all using ShotCut (https://shotcut.org/). Individual fish trajectories were then tracked using idTracker version 2.1 [139], which gives individual fish an X-Y coordinate in each frame that corresponds to its instantaneous location within the tank. Importantly, idTracker maintains the identity of the individuals within a trial.

3.4.4 Quantifying behavioral parameters from video

X-Y coordinates were analyzed in MATLAB R2013b and mean nearest neighbor distance, mean nearest upstream neighbour and mean nearest neighbour within a field of flow detection were calculated for the focal fish; mean group radius was also calculated. Mean nearest neighbor was calculated by determining the distance between all individuals in every frame, then taking the lowest of these values and storing them in a string; the mean was found from this string. Upstream nearest neighbour used the same string of lowest values, but excluded values from individuals that were not in front, while to find those in the flow detection field, values were excluded from both those not in front and those further than 50mm either side. Group radius was calculated by finding the center point of the group (the mean of all of the individual's coordinate points) in each frame then calculating the distance to the individual furthest from the centre. Each video was watched manually in idPlayer [139] to verify that the identity of the focal fish was maintained within the two 20-minute trials each focal fish was tested in.

3.4.5 DASPEI staining and lateral line imaging

After three focal fish were tested, which was usually within approximately three hours but occasionally overnight, focal individuals were transferred to a DASPEI solution of concentration 0.01mg/ml where they were left for 30 minutes. They were then euthanized using a Schedule 1 method: submersion in a 300mg/L solution of tricaine methanesulfonate (MS-222) for 10 minutes, followed by destruction of the brain with a sharp implement. Each individual was then transferred to a platform placed 363mm underneath the Sigma 18-200mm f/3.5-6.3 lens on a Canon 550D DSLR camera; the manual zoom was adjusted so that the fish occupied the entire screen. The camera was connected to a laptop and controlled by the Canon EOS Utility Software, allowing all adjustments to zoom and focus to be made on the laptop screen. A Royal Blue lamp (465nm) was directed at the fish to excite the DASPEI stain. A yellow glass filter (longpass filter, 500nm) was placed in front of the camera lens to remove interference from the excitation light to allow the emission light to be seen more clearly. Multiple stills were taken of each individual at a resolution of 5184 x 3456 with the lamp redirected to highlight different areas of the fish to ensure that all DASPEI labels were visible. These images were then compiled using the ImageJ (https://imagej.nih.gov/ij/) stack feature to generate a single image showing all areas of the fish highlighted. The result was a lateral view of the whole fish.

3.4.6 CT scanning and pore structure analysis

After the DASPEI staining process all individuals were prepared for CT scanning using a Nikon XTH225ST micro-Computed Tomography (microCT) system. Fish were scanned two at a time, each scan using 3141 projections and a voxel size of 20-30µm. CT scan parameters were determined following preliminary scans of similar specimens, and careful inspection of

the cranial pores following reconstruction. Stacks of images were imported into VG Studio 3.0 (Volume Graphics GmbH) and reconstructed into a 3D model. From these 3D reconstructions, 2D images were captured from the ventral head perspective and lateral head perspective (on the left side of the fish). Additional work by Duncan Edgely (University of Bristol) used graphical morphometrics to determine the area of all the pores in the head lateral line systems for each individual scanned [49].

3.5 Experiment results

3.5.1 Behaviour

Behavioural experiments were run to observe the collective behaviour of individuals within the study. Nearest neighbour distance, nearest upstream neighbour distance, nearest neighbour within the field of flow detection, and group radius were calculated for all individuals for each

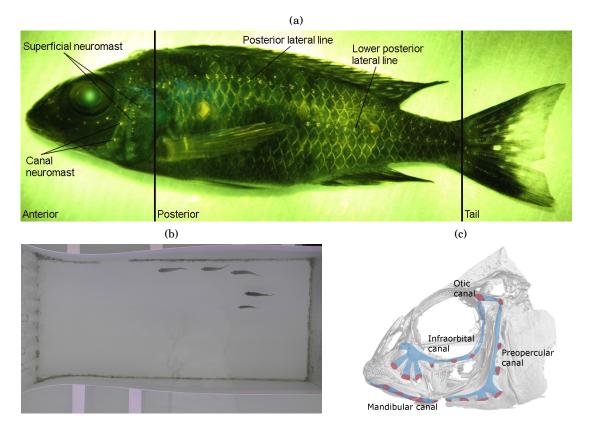


Figure 3.7: The three elements of the experimental work. (a) A side view of a hybrid individual, with labels indicating the visual appearance of the different types of neuromasts and the locations from which they were counted. (b) A still from footage of a behavioural trial where the individual furthest downstream (right) was the target individual. (c) A 3D reconstructed image of the cranial lateral line system of a hybrid with the different lateral line regions marked.

		Nearest	Nearest Neighbour	Nearest Neighbour	Group
		Neighbour (mm)	Upstream (mm)	Field of View (mm)	Radius (mm)
All	μ	93.98	123.65	119.9	207.27
	σ	61.27	63.96	75.49	74.11
Hybrids	μ	90.77	121.92	118.57	209
	σ	50.32	53.39	64.85	70.02
Aulonocara	μ	66.14	86.92	73.59	166.6
stuartgranti	σ	19.4	27.89	27.47	47.76
Otopharynx	μ	158.78	182.77	185.38	234.17
lithobates	σ	123.42	125.84	142.35	112.61

Table 3.1: The mean and standard deviation of the behavioural variables for all study individuals and for each of the groups.

Table 3.2: The mean and standard deviation of the neuromast variables for all study individuals and for each of the groups.

		Anterior superficial neuromasts	Anterior canal neuromasts			Lower superficial neuromasts	Lower posterior canal neuromasts	Tail neuromasts
All	μ	73	11	146	28	59	17	82
	σ	24.8	6.6	37.5	2.4	15.2	1.9	50.3
Hybrids	μ	72	10	150	28	61	17	83
	σ	23.5	6.6	37.3	2.5	15.4	1.9	53.1
Aulonocara	μ	58	14	131	26	51	16	71
stuartgranti	σ	25.5	7.2	34	1.8	12.1	1.7	30.8
Otopharynx	μ	99	8	114	27	56	18	78
lithobates	σ	16.7	3.7	19.4	1.7	12.9	1.4	34.5

Table 3.3: The mean and standard deviation of the pore structure variables for all study individuals and for each of the groups.

		Dentary pore	Otic pore	Orbital pore	Preopercular
		area (mm²)	area (mm²)	area (mm²)	pore area (mm ²)
All	μ	0.258	0.77	0.368	0.91
	σ	0.093	0.201	0.087	0.247
Hybrids	μ	0.251	0.75	0.364	0.875
	σ	0.069	0.159	0.062	0.152
Aulonocara	μ	0.432	1.149	0.54	1.501
stuartgranti	σ	0.101	0.193	0.052	0.232
Otopharynx	μ	0.152	0.584	0.236	0.652
lithobates	σ	0.029	0.089	0.03	0.079

frame in the video. An average for each trial was also calculated.

As can be seen, the hybrids tend to exhibit median characteristics in comparison to the two parents (Fig. 3.1). This is the result that we expected to see, but this initial examination only contains information about the mean and standard deviation, so further work is needed to conclusively say that the hybrids do have traits that span between the two parents. This further work and its results are presented next in section 3.5.4.

3.5.2 Neuromast Imaging

Results from the DASPEI staining and photography provided clear images of the position and number of both superficial and canal neuromasts across the head, trunk and tail of all individuals in the study, as seen in Fig. 3.7(a). Neuromast data was divided into seven categories: the anterior superficial neuromasts, the anterior canal neuromasts, the posterior superficial neuromasts, the posterior canal neuromasts, the lower posterior superficial neuromasts, the lower posterior canal neuromasts and the tail neuromasts. The anterior lateral line system refers to those neuromasts on the head, while the posterior lateral line system refers to those on the trunk. The lower posterior lateral line system refers to those on the trunk. The lower posterior lateral line system refers to those on the tail. Canal neuromasts are seen as larger, more diffuse spots of fluorescence while superficial neuromasts are seen in each category.

Again, we see that the hybrids typically show traits that are between those of the two parents. However, in some categories, most notable the number of superficial neuromasts along both trunk lateral lines, we see that the hybrids actually have an average that is higher than either parent. This is a common occurrence when creating hybrids, known as transgressive segregation [132, 149].

3.5.3 Pore Structure

The head area was divided into 4 different lateral line regions: the preopercular, the otic, the mandibular, and the orbital, with the location of each being noted on Fig. 3.7(c). The results from the CT scanning and pore structure morphometry reveal similar trends to those seen in the neuromast imaging, with hybrids showing median characteristics compared to the extremes of the parents (Fig. 3.3).

3.5.4 Characterisation

Mean values for every individual were visualised in a raincloud plot to verify that, as a group, there was the full range of characteristics we expected to see. Raincloud plots were also created using data from the parent species who also underwent the behaviour experiments and neuromast imaging to allow for comparisons between the three groups and to better understand how hybridisation had made the offspring different from the parents. These raincloud plots are useful to include in addition to the information in the tables already seen, as they show a more complete picture of the inter-specific variation.

Data from the behaviour experiments revealed that in each case, the hybrids found the middle ground between the two parents (Fig. 3.8(a)-(d)). There was a single set, the mean nearest neighbour distance, where the lowest value of the hybrid's data set is slightly lower than that

of the parent's, but this is not unusual given the higher means that were seen in several of the trunk neuromast data sets (Fig. 3.8(a)). Additionally, the vast majority of this set is still within the expected bounds. It is interesting to note the much reduced variation in the *Aulonocara* in comparison to the *Otopharynx*, particularly Fig. 3.8(b) & 3.8(c). The increased distance to upstream nearest neighbour seems to indicate that the Otopharynx prefers to stay further downstream. This is likely due to its less sensitive lateral line making it harder to get as close to an upstream fish without risking a collision, which is negative for both individual and shoal. It could also be due to the reduced flow speeds, and reduced turbulence in the turbulent treatment, downstream that the 'narrow' lateral line phenotype of the *Otopharynx* may find easier to take information from. It is also possible that, despite the mesh that was placed in front of the outflow pipe, the fish were drawn to the pipe opening, as it may appear similar to the *Otopharynx*'s natural habitat. Observations of footage show minimal time where test individuals, both *Otopharynx* and otherwise, appear fixated on the mouth of the pipe however, instead showing a tendency to move constantly around the majority of the tank, with a slight preference for the upstream corners.

Likewise, the raincloud plots of the different neuromast variables show similar trends with the hybrids possessing characteristics between those of the two parents (Fig. 3.10(a)-(c) & Fig. 3.9(a)-(d)). In some cases, we see a few outliers whose traits are more extreme that either parent, but this is common in hybrids [149], and the majority remain within the bounds. The tendency for hybrids to show more extreme characteristics than either parent is known as transgressive segregation [132, 149]. Transgressive segregation can explain traits that fall both above and below the expected range, as when two 'positive' alleles come together, they can result in something that is greater than either of the original two, while the opposite is true for two 'negatives'. In our findings, these extreme cases occur most often when the two parent species show similar numbers for the particular trait, i.e. the lower trunk superficial neuromast numbers and the tail neuromast numbers. In both of the examples given, the two parents show very similar distributions, while some of the hybrids possess traits outside of the range seen within the parents. Such an evolutionary model is advantageous, as the creation of the new transgressive traits in a pool of otherwise similar traits creates the opportunity for diversification and for better adaptation to the existing and to new niches. It has been shown that transgressive traits are most often seen when breeding between domesticated or in-bred populations [149], where individuals are likely to be genetically similar; therefore on this occasion the presence of the transgressive traits can be said to be positive, as it indicates the similarity between the parent species. We do still see differences in the head lateral line however, which is the primary region of diversification between the two species.

It must be noted that we identified an unusual relationship between the number of visible anterior canal neuromasts and the size of the individuals. It is unlikely that individuals are losing these neuromasts as they grow, with studies showing that canal morphology becomes fixed during juvenile stages [195, 197]. Speculating on why increasing fish size could lead to fewer visible anterior canal neuromasts leads us to two possibilities. First, increasing fish size comes with a thickening of the skin around the head, and a thickening of the canal bone structures [50], both of which would prevent fluorescence from being viewed properly. Second, a recent study has associated increased neuromast activity with increased mitochondrial activity [140]. They did this through the use of aminoglycoside antibiotics, which they showed to target mitochondria, particularly those mitochondria with increased cumulative activity. DASPEI works by the same mechanism, targeting the mitochondria in neuromasts to bind to. We speculate the possibility that fish with increased neuromast activity have higher mitochondrial activity in their neuromasts, resulting in greater DASPEI uptake and increased fluorescence. Further work is needed on this front.

The distribution of pore sizes is also presented. The difference in lateral line pore structure between the two parents is by far the most apparent between the three groups included in the data set (the behavioural variables group, the lateral line neuromast variables group and the pore structure variables group). Here, we see that the vast majority of the hybrids are within the expected range between the two parents, with some slight transgressive results seen in the mandibular lateral line. It is interesting to note the apparent opposite trend between this group and the behavioural variables group, with the significantly larger range and average pore sizes seen across the variables in the Aulonocara corresponding to the much reduced average and range of nearest neighbour distances and group radius, and the lower average and smaller range of pore sizes of the Otopharynx corresponding to a much greater range and average of the same. It is possible that this indicates that the Aulonocara possess an improved level of accuracy and control than their counterparts, able to swim closer without risk of collision, but further analysis of the data set will be required to confirm this. This also supports the discussion above about transgressive traits appearing more often when parents are more similar, as there are fewer individuals with transgressive traits apparent in this set of results; this highlights the differences that the diversification has caused in the heads of the different species.

Overall, hybrid fish exhibited intermediate lateral line system morphology and collective behavior, which confirms the efficacy of our segregating cross. Together, the hybrids exhibit the full range of morphological and behavioral diversity between the two parental phenotypes: the 'wide' canals and the 'narrow' canals. These results also provide evidence that a number of lateral line components, such as pore size, have a heritable component, as well as neuromast number [193].

3.6 Conclusion

This chapter details the development of a rich new data set, containing information about all aspects of the lateral line in 96 cichlid hybrids that showed high levels of variation, with 10 of each of the parent species of the hybrids for comparative purposes. It also details the construction

of a custom built tank used to determine the behavioural tendencies of the individuals in the study. Characterisation of this dataset has shown that the methods we used and the data that we collected is suitable for further work to look for associations between morphology and behaviour. We have shown the similarity between the parent species and also revealed the differences in anterior lateral line morphology, as well as showing that the hybridisation process has created a generation of individuals that display significant variation, with the vast majority of that variation occurring within the expected range, and with the parent's traits acting as upper and lower bounds. This dataset could act as a new resource in the study of the lateral line system, as it will allow us to effectively test for links between morphology and behavior, with benefits that are twofold. Firstly, we generate morphological variation along a spectrum between two extremes, rather than testing between two distinct groups, as in a solely interspecific study. In such studies, there is the risk that differences in behaviour arise from other interspecific differences instead of morphological ones. Secondly, by using a segregating cross, we can begin to uncorrelate the responses of the different phenotypes.

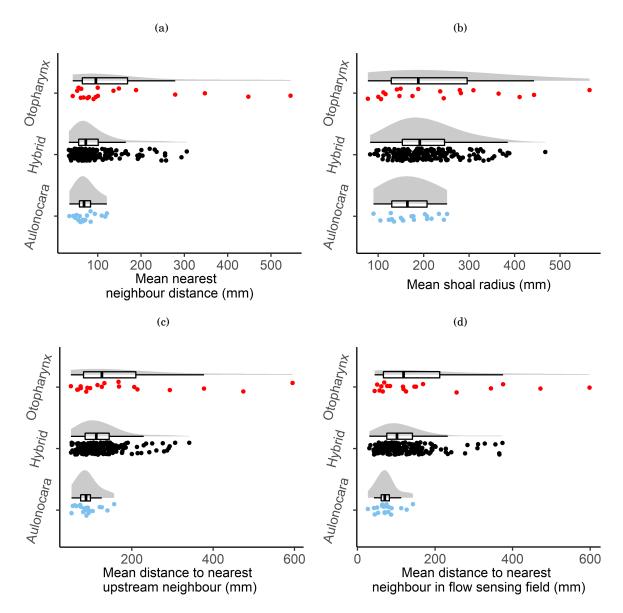


Figure 3.8: Behavioural data for each of the individuals in the study, organised into groups based on species for (a) The mean nearest neighbour distance. (b) The mean group radius. (c) The mean distance to nearest upstream neighbour. (d) The mean distance to nearest neighbour within the flow detection field. Graphs here use data from both laminar and turbulent trials. The raincloud plots consist of a probability density function (top in light grey), a boxplot (central in black) and a jittered scatter plot using the raw data (bottom in colour).

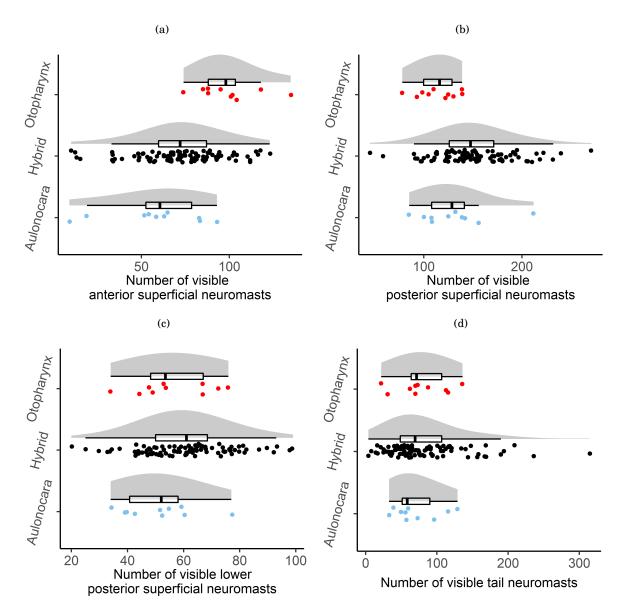


Figure 3.9: Superficial neuromast data for each of the individuals in the study, organised into groups based on species for (a) The number of anterior superficial neuromasts. (b) The number of posterior superficial neuromasts. (c) The number of lower posterior superficial neuromasts. (d) The number of tail neuromasts. Graphs here use data only from the laminar trials; turbulent trials are not included to avoid duplicate results. The raincloud plots consist of a probability density function (top in light grey), a boxplot (central in black) and a jittered scatter plot using the raw data (bottom in colour).

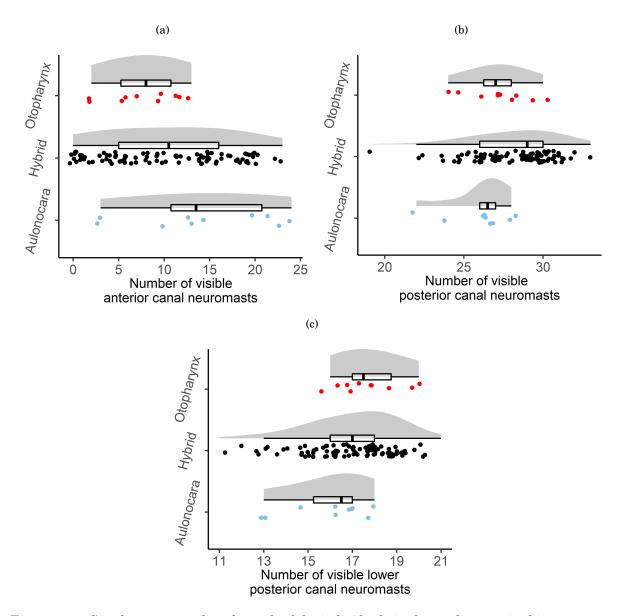


Figure 3.10: Canal neuromast data for each of the individuals in the study, organised into groups based on species for (a) The number of anterior canal neuromasts. (b) The number of posterior canal neuromasts. (c) The number of lower posterior canal neuromasts. Graphs here use data only from the laminar trials; turbulent trials are not included to avoid duplicate results. The raincloud plots consist of a probability density function (top in light grey), a boxplot (central in black) and a jittered scatter plot using the raw data (bottom in colour).

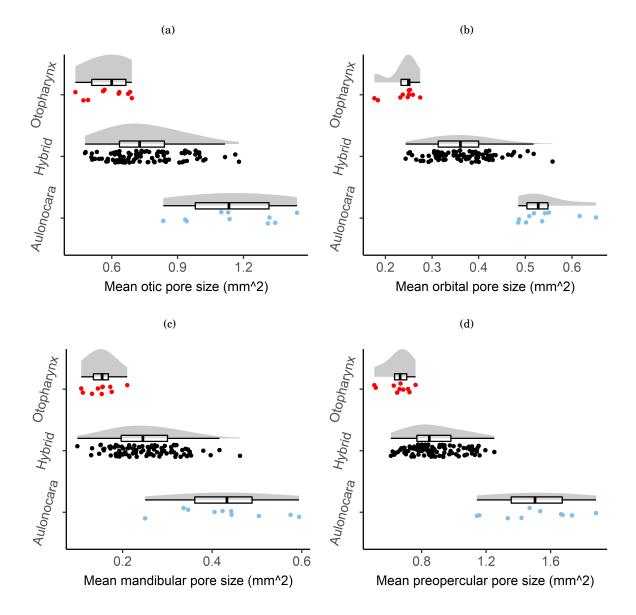


Figure 3.11: Pore size data for each of the individuals in the study, organised into groups based on species for (a) The mean size of the pores in the otic lateral line. (b) The mean size of the pores in the orbital lateral line. (c) The mean size of the pores in the mandibular lateral line. (d) The mean size of the pores in the preopercular lateral line. Graphs here use data only from the laminar trials; turbulent trials are not included to avoid duplicate results. The raincloud plots consist of a probability density function (top in light grey), a boxplot (central in black) and a jittered scatter plot using the raw data (bottom in colour).



THE EFFECT OF MORPHOLOGY ON BEHAVIOUR

FIGURE or we use generalised linear mixed models to look for relationships between morphological characteristics and measured behavioural characteristics within a group of hybrid cichlids and also with some members of their parent species. We then investigate conclusions drawn from these relationships in simulation.

4.1 Introduction

The lateral line system, sometimes described as a 'touch-at-a-distance' sense [45], is used by fishes to detect changes in water flow and pressure, capturing information about their surroundings. It is comprised of mechanoreceptive organs called neuromasts that are either on the surface of the skin, known as a superficial neuromast, or within a lateral line canal, known as a canal neuromast [17, 42]. Superficial neuromasts are mainly used to detect water flow velocity, while the canal neuromasts are used to detect changes in the water flow velocity, primarily caused by turbulence [99]. These sensory organs are spread over the head, trunk, and tail of the fish and can differ considerably among species in number, distribution and structure [69, 99, 162].

The lateral line system plays an important role in a number of behaviors, including prey detection [69, 80, 81, 126], alignment to flow [127], mate selection [118, 183], conspecific aggression [30, 183] and shoaling [136, 142]. Additionally, it appears to be essential in situations where other senses are impaired, including detection of prey in dark [33, 80, 83, 106, 128, 163, 164, 166, 167], or turbid [37, 152] conditions, as well as for detection of benthic prey in or on substrate [165]. Fishes are also able to sense vibrating obstacles [20, 79, 122, 130] and their neighbours, even well enough to shoal, when unable to see [136, 142]. When deprived of their lateral line through surgical methods or chemical treatment, a number of behaviours are altered or lost including normal shoaling ability [55, 136, 142], selective predation behaviours [163–165], competitor assessment [30, 183] and mate selection [118, 183].

It must be noted however, that some of the experimental techniques used above have their drawbacks. The work by Partridge and Pitcher [136, 142] concerning the saithe (Pollachius virens) only ever cut the lateral line at the operculum, which disables only the posterior lateral line system. Other work has used chemical treatments of either aminoglycoside antibiotics (gentamicin and/or streptomycin), or cobalt chloride to ablate the neuromasts in the lateral line system [30, 33, 80, 106, 118, 127, 163–165, 183]. While these treatments are no doubt effective at inactivating the lateral line, some studies claimed to inactivate only the canal neuromasts (through use of gentamicin) [127, 174], but more recent work has shown that this ablates the entire lateral line [28, 187]; aminoglycosides antibiotic treatments also showed damage to hair cells within the auditory system [28]. Cobalt chloride has also recently been noted to be toxic to a number of species of fish that experienced significant detriment to vital processes after even low exposure [29, 78, 114, 135, 155]. Even what is considered a safe dose for lateral line ablation has a 15% mortality rate in zebrafish [177]. Additionally, cobalt chloride has been shown to damage hair cells in the olfactory system [29], resulting in possible confounding effects [68].

Here, we use the novel approach of exploiting the large amount of variation that occurs between second generation hybrids to explore the relationship between lateral line morphology and sensory perception driving collective behaviour. For this approach, we make the assumption that the differences in behaviour come about as a direct result of the differences in morphology. It should be acknowledged that behaviour, especially collective behaviour is very complex and that there are often many inputs mediating any one behaviour. However, this approach takes steps to mitigate this complexity and make it easier to draw out trends. By exploiting naturally occurring variation, we remove the need for chemical or physical ablation, which, as seen above, can have potentially negative side effects [28, 29, 114]. By using a single hybrid species, we also help to remove the issues seen in interspecific studies, where behavioural differences can arise simply due to individuals being from different species. This approach does still retain the factor that different individuals will display different 'personalities', which will result in different behaviours, but this factor exists in all of the above methods, and in fact, in all studies with live animals. With enough test individuals, we can reduce the effect of individual tendencies on the final results.

The parent species of this cross, *Aulonocara stuartgranti* and *Otopharynx lithobates*, are Lake Malawi cichlids that were selected for their divergent lateral line morphology [49]. They are a part of a recent adaptive radiation, in which hundreds of ecomorphologically-divergent species have emerged over a relatively short evolutionary timescale [112, 180]. Such adaptive radiations are characterized by pronounced changes in morphological traits associated with their divergence, including their lateral line systems [49, 111]. The *Aulonocara* is widely recognized as an example of a species with a 'widened' canal morphology [92, 163–166], while the *Otopharynx*

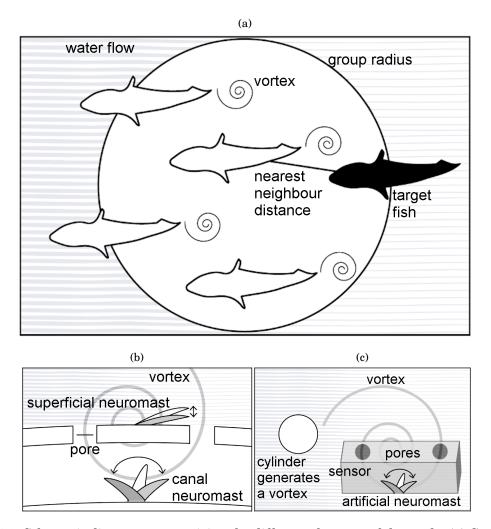


Figure 4.1: Schematic diagram summarizing the different elements of the study: (a) Group of fish shedding vortices with the response variables used in the experiment marked (nearest neighbor distance and group radius). (b) Response of superficial and canal neuromasts to a vortex when in the presence of background flow. The superficial neuromast is saturated by background flow, whereas the canal neuromast is unaffected by the background flow. The canal structure filters out any background laminar flow (pale grey lines) while allowing turbulent flows like shed vortices to be detected more clearly. (c) A cylinder can be used to generate vortices (approximate to those generated by an upstream fish, albeit in different positions), and an artificial canal structure containing an artificial neuromast can detect them.

is an example of a 'narrow' canal morphology (along with most other teleost fishes) [61, 185, 194]. The segregating second-generation hybrids exhibit significant variation in the lateral line between the 'widened' and 'narrow' canal morphologies of their parents, which allow for the uncorrelating of this trait from other traits that underpin sensory perception.

Shoaling, and collective behaviour in general, provides many benefits to individuals and to the group as a whole including prey detection [73, 199], predator avoidance [74, 110, 151], reduced

energetic costs [58, 115] and social learning [137]. In the case of prey detection, a shoal will often spread out to forage, at which time, individuals are less focused on detecting each other and instead focus on finding food, but in the other cases, shoal density is typically increased [137]. A tightly grouped shoal is more effective at confusing predators [74, 110, 151], while being in closer proximity to as many neighbours as possible will allow greater information flow for social learning [74, 137]. The energetically beneficial flows generated by tail beats tend to disperse with increasing distance from the source, so staying close is beneficial on that front too. However, a limitation on proximity exists, as collisions can disrupt shoals and should be avoided [19, 55]. As such, we would expect fish in these experiments to want to group together as tightly as possible without risking collisions, and that those with 'better' lateral line systems, i.e. those with more visible neuromasts and larger canal systems, would be able to form more cohesive groups, as they will be more aware of their neighbours, and have more precise insight of the distance to them.

To quantify sensing ability, we tested each focal hybrid fish and focal subjects from each of the parent species in behaviour trials with four companion fish of a different species, Hemitilapia oxyrhynchus: another cichlid fish endemic to Lake Malawi that has been observed in field tests forming large groups [150]. Each group was tested in both laminar and turbulent flow, in a randomized order. Automated video tracking software [139] was used to extract the mean nearest neighbor distance for each focal individual and the mean group radius over time (Fig. 4.1(a)). We also quantified aspects of the lateral line system morphology of each focal fish, generating information on neuromast number and the size of anterior lateral line canal pores. This work is discussed more in depth in the previous chapter. We then tested for associations between these variables and our behaviour metrics, giving insights into the role of different aspects of the lateral line system on collective behavior. A sensory mechanism is presented whereby superficial neuromasts quickly become saturated with information due to background flow, whereas the structure of lateral line canals allows them to detect otherwise masked flow features, for example shed vortices from upstream companions (Fig. 4.1(b)). We also run simulations to investigate the filtering properties of the canal structure and how the varying pore size affects the ability to detect the vortices shed by an upstream cylinder, in lieu of the wake of a swimming fish (Fig. 4.1(c)). Together, our study sheds new light on the role of the lateral line in mediating collective behavior of fish and takes the first steps towards a novel design of simple artificial lateral line

4.2 Statistical Analysis

A series of Generalized Linear Mixed Models (GLMMs) was created, with each model relating one of the morphological variables detailed in the previous chapter (number of visible neuromasts, pore size, etc.) to one of the behavioural variables (nearest neighbour distance, group radius). In statistics, a GLMM is an extension of the Generalised Linear Model (GLM) that includes a term for random effects. A GLM is a method of ordinary linear regression that has been generalised by relating the response (dependent) variable to the linear model (explanatory variable plus errors) through the use of a link function. In a GLM, the outcome of any response variables, Y, is assumed to follow the distribution of one of the probability distributions in an exponential family, such as a normal distribution, a Poisson distribution, a binomial distribution (when the right conditions are met), *etc*. The explanatory variables then dictate the mean, μ , of the distribution. As a function this looks like:

$$E(Y|X) = \mu = g^{(-1)}(X\beta)$$

where E(Y|X) is the term for an exponential family distribution where Y is the response variable distributed according to E and conditional on X, μ is the mean of the distribution, g is the link function, and $X\beta$ is the linear predictor: a linear combination of unknown parameters, b.

As already mentioned, a GLMM adds terms to include random effects. Random effects in the model can be considered any element where the outcome is dependent on a random phenomenon. After including this term, the function now looks like this:

$$E(Y|u) = \mu = g^{(-1)}(X\beta + Zu)$$

where E(Y|u) is again the term for an exponential family distribution where Y is the response variable distributed according to E, but now conditional on u, μ is the mean of the distribution, g is the link function, and $X\beta + Zu$ is the linear predictor. Here X and β are the fixed effects design matrix, and fixed effects respectively, and Z and u are the random effects design matrix and random effects respectively.

The GLMM models are now set up to be able to capture and display how changes in each of the different terms affects the overall relationship between the explanatory and response variables. Fig. 4.2 shows an example of a typical output from a GLMM when computed in R (version 3.6.1).

R version 3.6.1 [146] was used to generate the GLMM series using the glmmADMB package [2, 59]. A negative binomial distribution was used as both response variables were right-skewed; the overdispersion parameter was checked to be approximately equal to 1 for all models using the glm.nb function in the MASS package [188]. These models included a number of additional explanatory variables: whether each trial was in turbulent or laminar flow, which of the turbulent or laminar treatments had come first for that individual, a term to control for body length, and the individual's ID (where the individual with ID 1 was the first fish to be trialed, 2 was the second, etc.). The ID of the fish was included as a random effect throughout as each focal fish was tested in both laminar and turbulent flow. Additional models were made where body size was not included as an explanatory variable, and instead an additional model with body length as the main effect was included for comparison.

```
> summary(m1)
Call:
glmmadmb(formula = Shoal.Radius ~ scale(Head.Superficials) +
    Turbulent.Laminar + Trial_order + scale(Length) + (1 | ID)
    data = data1[is.finite(data1$Shoal.Radius), ], family = "nbinom")
AIC: 2482.5
Coefficients:
                            Estimate Std. Error z value Pr(>|z|)
                                          0.0348 150.95
                                                            <2e-16 ***
(Intercept)
                               5.2465
scale(Head.Superficials)
                              0.1087
                                          0.0301
                                                    3.61
                                                            0.0003 ***
                             0.0369
                                          0.0268
Turbulent.LaminarTurbulent
                                                    1.38
                                                            0.1680
Trial_order2nd
                              0.0323
                                          0.0268
                                                    1.21
                                                            0.2273
scale(Length)
                             -0.0237
                                          0.0298
                                                   -0.79
                                                            0.4268
Signif. codes: 0 '***' 0.001 '**' 0.01 '*' 0.05 '.' 0.1 ' ' 1
Number of observations: total=226, ID=116
Random effect variance(s):
Warning in .local(x, sigma, ...) :
    'sigma' and 'rdig' arguments are present for compatibility only: ignored
Group=ID
            Variance StdDev
(Intercept) 0.07507
                      0.274
Negative binomial dispersion parameter: 29.445 (std. err.: 4.5225)
Log-likelihood: -1234.25
> |
```

Figure 4.2: The output of a GLMM when computed and called in R (version 3.6.1 [146]). The first shows the formula used; next is the AIC score; the 'coefficients' section gives the contribution that each of the different terms has on the final model, where scale() terms affect the slope and all other terms affect the intercept position; the following section shows the effect of the random term(s); the negative binomial dispersion parameter is next and measures how much the model fluctuates around a mean value; finally, the log-likelihood value is shown, which gives an estimate of the goodness of fit.

A downside of GLMMs is that they do not have any information about the likelihood of a given model being effective at explaining an observed trend. In other words, the GLMM might reveal a highly positive correlation between the explanatory and response variables, but in reality, this is coincidental and varying one will likely not have the expected effect on the other. A method is needed to determine how likely a model is to be true and how much better it is likely to be than other models. For this, we use the Akaike Information Criterion (AIC). This method estimates the prediction error of a model by determining the amount of information lost in the process of fitting the model to the data: the less information lost, the higher the quality of the model. The AIC value should be minimised, so by examining the formula, it is evident that model complexity is penalised, while 'goodness of fit' is rewarded. In this way, the AIC method deals with the issues of both under-and over-fitting. The formula for this is as follows:

$$AIC = 2k - 2ln(\hat{L})$$

where k is the number of estimated parameters in the model, and \hat{L} is the maximum value of the likelihood function for the model. The likelihood function (sometimes just likelihood) gives the probability of the observed data as parameters of the mathematical model.

By using AIC, we can determine the relative quality of the models to each other, but this gives no information about absolute quality. To overcome this, an additional model is included that is called the null model, where no explanatory variable is included, only the random variables and those variables being controlled for. All models are compared against this model, and if the null model scores better, then it shows that the observed results in the given model are not significant. If a given model has a score of 2 or more lower than the null model, then the observed trend is statistically significant, and is considered to have strong support. The model with the lowest score (assuming that score is 2 or more lower than the null model) is considered to be the best supported. We compared the difference in corrected AIC (AICc) values using the ICtab function in the bbmle package [22]; we considered a model with an AICc of two or more lower than the null model (or \triangle AICc 2) to have strong support. By comparing AICc values in this way, we determined which aspects of our focal fishes' sensory morphology best predict collective behaviour. Fig. 4.3 shows a typical model comparison using AIC.

4.3 Statistical Analysis Results

4.3.1 Anterior neuromast number and collective behavior covary

To investigate the role of the lateral line system in collective behaviour, we constructed models to test for the effect of lateral line morphology (visible canal and superficial neuromast counts, and pore size measurements) on collective behavior metrics (mean group radius, mean nearest neighbor distance, mean distance to nearest upstream neighbour and mean distance to nearest neighbour in the field of flow detection). Each model included only one morphological variable due to collinearity among them, and the likelihood of models were compared using AICc [74, 191]. When testing for the influence of visible neuromast number on mean nearest neighbor distance, we found the most support for the model with the number of visible anterior canal neuromasts as the main effect (Fig. B.1,B.2), which associated more canal neuromasts on the head with a reduced nearest neighbor distance (Fig. 4.4(a)). When testing for the influence of visible neuromast support for the model with the number of visible neuromast on the head with a reduced nearest neighbor distance (Fig. 4.4(a)). When testing for the influence of visible neuromast support for the model support for the model with the number of visible neuromast number on mean group radius, we found the most support for the model with the number of visible neuromast number on mean group radius, we found the most support for the model with the number of visible anterior superficial neuromasts as the main effect (Fig. B.3,B.4), which associated more superficial neuromasts on the head with less cohesive groups (Fig. 4.4(b)). We also found support for increased numbers of visible posterior superficial neuromasts (on the upper trunk) leading to

Group Radius - All - Scaled for body size

m1 0.0 7 – Head Superficials – +ve
m9 1.9 8 - Head Superficials (interactions) - +ve (+ve)
m10 4.8 8 - Head Canal (interactions)ve (-ve)
m2 5.8 7 - Head Canalve
m3 6.8 7 – Trunk Superficials – +ve
m11 8.5 8 - Trunk Superficials (interactions) - +ve (-ve)
m8 10.3 6 - Null
m20 10.3 6 – Length – +ve
m21 10.6 7 - Length (interactions)ve (+ve)
m5 10.9 7 - Lower Trunk Superficials - +ve
m4 12.1 7 – Trunk Canals – -ve
m6 12.2 7 – Lower Trunk Canals – +ve
m7 12.3 7 - Tail - +ve
m13 12.7 8 - Lower Trunk Superficials (interactions) - +ve (-ve)
m12 13.0 8 - Trunk Canals (interactions)ve (-ve)
m14 14.2 8 - Lower Trunk Canals (interactions) - +ve (-ve)
m15 14.3 8 - Tail (interactions) - +ve (+ve)

Figure 4.3: Comparing AIC scores of GLMM models against a null model in R (version 3.6.1 [146]). From left to right, the first column gives the model name, the second column gives the AIC score, the third column gives the number of variables in the model, the fourth column gives the name of the explanatory variable (as well as indicating if the model includes the interactions between the given variable and the level of turbulence), and the fifth column indicates the direction of the correlation between the explanatory and response variables (as well as indicating what effect increasing the level of turbulence has on that correlation, when an interaction term is included).

looser groups, and increased numbers of visible anterior canal neuromasts causing tighter ones (Fig. B.3,B.4).

As only hydrodynamic stimuli from upstream fish will be detectable by the focal fish, we repeated the analysis, restricting the nearest neighbor distance metric to only those periods of time where the test individual was downstream of at least one of its companions. The most likely models showed higher numbers of visible anterior canal neuromasts were associated with closer upstream neighbors (Fig. B.5,B.6). However, in both the full and hybrid-only datasets, the models including the interaction between visible anterior canal neuromast number and flow regime (laminar or turbulent) were best supported by a substantial margin. In trials with turbulent flow, the number of visible anterior canal neuromasts had a larger negative effect on the mean nearest neighbor distance than in laminar flow (Fig. B.5,B.6), meaning that individuals with more visible anterior canal neuromasts tended to swim closer to their nearest neighbour in turbulent flow than in laminar flow. Individuals with fewer visible anterior canal neuromasts showed similar mean nearest neighbour distances in laminar and turbulent flow.

A further restriction was added to remove parts of the trial where upstream fish were presumed to be too far to either side for the target fish to detect them using their lateral line, i.e. outside the flow detection field of the focal individual. Within the full dataset of all studied

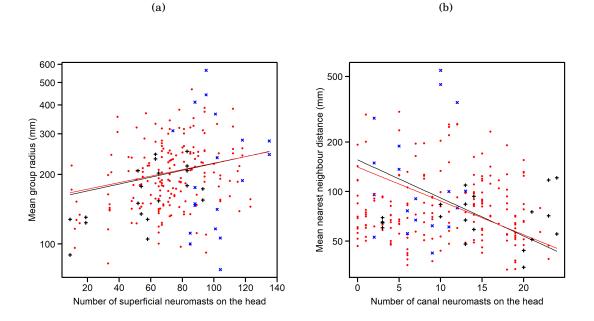


Figure 4.4: The best supported associations between the behavioural variables and the morphological variables pertaining to the visible neuromast counts: (a) the effect of number of visible anterior superficial neuromasts on the group radius and (b) the effect of the number of visible anterior canal neuromasts on the mean nearest neighbour distance. In both, *Otopharynx lithobates* is shown by blue crosses, *Aulonocara stuartgranti* is shown by black pluses, and the hybrids are shown by red dots. The black line shows the line of fit for the entire data set, while the red line shows the line of fit for a data set of only hybrid individuals.

fish, models with the number of visible anterior canal neuromasts were best supported, with the model also including the interactive effect of the flow regime (laminar or turbulent) being most likely; support for this model was also present using the hybrid-only dataset (Fig. B.7,B.8). This is the same pattern as seen in the upstream nearest neighbour distance analysis. When considering hybrids alone, the model with the number of visible posterior superficial neuromasts had the most support, with a greater number of posterior superficial neuromasts being associated with greater distances to nearest neighbors. However, this pattern was not strongly supported by the dataset including all studied fish (Fig. B.7,B.8).

Since body length and the number of neuromasts in the lateral line system were significantly correlated (See Appendix A), to test for the relationship between behavior and absolute visible neuromast number we repeated our analysis excluding body length as a covariate, instead including it as a stand-alone model (Fig. B.9,B.10,B.11,B.12). Finding a relationship between the absolute number of visible neuromasts and nearest neighbour distance or group radius (instead of using the number of neuromasts per unit length) has the potential to be more useful for engineering applications as it removes the need to scale neuromast numbers to the size of the platform using them. In these models, we found strong support for a larger numbers of visible

anterior and posterior superficial neuromasts being associated with an increased group radius in both datasets, and also found support that an increased number of visible anterior canal neuromasts leads to decreased group radius (Fig. B.11,B.12). However, there was no support for models showing associations between any neuromast variables and nearest neighbor distance (Fig. B.9,B.10). There was also no evidence that models with body length as a main effect had greater support than the null models (Fig. B.9,B.10,B.11,B.12), making it unlikely that variations in body size have any significant effect on collective behaviour.

A possible explanation for the importance of the anterior structures is that flow around the head is less disrupted by the fish's body; as flow moves further down the body of the fish, boundary layer effects and self-generated flows, particularly from the pectoral fins, will begin to alter and disrupt the flow information an individual is attempting to capture [200]. For these reasons, from a sensory perspective, a fish may gain more by extracting data from flow around the head. This may also have the additional benefit of allowing the fish to respond to the stimulus more quickly, as a fish will usually be aligned to the flow's source or facing upstream, and the head will be the first part of the fish in contact with the flow stimuli. As such, having more anterior canal neuromasts may allow more data to be gathered about the fish's surroundings and in turn allow for better control. Increased numbers of superficial neuromasts will give an individual better information about the surrounding flow velocities [45, 99], which could give broad warning of obstructions (like companions) ahead with reduced flow velocity behind them. Individuals with more anterior superficial neuromasts may be more sensitive to these reduced velocity areas and naturally distance themselves from them, resulting in more widely spaced fish. Previous work has highlighted the importance of lateral line mechanoreception in preventing collisions within a group, with some lateral line-ablated fish colliding with their companions with sufficient force to stun themselves [55, 136, 142]. Collisions can have significant negative effects for the individual so an increased sensitivity to slower flow regions may act to avoid physical contact with neighbours.

In the analysis of both the distance to nearest upstream neighbour and the distance to nearest neighbour in field of flow detection, it was found that increasing turbulence had the result of causing fish to swim closer to their nearest neighbour. Referring back to Fig. 3.4, we can see that the turbulent regime introduces a new level of complexity. The new vortices formed by the turbulence generators interfere with the vortices shed by the swimming fish, and as such, it is likely that a trailing fish will need to move closer to its upstream neighbour to be able to sense it effectively in these more complex conditions. Work by Partridge and Pitcher saw that increasing flow speed caused the shoal to swim more closely together [141]. Increasing flow speed is known to cause increasing levels of turbulence, so the two results can be said to support each other.

An unusual relationship was identified in the previous chapter, where larger fish apparently possessed fewer visible anterior canal neuromasts than smaller fish. This was deemed to be unlikely as it had not been previously observed in the literature [195, 197]. However, all models

here have body size controlled for, either as a covariate or with a stand-alone model for comparison, and as such, it can be said that the associations identified are likely present. Referring back to the possibilities discussed in the previous chapter, it seems feasible that if thicker skin, present on the larger fish [50], is able to block the fluorescence from getting out, it could also block hydrodynamic signals from getting in as effectively. If the flow stimuli required to sense neighbouring fish are effectively being muffled by this thicker skin, it could explain why fish with fewer visible anterior canal neuromasts in our dataset tend to swim further from their neighbours, as they are not as able to sense the shed vortices with their lateral line. This again ties in with fish wanting to be as close to one another as possible while in a group, but it seems when lacking the precision necessary for this, they opt to increase distance to avoid collisions. The other possibility discussed relates increased use of neuromasts with increased mitochondrial activity within the cells of these neuromasts. DASPEI is known to bind to the mitochondria in neuromast cells, and the possibility of increased mitochondrial activity resulting in increased DASPEI uptake was floated. If this were the case, then the increased numbers of visible anterior canal neuromasts in some fish would relate to increased use of these neuromasts in sensing neighbouring fish. The lateral line is likely to be more engaged in a fish swimming close to its neighbours than one swimming further from them. Further study would be needed to investigate this.

4.3.2 Fish with larger anterior canal pores swim closer to their nearest neighbors

We determined associations between mean nearest neighbor distance and mean anterior lateral line canal pore size, within four of the head canals, using body length as a covariate (Fig. B.13,B.14). Using the full dataset of hybrids and parents, models with all pore size variables (otic, infraorbital, preopercular and mandibular) received strong support, with greater mean pore size correlated with reduced nearest neighbor distances (Fig. 4.5). For the hybrid-only data, the model with the most support (otic canal pore size) was only marginally better than the null model. Testing associations with mean group radius and mean anterior lateral line pore size using the full dataset revealed larger preopercular and otic canal pore size models as predictors of a less cohesive group. In the hybrid-only data, again the otic canal was only marginally better than the null model (Fig. B.15,B.16). When implementing additional constraints on the nearest neighbors within the focal fish's field of flow detection) we found the same trends, where larger canal pore sizes predicted closer neighbors, but again only in the full dataset (Fig. B.17,B.18,B.19,B.20).

Repeating analyses, but excluding body length as a covariate, again found strong support that increases in pore size variables (otic, orbital, preopercular and dentary) were associated with decreased nearest neighbor distances in the full dataset (B.21), and when considering only the hybrid population there was also support for the model with otic canal pore size model as a predictor (Fig. B.22). There was some support for increased preopercular and otic canal pore size



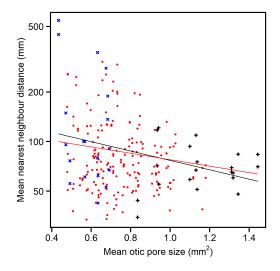


Figure 4.5: The best supported associations between the behavioural variables and the morphological variables pertaining to the pore size: the effect of the size of the otic canal pores on the mean nearest neighbour distance. *Otopharynx lithobates* is shown by blue crosses, *Aulonocara stuartgranti* is shown by black pluses, and the hybrids are shown by red dots. The black line shows the line of fit for the entire data set, while the red line shows the line of fit for a data set of only hybrid individuals.

correlating with decreased group radius in the full dataset, but the null model was most likely using the hybrid-only data (B.23,B.24).

Above, it is seen that larger canal pores are associated with a decreased average proximity to nearest neighbors (Fig. 3C) and a decreased group radius. The larger pore size allows more information from the external flow to pass into the canal system, resulting in increased signal strength within the system. This means that smaller changes in the external flow are amplified and as such more perceptible, leading to greater sensitivity overall. With this greater sensitivity, it is possible for fish to get closer to their neighbours without risking collisions. It should be noted that in cichlids the bony pores of the anterior canal system are covered with a thin membrane that blocks the majority of flow actually entering the canals; there exists only a small hole that flow can actually pass through [16]. A larger membrane however can act to amplify external signals that are acting on the pore area, making them more perceptible within the canals [16].

4.4 **Proof-of-concept simulations of the canal system**

A proof-of-concept prototype was created to investigate the filtering properties of the canal system's structure and the effect of varying pore size in order to verify the results from Section

4.3. This prototype was a rectangular box measuring 25 x 25 x 50mm with two openings on the 'front' face, this being one of the rectangular sides measuring 25 x 50mm. A physical prototype was also created and some successful preliminary tests were done by a student. The physical design used a set of stiff metal pins with skin between them that was inserted through a thin flexible membrane that allowed the pins to move freely in response to flow velocities. The other side of these pins bore a red bulb that showed equal and opposite movement to what the pins exposed to the flow experienced, allowing for flow measurement. The membrane offered very little resistance, meaning that any fluid motion within the prototype was translated to motion of the bulb. As such, no neuromast was added in simulation, and instead flow velocity was measured directly.

4.4.1 Simulating flow behind a cylinder

Computer aided design models of cylinders of varying sizes were created using Autodesk Fusion version 2.0.8816. The cylinder was positioned at the origin. Stl files were generated from these models. Snappyhexmesh was used to convert the stl files to the required text file format for simulation. OpenFOAM (BlueCFD-Core 2017) was used to simulate flow speeds at 0.1, 0.5 and 1m/s over 400 seconds. The Semi-Implicit Method for Pressure-Linked Equations (SIMPLE) algorithm coupled with Reynolds-Averaged Navier-Stokes (RANS) equations were used to get a steady-state approximation of the wake. A k- ω model was used to calculate turbulence. Results were exported as excel files containing the velocity data from every point in the mesh. Further analysis was done in MATLAB (2018b) to determine the optimum point in the simulation to take readings at. This was done by taking the pressure and flow velocity data from every point in the simulation at each of the 400 time steps, then calculating the range, the standard deviation, and the variance of the data at each point; total velocity was measured as well as the x, y and z components. For each type of data, a heat map was generated, with the x and y axes representing the x and y dimensions of the simulation and the colours showing the given metric. It was determined that x velocity variance was likely to be the best metric, as this displayed the maximum amount of variation; where more variation occurs, there is more data available to be extracted. An additional data set was extracted from OpenFOAM using the Plot Over Line function; this was taken in the flow behind the cylinder to act as the 'expected' signal. The 'expected' signal will then act as a baseline to determine the effectiveness of the canal structure's filtering properties, and how that changes with varying pore size. R (version 3.6.1) was used to generate a violin plot to visualise this signal and make for easier comparisons; a violin plot is combination of a probability density function (mirrored about the y-axis) and a box plot (plotted along the y-axis)

In an attempt to better understand the flow dynamics that occur within a group and during following behaviours, we first simulated a cylinder in flow. A cylinder is described as a bluff body in fluid dynamics, and the formation and shedding of vortices downstream from such an

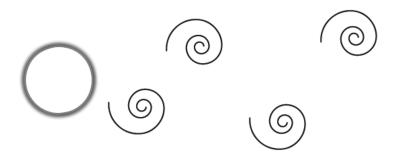


Figure 4.6: A simple diagram showing the expected appearance of a Kármán vortex street. Vortices are shed alternately from either side of the cylinder and then move downstream. At the centre of each vortex is an area of low pressure.

object is well documented [148]. While fish are not described as bluff bodies, instead typically being similar in shape to an aerofoil or streamlined body, their swimming motions have also been described forming and shedding vortices in a similar fashion to what one would see behind a cylinder in flow. Both of these phenomena, the repetitive and alternate formation and shedding of vortices, are known as a Kármán vortex street, with the key difference that above a given point, vortices that are shed behind a swimming fish rotate in the opposite direction to vortices that are shed behind a cylinder; this is known as a reverse Kármán vortex street [46, 103, 113]. The point after which the reverse Kármán vortex street forms is given by the Strouhal number, which is dependent on speed and tail beat frequency. Therefore, our approximation of an upstream neighbour through the use of a cylinder is suitable, but we should acknowledge and anticipate the potential difference in position that our sensor would be behind an actual swimming fish.

4.5 Kármán vortex street

The Kármán vortex street is a repeated pattern of swirling vortices that are alternately shed from either side of a bluff body in flow, seen in Fig. 4.6. A Kármán vortex street's formation is dependent on the Reynolds number of the body and flow it might occur behind and in. The Reynolds number is defined as:

$$Re = U * L/\nu,$$

where U is the background (freestream) flow speed, L is the characteristic length of the body, and v is the kinematic viscosity parameter of the fluid. This is defined as:

$$v = \mu/\rho$$

where μ is the free stream fluid dynamic viscosity and ρ is the fluid density.

A Kármán vortex street will form behind a cylinder over a range of Reynold's numbers, quoted as between $50 < Re < 3e10^5$. This translates to approximately 0.0005m/s up to 3m/s, for a cylinder of 100mm diameter. There is a region between $3e10^5$ and $3e10^6$ where transition occurs from the vortex street to completely turbulent flow, after which vortices will not appear [148]. Our chosen flow speeds in the simulations were between 0.1 and 1m/s, with a dynamic viscosity of $1e10^{-6}$, giving a Re between $1e10^4$ and $1e10^5$, which is within the range given above.

4.5.1 Simulating a canal structure and varying pore size

Computer aided design (CAD) models of the prototype, with five different pore sizes, were positioned behind a 100mm cylinder using Autodesk Fusion version 2.0.8816. The prototype was centered on the origin, with the cylinder placed 200mm away in the upstream direction and 40mm to one side. Stl files were generated from these models. OpenFOAM was used to simulate flow speeds of 0.5 m/s over 400 seconds. Snappyhexmesh was used to convert the stl files to the required text file format for simulation. Velocity data within the prototype was extracted from OpenFOAM using the Plot Over Line function. This line ran between a point in the centre of the internal face opposite the pores to a point perpendicular to this 15mm away in the middle of the 'canal' section of the prototype. This is in the same place as the velocity data taken from behind the cylinder to enable comparisons. Due to the very low resistance offered by the membrane in the physical prototype, the velocity data extracted here is taken to represent the motion of the pins in the simulation. R (version 3.6.1) was used to generate further violin plots to compare the velocity within the canal structures to the 'expected' signal taken from in the flow behind the cylinder.

4.6 Simulation results

4.6.1 Vortex shedding behind a cylinder

To better characterise the appearance of flow behind a cylinder, as an approximation of how flow may look behind a swimming upstream neighbour and in anticipation of determining how to best utilise a bio-inspired flow sensor, we generated a number of simulations of cylinders in flow with a range of characteristics. Variations were centred around a cylinder of 100mm diameter with flow speeds of 0.5m/s, and diameter and flow speed were then varied independently of each other: cylinder size between 50mm and 150mm and flow speed between 0.01m/s and 1m/s. It should be noted that simulations were run using simple assumptions, and so exact wake characteristics are not properly captured here. However, they do serve to provide estimates of wakes, and notably in the range of speeds most useful for the sensor use. More information about the assumptions made is given in the following chapter, in section 5.2.2.

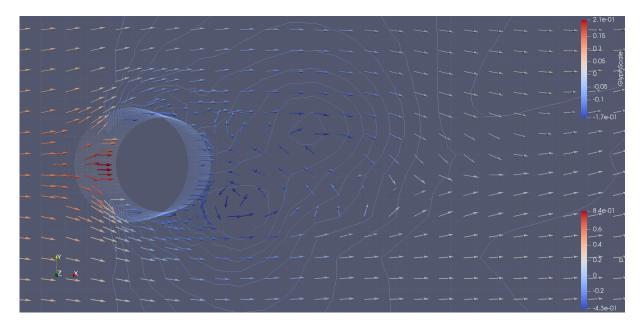


Figure 4.7: Simulated flow behind a cylinder with 100mm diameter at 0.5m/s, with glyphs showing the flow velocities and contour lines showing the different pressure levels.

Fig. 4.7 shows a cylinder of 100mm in flow of 0.5m/s. Referring back to Fig. 4.6 for comparison, we can see from the velocity glyphs (arrows) that a Kármán vortex street is occurring; the pressure contour lines also show areas of low pressure in the centre of each vortex. Three areas of low pressure are visible in the simulation, the first appearing on the top half of the cylinder then appearing alternately in the flow downstream from there. Focusing on the velocity glyphs, we see two rotational motions in the low pressure areas, as well as the beginnings of a new rotation in the low pressure area on the top surface of the cylinder, which indicates where the next vortex will form and be shed from.

Fig. 4.8 shows the effect that varying the cylinder size has on the vortex street, with flow speed fixed at 0.5m/s. Immediately evident is the effect that this has on the size of low pressure areas and the resulting vortices that form. The low pressure areas are minimal in Fig. 4.8(a), while in Fig. 4.8(b) they are significantly larger, and the same is true for rotational motion shown in the glyphs. This is quite intuitive, as it is expected that there would be a strong correlation between cylinder size and corresponding vortex. There also appears to be a correlation between cylinder size and how far the vortex street propagates downstream: flow in Fig. 4.8(a) returns to normal in a much shorter distance than in Fig. 4.8(b). A larger simulation was run for the cylinder of diameter 150mm at 0.5m/s (Fig. D.2) to show the additional distance downstream that flow is affected. This difference is likely due to the greater change in momentum that the flow contacting the larger sphere will experience, where energy is transferred from downstream velocity and instead into the circular motions of the vortices, and as such, will take longer to regain its momentum.

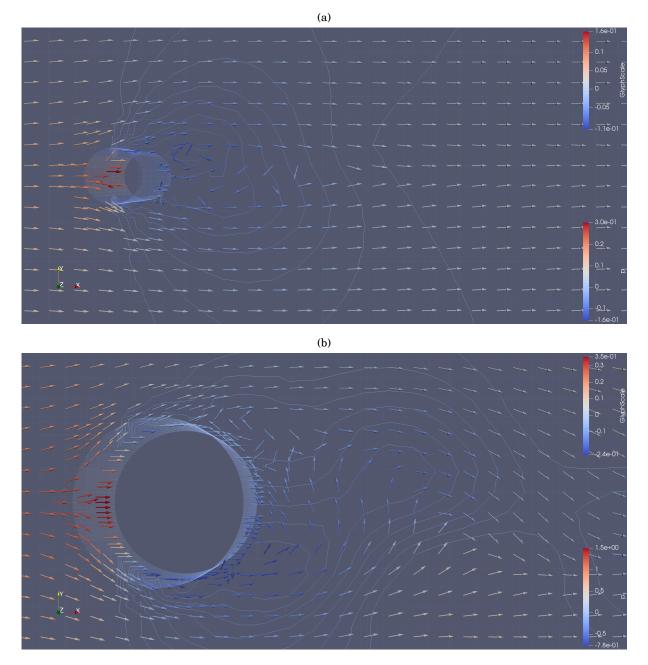


Figure 4.8: Simulated flow behind different cylinders at 0.5m/s, with glyphs showing the flow velocities and contour lines showing the different pressure levels. a) Simulation of a cylinder with diameter 50mm. b) Simulation of a cylinder with diameter 150mm.

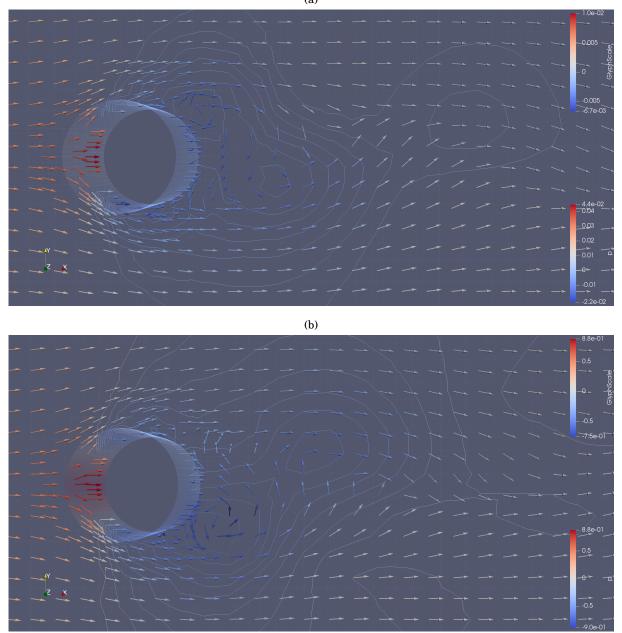


Figure 4.9: Simulated flow behind cylinders with 100m diameter at different speeds, with glyphs showing the flow velocities and contour lines showing the different pressure levels. a) Simulation of a cylinder at flow speed 0.1m/s. b) Simulation of a cylinder at flow speed 1m/s.

(a)

Fig. 4.9 shows the effect that varying the flow speed has on the vortex street behind a cylinder; cylinder diameter was fixed at 100mm. When looking at the size of the negative pressure areas, we can see that the areas of lowest pressure are comparable between the two simulations, and that while the actual pressure is lower when flow speed is higher (1m/s in Fig. 4.9(b)), the general appearance and gradient of the contour lines is quite similar. Vortices appear to travel further downstream in the same amount of time in the Fig. 4.9(b), but this is expected due to the faster flow. Additional larger simulations (Fig. C.1 & C.3) seem to show that the effect of the vortices remains more pronounced for a greater distance downstream in the slower flow, but that faster flow takes longer to return completely to normal. This is again likely due to the differences in momentum. Both streams are affected equally by the presence of the cylinder, but the higher velocity flow has more momentum to begin with and loses a smaller proportion of that as it interacts with the cylinder, resulting in higher velocity flow immediately after, and a faster return to the freestream velocity. The momentum of the surrounding water also contributes significantly to speed up the slower water through frictional forces. Together these smooth out the rotational motions making them less obvious. However, faster flow is naturally more turbulent, so instabilities remain present for longer. It is interesting to note that in all cases, the vortices appear to be shed from and propagate down a line that sits at approximately +/- 80% of the diameter of the cylinder. These results help to frame some of the conditions that a Kármán vortex street will form under, and give a general sense of how changing these conditions will affect the wake. This is useful in predicting how these changes might in turn affect flow velocities within our prototype, and any further developments to it.

4.6.2 Finding the optimum position

Analysis of flow behind the cylinder taken over the entire run revealed the positions in the flow with maximum and minimum flow speeds, as well as the positions with greatest variance. The position with maximum velocity will be the outermost edge of the vortex, where its rotation adds velocity to the flow, and the position with minimum velocity will be the inner edge of the vortex, where the rotation is in the opposite direction to the flow and so slows it. Examining Fig. 4.10, we see areas of high variance within the simulation coloured in red and can see that the position with maximum variance is also located on the inner edge of the vortex where flow is slowed. While the minimum velocity point is close to the cylinder where flow speed does not increase between shed vortices, the point of maximum variance is further from the cylinder where it can. This point of maximum variance is the point that we deemed to be the most useful place to carry out our investigations, as the relatively large and frequent changes in velocity mean that there is more information available to extract. Interestingly, it is along the line that we identified in the previous section, the +/- 80% mark, which in this case is at x = +/- 0.04m.

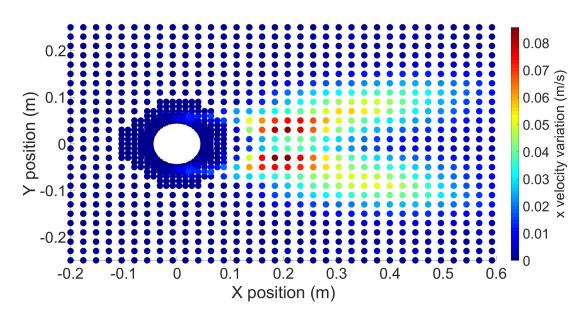


Figure 4.10: The variation in x velocities surrounding a cylinder with 0.1m diameter in flow at 0.5m/s. Blue dots represent the minimum level of variation and red dots represent the maximum variation. Variation is taken over the entire 400 second simulation.

4.6.3 Canal structures filter flow information

Results from simulations revealed that the signal from within the prototype was less affected by the background flow (Fig. 4.11). The original 'expected' signal oscillated around a mean flow speed of 0.4m/s, which is slightly slower than the background flow speed set in the simulation due to the flow being slower in the vicinity behind the cylinder. Flow speed data taken from the same location, but now within the simulated prototype showed a large decrease in the mean flow speed. The canal-like structure shields the region within the prototype from the background flow, moving in the x direction in this case, while still allowing flows as a result of shed vortices to be detected, moving in the y direction in this case. Put in a biological context, without the surrounding canal structure, a neuromast would either need to be so stiff to resist the background flow that it would not be sensitive enough to detect low velocity flows, or it would be constantly saturated by the background flow and unable to detect any information. The reduction of mean velocity seen in these results shows that the canal structure is able to effectively filter out the constant background flow, and is able to detect only the flows we are looking for: those generated by passing vortices. This highlights the associations we found between the number of visible canal neuromasts and the nearest neighbour distance, as simulation indicates that neuromasts situated within a canal structure will be far better able to detect the vortices shed by neighbouring fish.

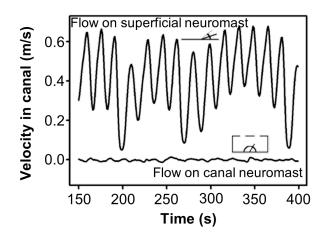


Figure 4.11: A comparison of the velocities experienced in open flow and within the 20mm pore size prototype. Diagrammatic representations of a neuromast in the different locations are included for context. The resulting waveforms show the changes in velocity over the full 400 seconds of the simulation. Both simulations have freestream velocity set to 0.5m/s.

4.6.4 Canal pore size affects sensitivity

We varied the size of the pores to test for the effect that this would have on sensitivity. We found that as the diameter of the pore increased, so too did the flow velocity within the prototype (Fig. 4.12). There is also a trend of increasing variability, with the exception of outliers at pore size 15mm. The velocities associated with the increasing pore size are still well below that seen in open flow, and so oversaturation poses no threat to data collection. As the mean velocity and the range of velocities increases, it can be expected that a neuromast will deflect to larger angles in response, thus indicating that more information is being captured from the flow. This in turn means that smaller changes in the background flow due to vortices from the upstream fish are more visible in the output, providing a greater sensitivity to stimuli. This highlights the association between larger anterior pores and reduced nearest neighbour distances, as we show here that larger pores allow more flow information to be captured, which fish in groups can use to better sense their neighbours. While the design here lacks the membrane over the pores seen in cichlids [16], we have demonstrated that the same principles can be applied.

4.7 Conclusion

These results have implications for the study of the evolution, ecology, and associated behaviors of the lateral line system of fishes. They demonstrate how it is possible to uncorrelate morphological disparity within multiple lateral line system structures, and to test the consequences of this variation on collective behaviour. They also highlight how different aspects of lateral line system morphology differentially affect collective behavior, and specifically identify the importance of

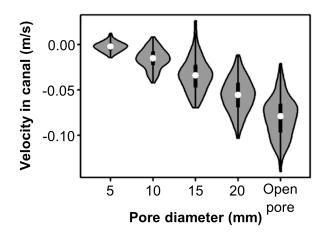


Figure 4.12: Violin plots of the velocity that was recorded within the prototype at each of the different pore sizes tested, where the 'Open pore' indicates that the entire pore-side face is removed and is meant to represent an infinitely large pore size. Freestream flow velocity was set at 0.5m/s for all cases. Data is extracted at the point where flow is reversed and so a greater response is measured with a greater negative velocity. A violin plot consists of a vertically oriented probability density function (mirrored around the centreline) and a boxplot, with the white dot giving the median, the thick black bar giving the interquartile range and the full length of the bar giving the total range.

the head structures. This result could help to explain how clupeid fish, that comprise numerous globally-important shoaling species, including herrings, shads and sardines, and have well developed anterior lateral line canal morphology [21, 85, 176] (although admittedly different to the lateral line systems seen in cichlids [49, 164, 194]), are able to coordinate their collective movement effectively in the absence of posterior lateral line canals [85, 176]. Simulations help to validate the biological work, showing the way that a canal structure can help to filter background flow noise making the canal neuromasts more sensitive to flow accelerations [45, 99], as well as giving indication that widened pores are more sensitive to these accelerations than narrow ones, which may contribute to better ability to sense neighbours. This is in line with what had been demonstrated for feeding cichlids who use their mandibular pores to hunt substrate prey [163–165]. In addition, these findings have the power to help inform the design of artificial lateral lines. Work has already been undertaken in developing biomimetic artificial lateral line systems [54, 63, 71, 84, 94, 207] and these systems have been shown to be very effective, able to localise a dipole source to high degrees of accuracy, and even determine yaw, pitch and roll angle between two neighbouring robots [211]. Much of this work is currently too complex or expensive to mass produce, however. The design and the simulation results seen here could help to create a simple, inexpensive, macro-scale sensor capable of informing minimalistic underwater robots for swarming purposes, eventually without the need for visual signals.



THE DESIGN AND OPTIMISATION OF AN ARTIFICIAL LATERAL LINE SENSOR

FFT ere we use ideas from the previous chapter to develop a novel design of canal lateral line inspired sensor and optimise it in simulation. We identify some key design elements and verify our observations with further simulations. Finally, preliminary experimental data is collected to affirm the sensor's ability to detect vortices as predicted by the simulations.

5.1 Introduction

Complex fluid dynamics in underwater environments make it difficult to design sensors that are effective at detecting and interpreting the surroundings of underwater robots. As a result, many of the underwater robotic platforms available at the moment require the use of tethers and an operator to complete the sensory tasks required of them [12, 108]. Other platforms are able to use visual processing techniques to effectively navigate autonomously, but in areas with low light or high turbidity this is more difficult [23]. Additional challenges exist when attempting to form swarms of underwater robots as they must also be able to sense and communicate with each other [18, 129, 154, 179].

To help deal with these problems, we turn to nature for inspiration. Many of the creatures found in the sea have adapted their senses for better use underwater and even developed entirely new ones. An adaptation of the auditory systems in many cetaceans allows them the use of sonar to aid in navigation [209], while fish like the Peters' elephantnose fish [31] and the black ghost knifefish [109] are able to actively generate an electric field for the same purpose. Another sense that teleost fishes posses is the lateral line [17, 42, 69, 162]. The lateral line is comprised of two types of sensory units, superficial neuromasts and canal neuromasts [17, 45, 162], that

detect the surrounding flow velocities and accelerations [45, 99]. Neuromasts are small hair-like structures that either exist on the skin (superficial neuromast) or in a system of canals that sit beneath the skin (canal neuromast); these sub-dermal canals have small openings, pores, that allow the canal neuromasts to gather information from their surroundings [42, 164]. It has been shown that some fish are able to navigate, hunt and shoal by relying solely on the lateral line [20, 33, 80, 83, 106, 142, 164, 167]. The lack of light available to cave dwelling fish and the issues of scattering and absorption that Autonomous Underwater Vehicles (AUVs) at depth or in highly turbid water experience [57, 133] share some overlap, and the cave dwellers rely heavily on their lateral lines to overcome this [83, 106]. As such, a new type of sensory suite inspired by the lateral line seems a prudent way to overcome these issues in AUVs too.

A number of biologically inspired artificial lateral line sensors do exist and have been shown to be effective [5, 48, 54, 63, 71, 84, 94, 192, 207], but they often use Micro-Mechanical-Electro Systems (MEMS) which can be difficult to manufacture [147, 172, 181]. The complexity of the manufacturing processes involved in realising many of these designs, processes that have been discussed in more depth in Chapter 2, make these sensors infeasible for mass production. Given that the ultimate aim of this project is to bring the artificial lateral line to underwater robotic swarms, a complex design and manufacture process will increase both the time and the cost required to reach the final product. In a swarm of the numbers needed to be effective in an arena as vast as the ocean, all efforts must be made to reduce these factors, otherwise the swarm will require too many resources to ever be feasible. A number of other systems exist that are able to combine off-the-shelf sensing units, particularly pressure sensors, into an effective artificial lateral line that is less complex than the systems above [44, 157, 189, 208]. However, even these systems require the use and subsequent coordination of multiple pressure sensors for effective flow sensing, which can again drive up cost. Further work is needed to create a novel design of very simple sensor that can operate effectively without requiring multiple instances of itself. Succeeding in this task could allow for the development of full shoals of low-cost underwater robots with applications in underwater inspection, canal surveying, exploration, or environmental monitoring [47, 104].

Here, we propose a new design for a simple and low-cost artificial lateral line system composed of a neuromast and bio-inspired canal structure. Our design differs from other more conventional canal neuromast designs due to its u-bend shaped front and rear facing pores; this helps filter background flow more effectively. Additionally, it is macro scale in size which makes it significantly easier to manufacture. In fluid dynamics, varying scales can drastically alter flow properties, and as a result much of the work that has come before this has stayed true to the expected biological scales. However, this project wanted to test if remaining at the microscopic scale was necessary for artificial neuromast sensors to work correctly, as such it should be considered to be lateral line inspired, not lateral line mimetic. The design also differs from previous work by using a highly flexible membrane as a fulcrum about which a stiff element will rotate, transferring force from the fluid within the sensor to the other side of the membrane. The sensor is designed to detect shed vortices, which are often formed by the swimming motions of upstream fish (natural or robotic), or obstacles. Being able to detect the vortices shed behind obstacles would give an AUV improved environmental awareness, while detecting swimming neighbours can aid in navigation and coordination. We highlight the ability of this novel canal lateral line sensor to filter background flow and its sensitivity to the shed vortices left in the wake of swimming neighbours, building on some preliminary work in the previous chapter. We demonstrate in simulation that the sensor can detect shedding vortex patterns emanating from a cylinder acting as an upstream fish or an obstacle [46, 77, 103]. We then justify the design specifications by comparing our sensor to variations reflecting each design decision. Results show the importance of all design decisions in improving similarity between the signal detected by the sensor and the original 'expected' signal; this 'expected' signal is the same as seen in the previous chapter and gives flow qualities behind the cylinder in the absence of a sensor. The end result was a 0.0155 total residual error between the normalised versions of the two time-series, and a visually similar set of results, with corresponding peaks between signals indicating detection of every passing vortex. Based on these results, we produced a physical sensor using off-the-shelf low cost parts and 3D printing and demonstrated its ability to sense shed vortices in water.

5.2 Optimising the lateral line

Chapter 4 details the initial investigation into the use of a canal structure to filter background flow and into the effects of varying pore size on sensitivity. This used a cuboid with two pores (holes) next to each other on the same face, and a hair cell within the structure on the internal face opposite the pores. Data from this showed that the canal structure was effective at filtering background flow (Fig. 4.11) and that increasing pore size increased internal flow speed (Fig. 4.12). Increased internal flow translates to increased sensitivity as it gives a greater response to the same stimuli. However, examination of the waveforms seen in Fig. 4.12 (the expected signal and the response from the 20mm pore prototype) shows that signal integrity does not appear to be well maintained, and comparing residual errors between them using normalised Euclidean distance measures we get a result of 0.207; this will act as the baseline for further optimisation. Residual errors for the other pore sizes have similar results with 0.208 for 5mm, 0.0212 for the 10mm, and 0.0207 again for the 15mm. Here, we iterate on the initial design to reduce these issues. All designs were created in AutoDesk Fusion, and then simulated in OpenFOAM at 0.5m/s. The simulated area was either 400 or 500mm (depending on the length of the sensor in the simulation) by 200mm by 250mm, using 800,103 cells. Sensor effectiveness is measured by comparing the expected and detected time-series' residual errors, determined with euclidean distance measures. After each attempt at optimisation, if the new design was shown to be more effective, it was combined with other successful designs. This process continued until no further

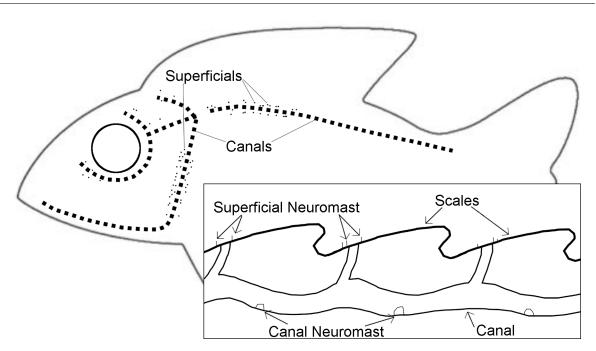


Figure 5.1: Graphical representation of a lateral line system in teleost fish.

improvement was seen.

5.2.1 Artificial lateral line design

Inspired by its natural counterpart (Fig. 5.1), our artificial lateral line sensor has a canal, two pores, and one neuromast embedded in the canal. The sensor is formed of a long curved tube with the bottom shorter part dedicated to detecting the vortex and hosting the artificial neuromast hair, while the longer part acts as the canal and neutral pressure reservoir (Fig. 5.2(a)). This neutral pressure space then allows a pressure differential to be created when the negative centre of a vortex passes the mouth, resulting in fluid accelerating out of the canal and deflecting the artificial neuromast. The design hinges around the idea of using a stiff rod to act as the neuromast, with half of this rod inside the canal and half outside, and a thin elastic membrane, positioned at the midpoint of the rod, to act as a fulcrum. In this way, fluid motion within the sensor causes the external end of the rod to exhibit an equal and opposite motion. The highly elastic membrane offers almost no resistance, allowing the neuromast to swing freely. This also removes the need to include a neuromast in simulation: fluid velocity is taken as a proxy for neuromast deflection as with minimal resistance the two will be very closely related. Dimensions were chosen to be easy to produce using 3D printing and off-the-shelf components. The sensor as a whole is 140mm long, 39mm wide and 32mm in height. The sensor is meant to align with the fluid direction, with pores opening in the opposite direction. This prevents interference on the neuromast due to water displacement (e.g. river flow) or robot motion from impacting the sensory readout (Fig. 5.2(b)).

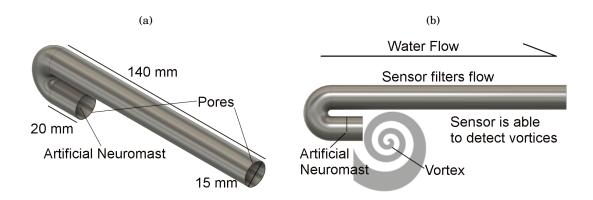


Figure 5.2: Artificial lateral line sensor design and mechanism. (a) CAD design of the artificial lateral line sensor. The sensor has two pores, a cylindrical canal of 15mm diameter, and an artificial neuromast positioned 10mm from the pore on the shorter side. (b) Artificial lateral line mechanism capturing shed vortices on the neuromast while filtering water flow. Flow is accelerated out of the sensor when the negative pressure at the centre of the vortex causes a pressure differential with the neutral pressure in the long section of canal.

5.2.2 Simulation-based experiments

To predict the expected sensory readout from the artificial lateral line and optimise its design, we simulate an environment with flow, due to robot motion or water motion, and a cylinder, to generate vortices in lieu of an upstream fish, robot or obstacle. The simulated environment was 200mm wide, 250mm deep, and either 400 or 500mm long, depending on the length of the sensor being simulated. A cylinder of 100mm diameter was included as a vortex generator. Our sensor was placed 200mm behind the cylinder and 40mm to the side of the cylinder's centre line, as analysis of flow behind the cylinder indicated that this point has the maximum flow velocity variation, and hence is the point from which the most information can be extracted (Fig. 5.3). Simulations used the Semi-Implicit Method for Pressure Linked Equations (SIMPLE) algorithm coupled with the Reynolds-Averaged Navier-Stokes (RANS) equations to get a steadystate approximation of the Kármán vortex street. The Shear Stress Transport (SST) k-w model is used for turbulence calculations. The SIMPLE algorithm was chosen for its efficiency, being able to arrive at the solution we were looking for much faster, and with much larger time steps than other algorithms, while still remaining accurate. The RANS equations are time-averaged, making them very good at finding solutions for flows that display a repeating pattern, like a Kármán vortex street. The SST k- ω model provides superior prediction of flow separation near walls but switches to a k- ϵ model in the freestream to avoid inlet turbulence properties; it is one of the most commonly used models. Data was extracted along a line in the vertical plane that extended between the two internal walls of the sensor. The data was extracted in the form of x velocities along the length of the line, which was then averaged. No neuromast is simulated as in experiment the combination of a stiff hair coupled with a highly flexible membrane as a base

makes the neuromast extremely sensitive to velocities, and as such the measured velocity can be considered a proxy for neuromast deflection. Experiments are performed using the computational fluid dynamics simulator OpenFOAM. Data was visualised using ParaFOAM, the post-processing element of the OpenFOAM software, but additional analysis was done in MATLAB: velocity data from each point in the mesh was exported to an excel file, which was then imported into MATLAB. Signal processing analysis was then done to determine which of the sensor designs was most effective at both detecting vortices and retaining signal integrity. For each design, euclidean distance measures are used to compare the residual error between the time-series of detected velocities inside the sensor and the time-series of expected velocities in the absence of the sensor. The formula for this is as follows:

$$Residual = \sqrt{\Sigma(a-b)^2}$$

where the term a - b is the difference between two vectors at the same point in the series.

This allows us to determine the total difference between two vectors (in this case our timeseries), giving a good measure of the overall difference between them. Time-series are normalised (with mean equal to 0 and standard deviation equal to 1) before residuals are calculated to make comparing them easier. The design with the lowest residual is then said to be the most optimised. Stl files were exported from AutoDesk and into OpenFOAM using the snappyhexmesh capability. A water flow of 0.5m/s was used as a realistic speed for an AUV [203], and the simulation was allowed to run for 400 seconds to allow it to reach a steady state solution.

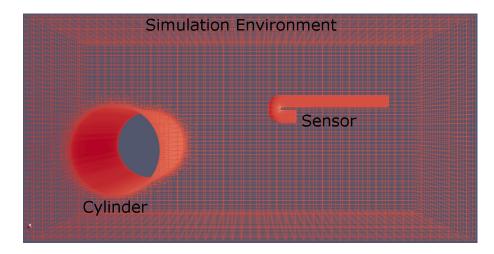


Figure 5.3: Simulated environment in OpenFOAM, including the 100mm diameter cylinder that generates the vortices and our optimised sensor design.

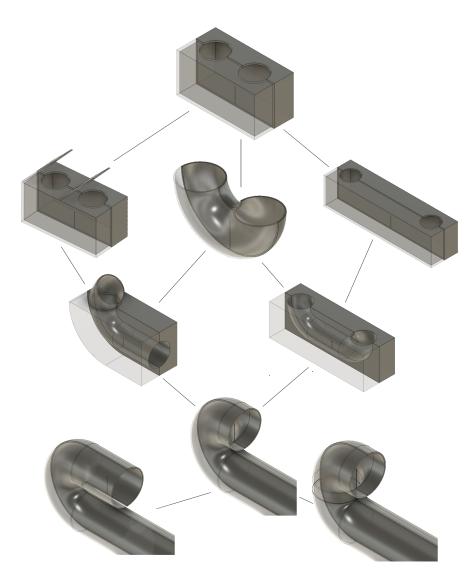


Figure 5.4: The iterative process that the sensor went through to arrive at the final optimised design.

5.3 Optimisation results

The following describes the main route that the iterative process took to arrive at the final design. Results from our initial design (Chapter 4) showed that while it was evident that the sensor could detect the presence of shed vortices, there was poor similarity between the signal that was expected and what was detected. Examination of the flow vectors around and inside the sensor over the course of the simulation showed a few major issues.

The first issue was that shed vortices affected both pores simultaneously, particularly in the early and late stages of their passing. For the set-up used in the initial simulations, the rotational motion of the vortex moves fluid into first the upstream pore (Fig. 5.5(a)), then into the

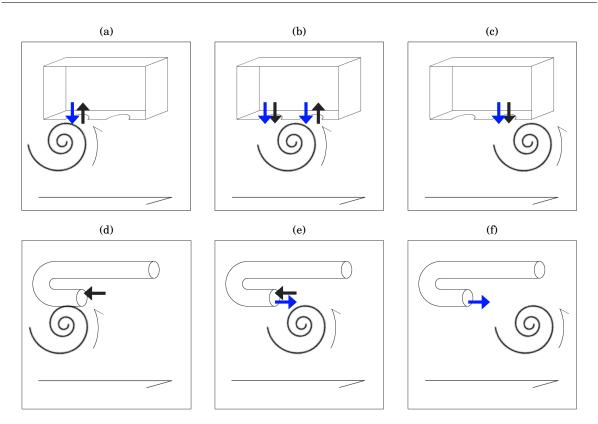


Figure 5.5: A graphical representation of the different mechanisms that affect how a passing vortex is detected. Black arrows show motion in and out of the sensor due to surrounding fluid motion, while blue arrows show motion in and out of the sensor due to surrounding fluid pressures. (a)-(c) show the time progression of a vortex passing the prototype detailed in Chapter 4, while (d)-(f) show the same for the optimised sensor.

downstream pore and out of the upstream pore (Fig. 5.5(b)), then out of only the downstream pore (Fig. 5.5(c)). In the case of a larger vortex, one would see that there would be a period of time between Fig. 5.5(a) and Fig. 5.5(b) where the rotational motion of the vortex would be moving fluid into both pores at the same time; the same will be true for some time between Fig. 5.5(b) and Fig. 5.5(c), but with fluid moving out. Concurrently to the above, the negative pressure at the vortex's centre pulls water out of upstream pore (Fig. 5.5(a)), then both pores together (Fig. 5.5(b)), then just the downstream pore (Fig. 5.5(c)). Over the course of this event, in flow without the presence of the sensor, we would expect to see a single sine wave oscillation, but it is immediately evident from the description above that this will not be the case due to the multiple variations in input and output to the pores.

The second issue was the turbulence that was becoming established within the sensor between vortices. Our sensor was originally designed to channel water in through the downstream pore and out again through the upstream pore as the vortex passed. However, when this moment is captured by the sensor, and we see the desired flow pattern, immediately after, smaller vortices

are established within the sensor that sometimes linger for long enough that they interfere with the flows of the next vortex. This also then prevents us from getting a clean sinusoidal reading.

Early attempts at optimisation were all focused around ways to encourage the flow to go in the downstream pore and come out of the upstream pore. Designs were focused around ideas such as varying the pore size (downstream pore larger than upstream), adding funnel structures to help guide the flow in the desired fashion, and adding a raised lip around the pores to better prevent flows that aren't correctly oriented from entering the sensor, to name a few. These all proved to be ineffective as previously mentioned, but there were a few designs that showed progress. These designs are shown in Fig. 5.4, along with the process that refined them to our new optimised design.

The top level of design changes were selected to counter the issues mentioned above. Left is inspired by the morphology of the scales that the lateral line is located along, with the thought process being that the plates slanted at 45 degrees would prevent the rotational flows during the early stages of a vortex from being able to enter the upstream pore, thus reducing interference on that front. Middle is meant to help channel the flow better, mimicking the curve of the vortex as well as removing spaces in which internal turbulence can develop. Right is designed to give more space between the two pores, so as to prevent the passing vortex from being able to affect both ends of the sensor at the same time. The following level combines these designs, seeing improvements each time. The design that combines all of the solutions has also taken elements further, increasing spacing between the pores by completely removing one of the pores on the face, and then also increasing the length of the sensor to prevent the vortex being able to affect the other pore at all. It also rotates the intake pore to be facing completely backwards, away from flow, taking the idea of using a scale to cover the pores to the extreme. The new design now works primarily by detecting the negative pressure at the centre of the vortex. Fluid moving back upstream is minimal, so the sensor will have little output in Fig. 5.5(d). This effect will remain minimal in Fig. 5.5(e) and the negative pressure of the vortex will accelerate water out of the canal, registering the main output, before this effect lessens in Fig. 5.5(f); the output will then move back towards neutral. There is likely to be some interference still in the output, mostly in Fig. 5.5(e), where fluid will be moving in two directions at the same time, but there is significantly less than with the previous design. This interference can be seen in the differences between the two signals in Fig. 5.6(b), particularly around the peaks.

5.3.1 Verifying the design

After optimisation, the simulated artificial lateral line sensor is better able to pick up signals from vortices shed by the upstream cylinder. In Fig. 5.6(a), each minimum in the original signal has a corresponding minimum in the signal obtained from our sensor, and this is made even clearer when comparing the normalised time-series in Fig. 5.6(b). The minima are the times when a vortex has passed our point of maximum velocity variation (200mm behind and 40mm to

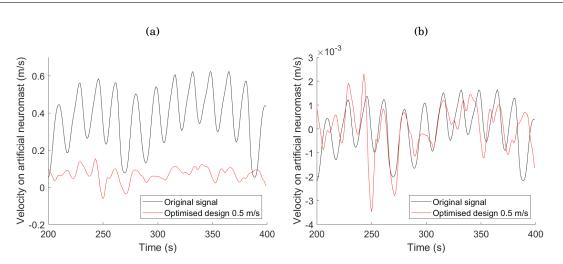


Figure 5.6: Comparisons between the velocities detected by the optimised sensor design (red) and the expected velocities (black) without the sensor present in simulation. a) The time-series b) The normalised time-series

the side of the centre point of the vortex-generating cylinder) and the upstream rotation of the vortex has slowed flow speed. Fig. 5.6(a) also shows the filtering quality of the sensor, with the detected time-series being centred around 0.05m/s. It is interesting to note that the waveform of the original signal seems to have two modes of oscillation, one higher frequency, and another lower frequency, resulting in a sine wave that follows the path of a sine wave. The sensor appears to be best at detecting the original signal in the lower velocity sections of the low frequency sine wave.

5.3.2 Fixed diameter internal channels prevent internal turbulence

We aimed to minimise internal turbulence by setting a fixed circular diameter for the internal channels. Our observation was that the internal shape of the sensor, i.e. using a square canal vs a circular canal, could lead to internal turbulence. This issue was particularly pronounced in structures with corners, as internal turbulence had a tendency to linger between vortices, adding significant noise to multiple cycles of the waveform. We theorised that removing the empty corners and instead having just a channel of fixed radius would reduce or even remove the internal turbulence levels.

Fig. 5.7(a) and (b) shows the significant improvement seen when using a circular canal design (Fig. 5.7(c)), as opposed to a square canal design (Fig. 5.7(d)). While there are parts of the square canal's time-series that appear to overlap well with that of our design's, the majority of it is different to both ours and the original signal. Comparison between the residuals reveal close to 50% more error between what is detected by the square channel compared to our final optimised design.

The change from a square canal design to a circular canal design was inspired by both biology,

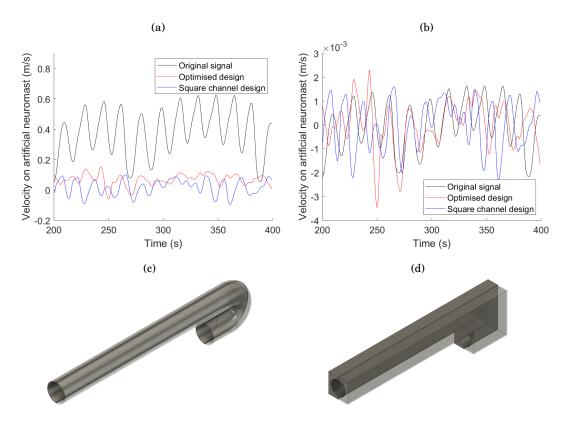


Figure 5.7: Impact of canal shape on sensory readout. (a) Comparisons between the (a) time-series and (b) normalised time-series detected by the optimised sensor design (red) and the square canal design (blue) against the original time-series (black) in the simulation. (c) The optimised sensor, with residual error between the detected and expected time-series equal to 0.0155. (d) The design with a square canal, with residual error between the detected and expected and expected time-series equal to 0.0214.

the canals seen in the lateral line are not square in shape [196], and aerodynamics, where flow around corners in square ducts is associated with high turbulence and vorticity [60, 153].

5.3.3 Rear facing pores reduce noise

The orientation of the sensor was chosen to reduce the amount of background flow (from sensor motion or laminar water flow) entering the sensor and disrupting the vortex measurement. To demonstrate the effect of orientation, we compare the optimised sensor design (Fig. 5.8(c)) against a sensor designed with a single forward-facing pore (Fig. 5.8(d)) and a single side-facing pore (Fig. 5.8(d)). Comparing errors reveals that the optimised design is approximately 20% better than either Fig. 5.8(d) or Fig. 5.8(e). Fig. 5.8(a) shows the significantly higher velocity that the neuromast in the forward-facing pore design (Fig. 5.8(d)) experiences, effectively removing the filtering property of the sensor. The side-facing pore (Fig. 5.8(d)) offers significant improvement over this, but is again not as effective as the rear-facing pore.

CHAPTER 5. THE DESIGN AND OPTIMISATION OF AN ARTIFICIAL LATERAL LINE SENSOR

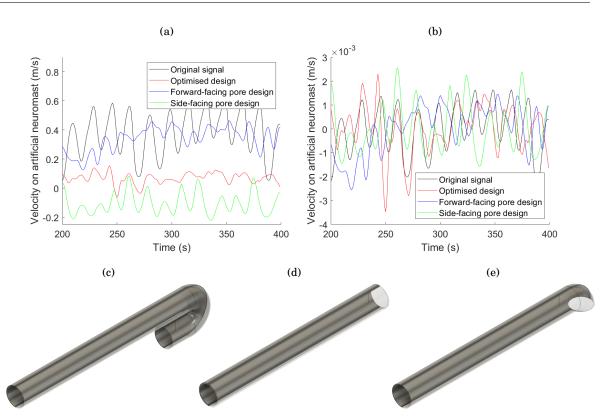


Figure 5.8: Impact of canal shape on sensory readout. (a) Comparisons between the (a) time-series and (b) normalised time-series detected by the optimised sensor design (red), the forward-facing pore design (blue) and the side-facing pore design (green) against the original time-series (black) in the simulation. (c) The optimised sensor, with residual error between the detected and expected time-series equal to 0.0155. (d) The forward-facing pore design, with residual error between the detected and expected time-series equal to 0.0199. (e) The side-facing pore design, with residual error between the residual error between the detected and expected time-series equal to 0.0199. (e) The side-facing pore design, with residual error between the detected and expected time-series equal to 0.0190.

It is interesting to note here that the rear facing pore is also seen in nature, with the channels that lead from pore to sub-dermal canal tending to face backwards, and with scales as well often occluding the pore's upstream side [196]. While there is limited data on how the angle of the canal affects how flow and turbulence is interpreted, the results here and those seen in nature seem to concur that a rear facing pore is more effective.

5.3.4 Further spaced pores result in less interference

The spacing of the pores was chosen to minimise vortices entering the pores from overlapping, leading to interference. We observed that when pores were in close proximity to each other, vortices affected both simultaneously. In real terms, this meant that both pores were experiencing an in-flow at the same time, particularly during the early stages of a passing vortex being detected, which resulted in either no velocity on the neuromast as the flows from the two pores

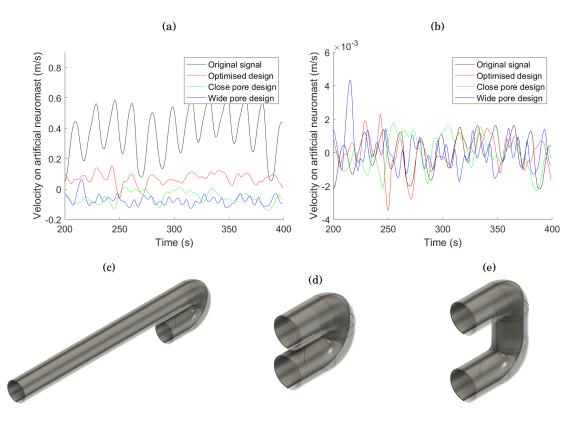


Figure 5.9: Impact of canal shape on sensory readout. (a) Comparisons between the (a) time-series and (b) normalised time-series detected by the optimised sensor design (red), the narrowly spaced pore design (green) and the widely spaced pore design (blue) against the original time-series (black) in the simulation. (c) The optimised sensor, with residual error between the detected and expected time-series equal to 0.0155. (d) The narrowly spaced pore design, with residual error between the detected and expected time-series equal to 0.0155. (e) The widely spaced pore design, with residual error between the detected and expected time-series equal to 0.0216.

cancelled each other out, or in a noisy signal. We theorised that having the two pores further apart would make it less likely that both pores could be affected by the same signal at the same time.

Fig. 5.9(a) shows that the design with the pores in close proximity (Fig. 5.9(d)) shows approximately 20% greater error than our design. Increasing the spacing between pores in a direction perpendicular to flow appears to reduce accuracy, with the widely spaced pore design (Fig. 5.9(e)) having over 25% more error than our optimised design. Both of these designs do retain their filter properties though.

Our design here tried to capture the shape of the canal system, with the long part of the sensor representing the subdermal canal part of the lateral line, and the u-bend and opening imitating the pore. The initial design and the two examples shown above are all closer in form to two pores connected to a limited section of the subdermal canal. Admittedly, to make the optimised design more bio-mimetic, the neuromast should be housed in the longer canal section,

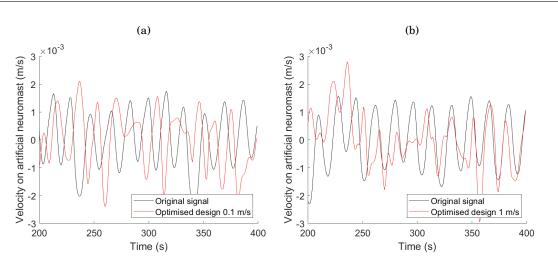


Figure 5.10: Comparisons between the time-series detected by the optimised sensor design (red) and the original waveform expected (black) in simulation, both normalised, at a) flow speed at 0.1m/s, with total residuals calculated at 0.0243 b) flow speed at 1 m/s, with total residuals calculated at 0.0243 b) flow speed at 1 m/s, with total residuals calculated at 0.0243 b) flow speed at 1 m/s, with total residuals calculated at 0.0243 b) flow speed at 1 m/s, with total residuals calculated at 0.0243 b) flow speed at 1 m/s, with total residuals calculated at 0.0243 b) flow speed at 1 m/s, with total residuals calculated at 0.0243 b) flow speed at 1 m/s, with total residuals calculated at 0.0243 b) flow speed at 1 m/s, with total residuals calculated at 0.0243 b) flow speed at 1 m/s, with total residuals calculated at 0.0243 b) flow speed at 1 m/s, with total residuals calculated at 0.0243 b) flow speed at 1 m/s, with total residuals calculated at 0.0243 b) flow speed at 1 m/s, with total residuals calculated at 0.0243 b) flow speed at 1 m/s flow speed at 0.0178

but this was shown to be less effective in early simulations. Based on the results in Fig. 5.9, it appears that being connected to a longer section of subdermal canal has a greater effect on allowing the sensor to extract information properly from the surroundings. It also appears that the neuromast needs to be close to the canal for its benefits to be properly felt. A possible further design to experiment with would be a long canal section that was also widely spaced from the neuromast, so as to explore the effect that separation between the canal and the neuromast has on signal integrity.

5.3.5 Sensor operational envelope

Additional simulations were run to test the effectiveness of the sensor at the high end and low end of the flow speeds that a robot might expect to experience, namely at 0.1m/s and 1m/s. This builds on the work in the previous chapter, where simulations were used to establish and qualitatively characterise the Kármán vortex streets at these speeds.

The associated total residuals for each of the two speeds are 0.0243 and 0.0178, for 0.1m/s and 1m/s respectively. The result for our upper bound of 1m/s marks only a slight increase in total residuals over our standard speed of 0.5m/s. This is a positive result as it shows that the sensor is still effective for a faster underwater vehicle. The upper bound at which a 10cm diameter cylinder in water can be expected to produce a Kármán vortex street is at 3m/s (determined in section 4.5), so while it is difficult to say with certainty how the sensor will behave as velocities increase up to this, the minimal increase between 0.5 and 1m/s suggests that further increases in velocity could result in minimal changes again. More concerning is the quite significant increase in residuals that is seen as velocity decreases. However, looking closely at Fig. 5.10(a), it seems

that the main source of this increase actually occurs due to a phase shift. At around 300 seconds, it is particularly evident that the two signals are 180 degrees out of phase. Shifting the phase accordingly gives a new error of 0.0143, which is now better than our standard speed, and implies that the sensor will remain effective as velocities decrease, potentially even improving further. The shift in phase in an interesting result: it seems that for velocities above 0.5m/s, vortices that are shed from the same side as the sensor result in an increase in velocity for the neuromast, while vortices shed from the other side of the cylinder result in a decrease in velocity, the same as is the case when no sensor is present. For velocities below 0.1m/s, the opposite is true. At higher velocities, it seems that the primary mechanism is as a result of frictional forces within the water acting to drag the water within the sensor forward to cause the velocity increase, whereas at lower velocities, pressure differentials become the primary source of flow accelerations. It is also likely that as the energy within the flow decreases, the sensor itself acts to disrupt the flow more. Further exploration of the mechanisms at low velocities is needed to be certain.

As further exploration of the sensor design, additional sensors were created with differing diameters. In the previous chapter it was noted that the pore size has an effect on the sensitivity, allowing detection of low velocity flow features among a constant background flow, and so further simulations were run using the same design as the optimised sensor but with an increased and decreased channel radius; 20mm and 10mm respectively. It was theorised that at lower velocities, a larger channel would allow the sensor to be more sensitive to the slower flow velocities, i.e. there would be less error due to a larger area through which information can be transmitted making it more likely that flow within the sensor matches flow outside it. At high velocities however, the larger volume of water in the sensor becomes more susceptible to noise in the higher energy system. A narrow channel is predicted to show the opposite, being less susceptible to noise in the higher velocity, higher energy set-up, but then being less able to properly extract information at lower velocities. This prediction is in line with the narrow canal systems seen in riverine fish that experience fast flowing water and the expanded canals in still or deep water fish who typically experience much slower flows, if any [123, 125]

It is first of all interesting to note that there are no cases where either larger or smaller diameter sensor display better signal similarity. This seems to indicate that a 15mm canal offers an optimal balance between reducing noise and increasing sensitivity. In the 1m/s velocity flow, it seems to be the case that the narrow channel is more similar to the expected result than the wide channel (5.11(e)), as predicted; this is most evident towards the end of the series. At 0.5m/s, however, both canals result in noisy detected signals, with the narrow canal faring slightly better and at 0.1m/s, the two canals have very similar errors, again apparently noisy. As seen in the previous set of results, there are periods here in a number of the results where the detected and expected signal are 180 degrees out of phase, particularly clear in Fig. 5.11(a) and (f). Shifting these, along with Fig. 5.11(b) and (d), errors are now seen to be 0.0188 for the narrow design at 0.1m/s and 0.0193, 0.0185, and 0.0207 for the wide design at 0.1, 0.5 and 1m/s respectively. This

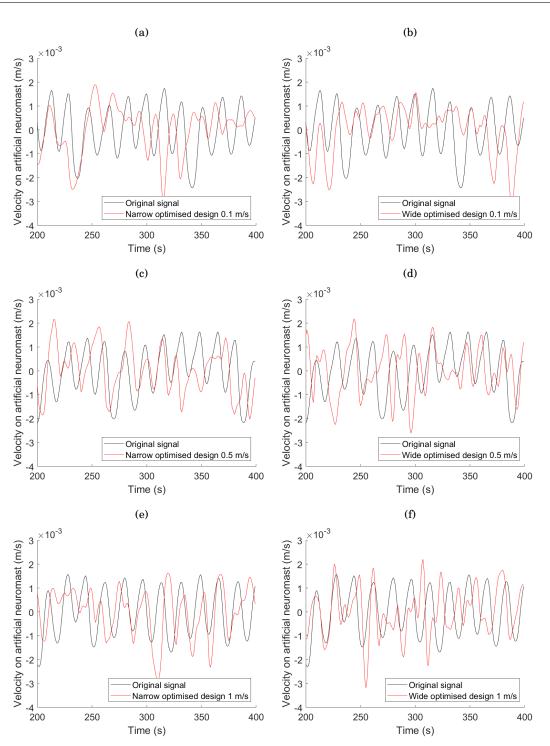


Figure 5.11: Comparisons between normalised time-series detected by the optimised sensor design (red) and the original waveform expected (black) in simulation. a) channel diameter at 10mm and at 0.1m/s, total residuals = 0.0210 b) channel diameter at 20mm and 0.1m/s, total residuals = 0.0206 (c) channel diameter at 10mm, total residuals = 0.0193. (d) channel diameter at 20mm, total residuals = 0.0213 (e) channel diameter at 10mm and at 1m/s, total residuals = 0.0189 (f) channel diameter a 20mm and at 1m/s, total residuals = 0.0191.

marks a reduction in residual error for all cases except the 20mm canal at 1m/s. If we maintain the assumption above that the out of phase response is as a result of pressure differentials while the in phase response is due to flow velocity and associated frictional forces, we can note that counter to our hypothesis, the narrow canal is better at low velocity likely due again to the smaller volume of water that need move to illicit a neuromast response. The wide canal appears to be less effective at low velocity due to the same reasoning, as at lower background flow velocity, the detected signal amplitude is markedly less than for the narrow canal. As flow velocities increase, for the narrow canal there seems to be a definite switch between pressure differential and friction forces as the driving mechanism, while the wider canal seems to be subject to both, leading to the increased noise in the detected signal. As such, half of our hypothesis can be considered to be true, namely that the narrow canal does offer better noise reduction than the wider canal, but not better than the 15mm canal. It is not the case that the wider canal offers better sensitivity at lower flow velocities.

5.4 Artificial lateral line production and testing

Our optimised sensor (Fig. 5.12) was 3D printed using a Form 2 printer and Clear V4 resin. A 7 x 7mm window was cut into the short side of the sensor to add the artificial neuromast. Our neuromast consists of an unpowered LED with a layer of cloth adhesive-tape attached between the pins to increase the surface area affected by the flows. The LED bulb was coloured with black to increase contrast, and is henceforth referred to as the visual tracker. A 10 x 10mm square of elastic material was used to cover the window, and the pins of the LED were pushed through this, so that the visual tracker remains outside the sensor; the fabric was added after this stage. The taped pins of the LED are exposed to the flow within the sensor and deflect in response to changing velocities. The 10 x 10mm elastic square represents the highly elastic membrane discussed in section 5.2.1 and acts as a fulcrum, allowing the neuromast hair to swing freely. The movement of the visual tracker indicates deflections of the pins inside the sensor as a response to shed vortices. A camera is used to record the motion of the visual tracker to produce the sensory output. Several of the design decisions discussed here were due to the Covid-19 pandemic limiting access to certain resources.

Given more time, the sensor would have been redesigned to output an electronic signal instead of requiring the camera and subsequent video analysis. Considering that the sensor is meant to be for swarms, keeping the design as simple and inexpensive as possible is still the major driving force. Preliminary thoughts on ways to improve the design involve adding an enclosed housing, with one of the internal faces bearing printed strips of wiring. The visual tracker element of the artificial neuromast would then be replaced by a thin, elastic hair of conductive metal. As the fluid moves the part of the artificial neuromast in flow, the conductive hair also moves and is pressed against the bands of wiring. The hair will span the gap between the bands of wiring, thus



Figure 5.12: 3D printed physical sensor, with the elastic skin (red), artificial neuromast, and corresponding visual tracker (black).

changing the length of the circuit, and as a result the resistance, which can then be measured. Increased fluid flow will result in increased force which will cause the hair to deflect more and bridge the gap between more of the bands, resulting in a greater change in resistance. In this way, analogue signals of changes in flow velocity can be captured, meaning the relative strength of the passing vortices can be captured. As the force from the fluid stops, the conductive hair will move away from the bands of wiring, and due to its elastic nature will return to its original straight shape. Here, we see a major benefit of using an elastic membrane as a fulcrum, as it keeps the fluid away from the conductive hair and bands of wiring where it would interfere significantly. An alternative, albeit more expensive, design would use a thin magnetic element for the haircell which would then move between an off-the-shelf hall-effect sensor, which could measure deflection. Preliminary CAD models of these designs are available in Appendix D.

Preliminary experiments were undertaken to demonstrate the physical sensor's ability to filter the laminar background flow and to detect shed vortices. To demonstrate the former, the sensor was moved through a static container of water at a steady speed, in approximation of having a steady laminar flow being passed around the sensor. This was done to demonstrate that the laminar flow, typically background flow, would be filtered out and not result in immediate saturation of our neuromast; saturation occurs when the visual tracker reaches its position of maximum deflection. This is undesirable as after this point no additional information can be extracted from the surroundings, such as from turbulent flows. To demonstrate the latter, the sensor was held stationary in a large container of water and a cylinder measuring 100 mm in

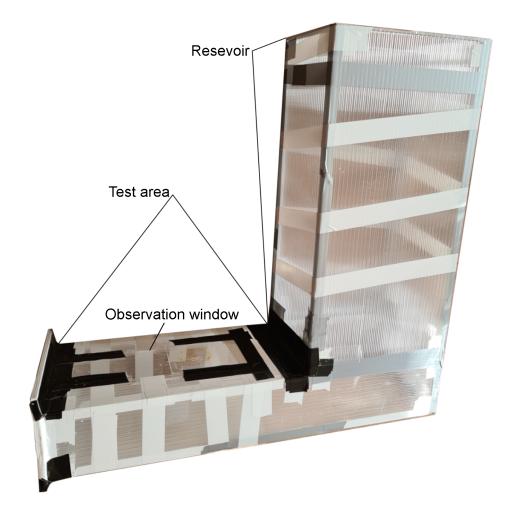


Figure 5.13: The custom built tank used for the sensor flow experiments. Tank walls were made of twin-wall polycarbonate sheeting, that was attached together using duct tape and silicone sealant. A thick plastic board with holes drilled in was used to cover the exit. These holes were covered to allow the resevoir to fill and then uncovered to allow water to flow through the test area. This set-up was used in a home environment during the Covid-19 pandemic.

diameter was pulled through the water alongside the sensor. Speeds and distances were varied to test the conditions over which the sensor was able to function without information saturation and to detect a vortex. Each pass was recorded. Any motion of the visual tracker was tracked as a way of indicating that the sensor had been successful.

Further experiments were also conducted in a custom built flow tank, consisting of a test area and a water reservoir. The reservoir was filled using an external water source, before being allowed to flow through the test area. A 100mm diameter plastic cylinder was placed into the centre of the test area to generate the necessary vortices. Windows were cut into the top surface of the test area to allow the sensor to be positioned in different locations behind the cylinder. A camera was positioned 150 mm away from the top of the arena and set to record in 1080p at

30fps. Footage was analysed frame by frame in the image processing software GIMP (version 2.10.18), where each video was given a global coordinate system centred on the bottom of the sensor opening, and movement of a fixed point on the visual tracker was recorded against this system; the fixed point varied between videos so all graphs were adjusted to be centred around 0.

5.4.1 Experimental results

A prototype of the sensor was demonstrated in a static container of water. Fig. 5.14 shows the sensor moving through the water, using a ruler to highlight the distance covered, without displaying a signal on the neuromast. This result is as expected, as our rear-facing pores act to filter out the background flow or in this case, filter out the inertial effect of the static water. This experiment is meant to act as a control case for the following two experiments, but some limitations exist to this as the set-ups are not entirely the same. However, in fluid dynamics, flow cases with static object and moving fluid, and vice versa, are often substituted for one another, and as such we deem this suitable as a control at the proof of concept stage.

Fig. 5.15 shows the sensor immobile with the cylinder moving through the container and generating a vortex as it passes; this is seen by the recorded oscillation. Fig. 5.15(c) shows the most deflection; it is also possible to see the vortex forming close to the mouth of the sensor in the ripples of the water. This panel is most similar to the setup used in the simulation, so the correlating results lend support to one another.

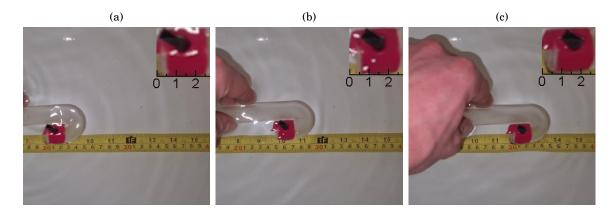


Figure 5.14: 3 still images taken from a video of the sensor being moved in static water to demonstrate the filtering effect of the sensor. Time progresses from the initial frame of the video (a) to the final frame of the video (c). A ruler is included in the background to better illustrate the motion of the sensor. The final position of the visual tracker is 8mm further forward than the starting position, but this can be attributed to parallax, because firstly, the tracker moves forward into the flow which it would not do if it was being affected by the sensor movement, and secondly, it does not return its (neutral) starting position, which it would do if the motion was being caused by negative pressure at the mouth of the sensor. Additionally, the apparent distance between the top and bottom edges of the mouth of the sensor go from 0mm to 4mm.

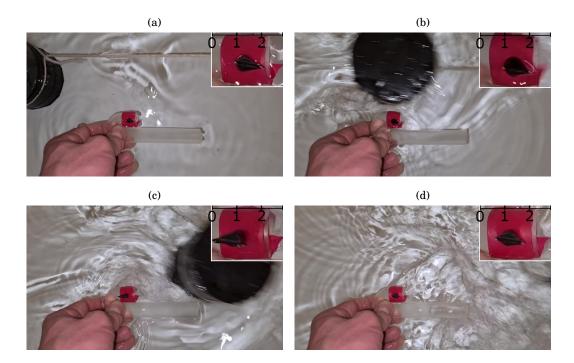


Figure 5.15: 4 still images taken from a video demonstrating the sensor's ability to detect passing vortices. Time progresses from (a) to (d). Each still image has a zoomed in call out showing the deflection of the neuromast at that time. As the cylinder passes in (c), there is a deflection of 1cm (from 1 to 0 on the markings above), before the tracker returns to 1 again in (d).

Fig. 5.17 shows the results of the sensor when tested within the flow tank. The sensor was placed at 6 different locations and the displacement of the visual tracker was measured during each run. 3 trials were done at each location to increase validity of results and these are shown in the different lines on the graphs at each location. It can be seen that the sensor shows deflection in response to the formation and shedding of vortices in all of the sampled areas. We see the best consistency between trials in the centre of the row closer to the cylinder, which is the position that the simulations have predicted to be the best spot for the sensor to operate in. We also see the least deflection in the first row at the furthest y position (X1Y3) from the cylinder, which is also predicted by simulation, due to the vortex forming in the region behind the cylinder and then being shed downstream from there. X1Y3 is further from the vortex than the other positions, hence the reduced deflection. An interesting result to note is the difference in time when the deflection occurs that can be seen in multiple positions. This is most likely to be as a result of the vortex forming and being shed from different sides of the cylinder in different trials. This is corroborated by the fact that the later deflections tend to be reduced. The vortices shed on the far side of the cylinder are further from the sensor and so must travel further before they can be detected, explaining the slight delay and indicating that the earlier troughs are likely from vortices shed on the sensor side of the cylinder, while the later troughs are from the opposite side. It is also possible that the body of the sensor is interfering, as some of it does sit in the path of

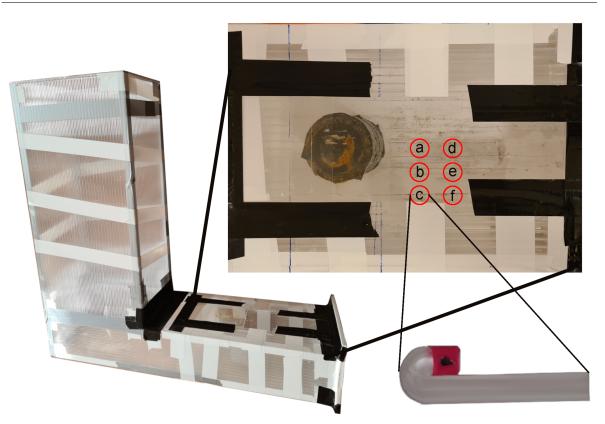


Figure 5.16: Breakdown of the experimental set-up used in the custom flow tank that was used to test for the ability of the sensor to detect shed vortices. Vortices are shed upstream by the black cylinder (Approximately 10cm diameter) Red circles mark the locations at which the sensor was positioned. Flow moves from left to right.

the shed vortices and this could also cause both a delay and a reduced deflection.

Using an average of the deflections taken over the 3 trials (Fig. 5.18) reveals that the two positions predicted by the simulations have the greatest deflection, with the position in the upstream row having the larger of the two. The double troughs mentioned above are also very apparent, particularly for the X2Y0 position (in line with the cylinder centre, in the downstream row). Referring back to Fig. 5.17, it is evident that the shape is as a result of the averaging, and that the second troughs still have reduced deflection, maintaining the theory that the difference is due to which side the vortex forms on.

It is worth noting that the greatest deflection actually occurs at the X2Y0 position. When in simulation, we based our positioning choice around the point at which maximum variation occurs, following the theory that we would be able to extract maximum information from here. However, at any one moment within both the simulation and in the experiment, the point where maximum deflection will occur may not be in this same position, and will likely vary slightly in both x and y directions. Additionally, experimental conditions are harder to both measure and control precisely, and differences in initial conditions will result in differences in results.

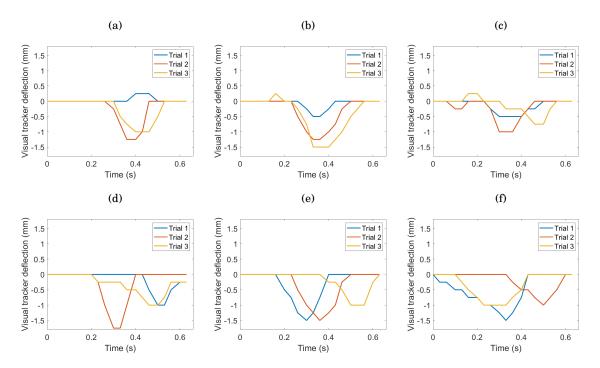


Figure 5.17: Results from the video analysis of the sensor response. Letter labels in this diagram correspond to the letter labelled positions seen in Fig. 5.16, such that results from the sensor being in position (a) correspond to the graph here labelled (a), etc. Each graph shows the response of the visual tracker to a passing vortex over 3 separate trials.

Overall, however, these are promising initial results that indicate that the sensor is able to detect shed vortices in flow, and over a wider area than initially thought.

5.5 Conclusion

Our new optimised artificial line sensor design (Fig. 5.12(a)) has been shown to be effective at detecting vortices shed by potential obstacles or upstream robots. We also explain and evidence our rationale behind the design choices, all of which can be rooted in biology, with a series of simulations where the particular traits we want to emphasise are removed to demonstrate an associated decrease in performance. In every case, we see significant increases in residuals and loss of similarity in signal shape. To validate simulated results in reality, we produce and test the proposed sensor and show that it is able to filter water flow caused by the sensor motion in water, and sense vortices shed by both a passing cylinder in static water and vortices shed behind a cylinder in flow. This work offers a promising new avenue of pressure sensor design that is both inexpensive and simple to manufacture that could be easily integrated onto pre-existing underwater robotic platform used to inspect underwater structures, explore canals, or perform environmental monitoring. It also offers the potential for an artificial lateral line system that is effective using only a single sensor, which could result in significant reductions in complexity and

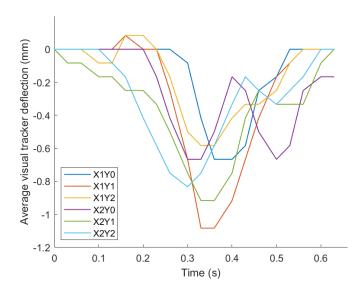


Figure 5.18: The average of the deflection across the three trials

expense. Such a reduction could be exploited for swarming, to create large numbers of simple and inexpensive robots that use this artificial lateral line system to navigate and interact with each other, and in turn display complex emergent behaviours. We have already began to work towards this goal on both software and hardware fronts through a number of student projects. A neural network has been developed and trained to read the flow fields behind a cylinder in simulation, and from this it has been shown that a simple agent based model can navigate said flow field to a given location by sampling only a single point per unit time. This is now being further developed into a multi agent model. A simple bio-inspired robotic fish with a compliant caudal fin has also been designed to host our optimised artificial lateral line sensor, that once complete will mark the beginnings of the development of the large scale swarm just mentioned.



CONCLUSIONS

FT ere we summarise the work that has been done, walking through the biological experiments, through the simulations and on to the experimental tests of the flow sensor before looking forward to further potential work.

6.1 **Biological experiments**

Our early work was focused around generating a large new data set containing information about the lateral line morphology and collective behaviour, all with the hopes of being able to find new relationships tying these two together. To do this, an experiment was conceived in which purpose bred cichlid hybrids were first observed in a custom built flow tank, before being stained with a neuromast illuminating vital dye called DASPEI and photographed, and finally being CT scanned and having their lateral line structure analysed through the use of morphometrics.

6.1.1 Flow tank and shoaling

We used a purpose bred second generation hybrid of two cichlid species (*Aulonocara stuartgranti* X *Otopharynx lithobates*) to explore differences in collective behaviour. These parents were chosen as they represent extremes of lateral line morphology, with the Aulonocara possessing a highly developed 'widened' lateral line morphology and the Otopharynx possessing a 'narrow' morphology; the F2 offspring were expected to show large amounts of variation between the two. This was characterised through the use of raincloud plots which showed that in almost all cases the offspring showed traits that did indeed range between the two parents.

6.1.2 DASPEI staining and photography

We used an off-the-shelf solution here to image neuromasts, coupling the vital dye DASPEI with the NIGHTSEA fluorescence imaging kit. A Canon DSLR was used through a microscope to capture images of the neuromasts in the head, along the trunk, in the tail, and also on the underside of the jaw.

6.1.3 CT scanning and morphometrics

All individuals used in the behaviour trials were subsequently prepared and scanned using a Nikon XTH225ST micro-Computed Tomography (microCT) system. Fish were prepared for scanning using florist foam and scanned two at a time inside plastic jars, each scan using 3141 projections and a voxel size of 20-30µm. Parameters for morphometrics were determined by comparison of our specimens against scans of other similar specimens and inspection of reconstructed images. Morphometrics and analysis of results were performed by a collaborator, which involved identifying and digitising landmarks on the 2D images generated from the scans to allow for the comparison of features, such as the pores, between individuals.

6.2 Modelling relationships

R (version 3.6.1) was used to build generalised mixed linear models (GLMMs) that analysed the relationships between our morphological variables: neuromast number and location and pore sizes, and our behavioural variables: nearest neighbour distance and shoal radius. From this, we were able to identify a few interesting trends that were persistent across a range of conditions. Firstly, a higher number of canal neuromasts on the head leads to our target fish swimming more closely to its neighbours, in both laminar and turbulent flow; this trend continues when we choose to focus on only upstream neighbours and on on those neighbours that are upstream and directly in front so as to be within the field of flow detection. This trend was also observed to be persistent when controlling for body size. Secondly, that a higher number of superficial neuromasts on the head leads to looser shoal formations; also persistent when controlling for body size. Finally, that increased pore size of canals in the head also leads to a reduction in distance to neighbours when considering all neighbours, upstream only neighbours, and neighbours within the aforementioned field of flow detection. Collectively, this suggests a previously unseen emphasis of the head lateral line systems in mediating shoaling behaviour, as well as suggesting that the finer sensitivity to turbulence that larger pores and increased canal neuromasts offer means that canal lateral line systems are more responsible for the fine tune distance control, while the general flow velocity information obtained from the superficial neuromasts is better suited for general positioning and avoiding other individuals.

6.3 Designing an artificial lateral line

Using the conclusions drawn from the biological work, we investigate the filtering properties of the canal structure and the effect that varying pore size has on sensitivity through use of a single unit of canal lateral line, consisting of a box representing the canal, two holes in one surface to represent pores, and a pin inside the box that could react to changes in flow velocity. Simulation results revealed that our design resulted in a significant drop in average speed between the freestream flow signal and the detected signal, effectively showing that the design can remove the background flow velocity and allow for the detection of turbulent vortices instead. They also revealed that increasing pore sizes tends to lead to a greater mean velocity acting on the hair cell. As we have demonstrated the ability of the sensor to filter background flow, these increases can be attributed to an increased sensitivity to turbulence. It is worth noting that residual errors between the detected signal and the expected signal were high with this set-up.

6.4 Optimising the sensor

Key issues were identified with the original prototype, and changes were hypothesised to fix them. A new sensor design was created as a result, and the importance of the design changes were highlighted through the creation and comparison of similar models that were each missing one of the elements. The design elements identified were the use of circular pipe channels, having pores that face completely away from the direction of flow, and ensuring that there is increased separation between the two pores. Through these changes, we saw significant improvements in similarity between the expected signal and the detected signal; comparing residual errors between the two designs shows the new design has a 25% reduction: 0.0155 compared to 0.0207 for the old design with equivalent pore size (15 mm).

We also tested the operational envelope of the sensor to attempt to verify its suitability for use under other flow conditions, and we able to demonstrate that it can operate effectively over a range of flow speeds.

This new optimised sensor was also tested experimentally in static water and in another custom built flow tank. The first experiment consisted of the sensor being moved at a constant velocity through static water yet registering no deflection on the neuromast, demonstrating an ability to filter out the background flow. The second experiment, again in static water, had the sensor fixed in position, and used a cylinder being pulled past the sensor to generate a vortex. The sensor registered a deflection just after the cylinder had passed, indicating that the generated vortex had been detected. Our final experiments had both cylinder and sensor fixed in position within a custom flow tank. A reservoir was filled and then allowed to flow through the test area and sensor deflections were recorded. The sensor was tested at six different positions within the tank, and was shown to be able to detect the shed vortices in each, but with stronger detections in the places predicted by simulation.

6.5 Future work

Moving forwards with this project, there are several potential areas to explore: further sensor refinement, the development of bio-mimetic control algorithms that use only flow information to shoal, and the integration of the current optimised sensor into an underwater robotic platform. Extra work could also be undertaken to better clarify some of the existing results, such as the apparent association between the number of visible anterior canal neuromasts and body size and the simultaneous association between the number of visible neuromasts and reduced nearest neighbour distance, or to test the effect of darkness on the collective behaviour of these hybrids to further isolate the role of the lateral line.

To clarify the results regarding the decrease of neuromasts with increasing size, more in depth morphological study would be needed on a new batch of hybrids to measure skin thickness of all individuals involved, as well as repeated DASPEI staining to monitor how the number of visible neuromasts changes over time. An association between increasing skin thickness and decreasing visible neuromasts could help to address the loss of anterior canal neuromasts at greater size. Further tests on the effect of increasing body size on sensitivity to hydrodynamic stimuli in the dark for individuals over their lifetime could help to identify if increasing skin thickness results in a decreased sensitivity to these stimuli in the absence of visual cues.

Running the same set of behavioural experiments with these hybrids in the dark could again exploit the range of lateral line characteristics that we saw, but take it a step further by removing visual cues to better isolate the role of the lateral line in collective behaviours.

To further refine the sensor, the best route to take seems to be to use AI and machine learning on a high powered computational cluster. Further refinement would require the development and testing of a large number of new models, each marginally different from the others, something that would take a lot of time and effort to do by hand. Automating this process would allow incremental changes to be made to aspects of the design and flow conditions to see if a better solution can be reached. Using a high powered processor is not strictly necessary, but would greatly speed up the process. Some of this work has been started by a student in a Summer Internship role.

Developing control algorithms that show behaviour similar to what has been observed in experiment and can be used to control a swarm of underwater vehicles would be another interesting direction to take this project. Agent-based modelling using the flow data generated when simulating a cylinder in flow offers the chance to build algorithms that not only have a practical use in helping large numbers of underwater robots to organise themselves, but also potentially explaining new elements of fish behaviour by building governing equations in fish shoals. Some of this work is currently being touched on by an MSc student collaborator.

Finally, exploring ways to integrate this sensor on to one or more fish-like robots, and then demonstrating that these robots are able to interact and coordinate using only the sensor, would bring the project full circle from the source of inspiration in the natural world to being fully realised in a robotic counterpart. This area of the project is also beginning to be explored by an MSc student collaborator.

Naturally, the final end goal, one that was talked about at the beginning of the project but deemed infeasible for the time scale, would be to integrate all of the work shown in this thesis with the three elements of further work above to create a simple, bio-inspired, shoal of fish-mimetic robots that use fish-behaviour derived, flow based control algorithms to navigate by using the, potentially more, optimised bio-inspired flow sensor developed here. Such a swarm has a great many potential uses ranging from environmental monitoring, to wildlife videography, to search and rescue, all while being easy to manufacture, low power and low cost.



APPENDIX A

his appendix contains the graphs detailing the relationships between each of the morphological variables we used and body size.

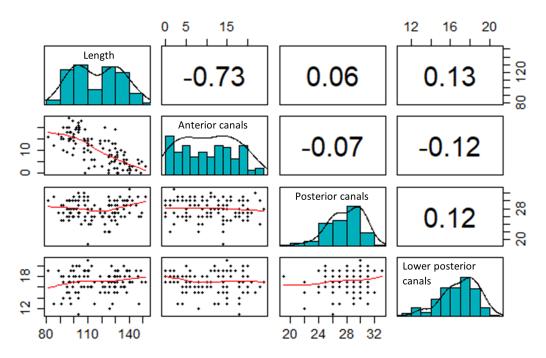


Figure A.1: The associations between body length and the different canal neuromast morphological variables: the number of anterior canal neuromasts, the number of posterior canal neuromasts and the number of lower posterior canal neuromasts (below/left of variable histogram), and the associated Spearman's rank correlation coefficient (above/right of variable histogram).

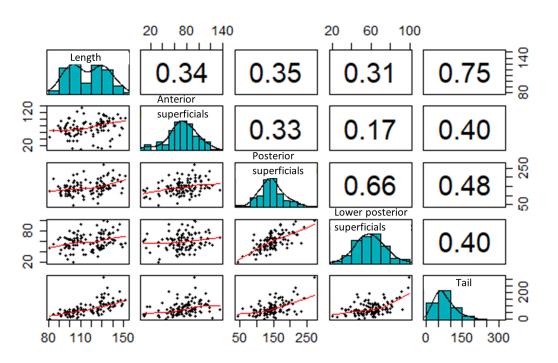


Figure A.2: The associations between body length and the different superficial neuromast morphological variables : the number of anterior superficial neuromasts, the number posterior superficial neuromasts, the number of lower posterior superficial neuromasts and the number of tail neuromasts (below/left of variable histogram), and the associated Spearman's rank correlation coefficient (above/right) of variable histogram).

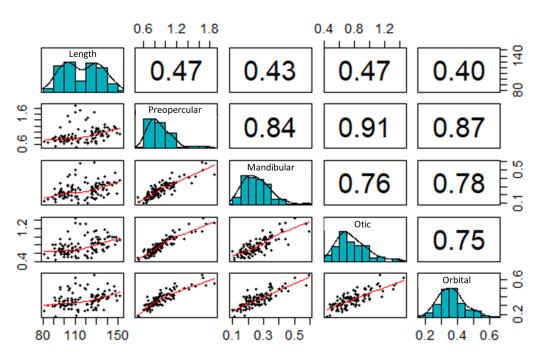


Figure A.3: The associations between body length and the different canal pore size variables: the mean size of preopercular canal pores, the mean size of mandibular canal pores, the mean size of otic canal pores, and mean size of orbital canal pores (below/left of variable histogram), and the associated Spearman's rank correlation coefficient (above/right of variable histogram).



APPENDIX B

his appendix contains the tables comparing the Generalised Linear Mixed Models that we generated to associate our morphological variables with our behavioural variables. Table B.1: Model comparisons using the Akaike Information Criterion scores for neuromast models that explain variability in mean nearest neighbour distance, for the dataset that includes all individuals (hybrids and parent species), where total body length is included as a covariate term in all models.

Model Name	df	dAICc	Association	LRT
scale(Anterior.Canals.Neuromasts)*Turbulent/Laminar	8	0	-ve	0.0448
+scale(Length)+Trial.Order+(1 ID)				
scale(Head.Canal.Neuromasts)+Turbulent/Laminar	7	0.4	-ve	0.0331
+scale(Length)+Trial.Order+(1 ID)				
scale(Head.Superficial.Neuromasts)+Turbulent/Laminar	7	5.3	+ve	0.0116
+scale(Length)+Trial.Order+(1 ID)				
Null	6	5.8	N/A	0
scale(Anterior.Superficial.Neuromasts)*Turbulent/Laminar	8	6.1	+ve	0.0176
+scale(Length)+Trial.Order+(1 ID)	0			
scale(Posterior.Superficial.Neuromasts)+Turbulent/Laminar	7	7.3	+ve	0.0031
+scale(Length)+Trial.Order+(1 ID)] '			
scale(Lower.Posterior.Canal.Neuromasts)+Turbulent/Laminar	7	7.4	+ve	0.0027
+scale(Length)+Trial.Order+(1 ID)				
scale(Lower.Posterior.Superficial.Neuromasts)+Turbulent/Laminar	7	7.5	+ve	0.0021
+scale(Length)+Trial.Order+(1 ID)				
scale(Posterior.Canal.Neuromasts)+Turbulent/Laminar	7	7.9	-ve	0.0004
+scale(Length)+Trial.Order+(1 ID)		1.0		0.0004
scale(Tail.Neuromasts)+Turbulent/Laminar	7	7.9	-ve	0.0002
+scale(Length)+Trial.Order+(1 ID)				
scale(Lower.Posterior.Canal.Neuromasts)*Turbulent/Laminar	8	9.4	-ve	0.0034
+scale(Length)+Trial.Order+(1 ID)	Ŭ			
scale(Posterior.Superficial.Neuromasts)*Turbulent/Laminar	8	9.4	-ve	0.0031
+scale(Length)+Trial.Order+(1 ID)				
scale(Lower.Posterior.Superficial.Neuromasts)*Turbulent/Laminar	8	9.4	-ve	0.0031
+scale(Length)+Trial.Order+(1 ID)				
scale(Posterior.Canal.Neuromasts)*Turbulent/Laminar	8	9.8	-ve	0.0016
+scale(Length)+Trial.Order+(1 ID)				
Scale(Tail.Neuromasts)*Turbulent/Laminar	8	10	+ve	0.0004
+scale(Length)+Trial.Order+(1 ID)				

Table B.2: Model comparisons using the Akaike Information Criterion scores for neuromast models that explain variability in mean nearest neighbour distance, for the dataset that includes only hybrids, where total body length is included as a covariate term in all models.

Model Name	df	dAICc	Association	LRT
scale(Anterior_Canal_Neuromasts)+Turbulent/Laminar	7	0	-ve	0.0255
+scale(Length)+Trial.Order+(1 ID)	'			
scale(Posterior_Superficial_Neuromasts)+Turbulent/Laminar	7	1.2	+ve	0.019
+scale(Length)+Trial_Order+(1 ID)	\ [']			
scale(Anterior_Canal_Neuromasts)*Turbulent/Laminar	8	1.4	-ve	0.0296
+scale(Length)+Trial_Order+(1 ID)				
scale(Posterior_Superficial_Neuromasts)*Turbulent/Laminar	8	2	-ve	0.0265
+scale(Length)+Trial_Order+(1 ID)	Ŭ			
Null	6	2.7	N/A	0
scale(Lower_Posterior_Superficial_Neuromasts)+Turbulent/Laminar	7	4.4	+ve	0.0023
+scale(Length)+Trial.Order+(1 ID)	Ľ			
scale(Anterior_Superficial_Neuromasts)+Turbulent/Laminar	7	4.6	+ve	0.0012
+scale(Length)+Trial_Order+(1 ID)				
scale(Tail_Neuromasts)+Turbulent/Laminar	7	4.8	-ve	0.0003
+scale(Length)+Trial_Order+(1 ID)	<u> </u>			
scale(Lower_Posterior_Canal_Neuromasts)+Turbulent/Laminar	7	4.8	+ve	0.0001
+scale(Length)+Trial_Order+(1 ID)				
scale(Posterior_Canal_Neuromasts)+Turbulent/Laminar	7	4.8	+ve	1.00E-05
+scale(Length)+Trial_Order+(1 ID)	ľ			
scale(Lower_Posterior_Superficial_Neuromasts)*Turbulent/Laminar	8	6	-ve	0.0053
+scale(Length)+Trial_Order+(1 ID)				
scale(Lower_Posterior_Canal_Neuromasts)*Turbulent/Laminar	8	6.7	-ve	0.0015
+scale(Length)+Trial_Order+(1 ID)				
scale(Posterior_Superficial_Neuromasts)*Turbulent/Laminar	8	6.8	+ve	0.0013
+scale(Length)+Trial_Order+(1 ID)				
scale(Posterior_Canal_Neuromasts)*Turbulent/Laminar	8	6.8	-ve	0.0011
+scale(Length)+Trial_Order+(1 ID)				
scale(Tail_Neuromasts)*Turbulent/Laminar	8	6.9	-ve	0.0005
+scale(Length)+Trial_Order+(1 ID)	0			

Table B.3: Model comparisons using the Akaike Information Criterion scores for neuromast models that explain variability in mean group radius, for the dataset that includes all individuals (hybrids and parent species), where total body length is included as a covariate term in all models.

Model Name	df	dAlCc	Association	LRT
scale(Anterior_Superficial_Neuromasts)+Turbulent/Laminar	7	0	+ve	0.0531
+scale(Length)+Trial_Order+(1 ID)	'	0	7 + VC	0.0001
scale(Anterior_Superficial_Neuromasts)*Turbulent/Laminar	8	10	+ve	0.0537
+scale(Length)+Trial_Order+(1 ID)	Ŭ	1.5	140	0.0007
scale(Anterior_Canal_Neuromasts)*Turbulent/Laminar	8	18	-ve	0.0412
+scale(Length)+Trial_Order+(1 ID)		4.0	-vc	0.0412
scale(Anterior_Canal_Neuromasts)+Turbulent/Laminar	7	5.8	-ve	0.0286
+scale(Length)+Trial_Order+(1 ID)	Ĺ	0.0	10	0.0200
scale(Posterior_Superficial_Neuromasts)+Turbulent/Laminar	7	6.8	+ve	0.024
+scale(Length)+Trial_Order+(1 ID)		0.0	TVC .	0.024
scale(Posterior_Superficial_Neuromasts)*Turbulent/Laminar	- 8	85	-ve	0.0255
+scale(Length)+Trial_Order+(1 ID)	Ŭ	0.0	-10	
Null	6	10.3	N/A	0
scale(Lower_Posterior_Superficial_Neuromasts)+Turbulent/Laminar	7	10.9	+ve	0.0063
+scale(Length)+Trial_Order+(1 ID)	Ĺ	10.0		
scale(Posterior_Canal_Neuromasts)+Turbulent/Laminar	7	12 1	-ve	0.0011
+scale(Length)+Trial_Order+(1 ID)		12.1		0.0011
scale(Lower_Posterior_Canal_Neuromasts)+Turbulent/Laminar	7	12.2	4/10	0.0004
+scale(Length)+Trial_Order+(1 ID)	Ĺ	12.2		0.0004
scale(Tail_Neuromasts)+Turbulent/Laminar	7	12.3	+ve	9.00E-05
+scale(Length)+Trial_Order+(1 ID)		12.0		0.002 00
scale(Lower_Posterior_Superficial_Neuromasts)*Turbulent/Laminar	8	12.7	-ve	0.0071
+scale(Length)+Trial_Order+(1 ID)	Ŭ	12.7	-•0	0.0071
scale(Posterior_Canal_Neuromasts)*Turbulent/Laminar	8	13	-ve	0.006
+scale(Length)+Trial_Order+(1 ID)	Ŭ			0.000
scale(Lower_Posterior_Canal_Neuromasts)*Turbulent/Laminar	8	8 14.2	VO	0.0008
+scale(Length)+Trial_Order+(1 ID)	Ŭ		-•0	
scale(Tail_Neuromasts)*Turbulent/Laminar	8	14.2	110	0.0002
+scale(Length)+Trial_Order+(1 ID)	0	14.0	3 +ve	0.0002

Table B.4: Model comparisons using the Akaike Information Criterion scores for neuromast models that explain variability in mean group radius, for the dataset that includes only hybrids, where total body length is included as a covariate term in all models.

Model Name	df	dAICc	Association	LRT
scale(Head_Superficial_Neuromasts)+Turbulent/Laminar +scale(Length)+Trial_Order+(1 ID)	7	0	+ve	0.0406
scale(Head_Superficial_Neuromasts)*Turbulent/Laminar +scale(Length)+Trial_Order+(1 ID)	8	1.5	-ve	0.0433
scale(Trunk_Superficial_Neuromasts)+Turbulent/Laminar +scale(Length)+Trial_Order+(1 ID)	7	2.8	+ve	0.0263
scale(Trunk_Superficial_Neuromasts)*Turbulent/Laminar +scale(Length)+Trial_Order+(1 ID)	8	2.8	-ve	0.0365
scale(Head_Canal_Neuromasts)+Turbulent/Laminar +scale(Length)+Trial_Order+(1 ID)	7	3.4	-ve	0.0229
scale(Head_Canal_Neuromasts)*Turbulent/Laminar +scale(Length)+Trial_Order+(1 ID)	8	4.6	-ve	0.0272
Null	6	5.8	N/A	0
scale(Lower_Trunk_Superficial_Neuromasts)+Turbulent/Laminar +scale(Length)+Trial Order+(1 ID)	7	7.2	+ve	0.0029
scale(Trunk_Canal_Neuromasts)+Turbulent/Laminar +scale(Length)+Trial_Order+(1 ID)	7	7.3	-ve	0.0024
scale(Lower_Trunk_Canal_Neuromasts)+Turbulent/Laminar +scale(Length)+Trial_Order+(1 ID)	7	7.7	-ve	0.0002
scale(Tail_Neuromasts)+Turbulent/Laminar +scale(Length)+Trial_Order+(1 ID)	7	7.7	-ve	0.0002
scale(Trunk_Canal_Neuromasts)*Turbulent/Laminar +scale(Length)+Trial_Order+(1 ID)	8	8.2	-ve	0.0082
scale(Lower_Trunk_Superficial_Neuromasts)*Turbulent/Laminar +scale(Length)+Trial_Order+(1 ID)	8	9.2	-ve	0.0032
scale(Tail_Neuromasts)*Turbulent/Laminar +scale(Length)+Trial_Order+(1 ID)	8	9.6	-ve	0.0007
scale(Lower_Trunk_Canal_Neuromasts)*Turbulent/Laminar +scale(Length)+Trial_Order+(1 ID)	8	9.7	-ve	0.0003

Table B.5: Model comparisons using the Akaike Information Criterion scores for neuromast models that explain variability in mean distance to nearest upstream neighbour, for the dataset that includes all individuals (hybrids and parent species), where total body length is included as a covariate term in all models.

Model Name	df	dAlCc	Association	LRT
scale(Head_Canal_Neuromasts)*Turbulent/Laminar +scale(Length)+Trial Order+(1 ID)	8	0	-ve	0.07
scale(Head Canal Neuromasts)+Turbulent/Laminar				
+scale(Length)+Trial Order+(1 ID)	7	5.8	-ve	0.036
scale(Head Superficial Neuromasts)+Turbulent/Laminar	-	7.0		0.000
+scale(Length)+Trial_Order+(1 ID)	7	7.6	+ve	0.029
scale(Head_Superficial_Neuromasts)*Turbulent/Laminar +scale(Length)+Trial Order+(1 ID)	8	8	+ve	0.036
Null	6	12.1	N/A	0
scale(Trunk_Superficial_Neuromasts)+Turbulent/Laminar +scale(Length)+Trial_Order+(1 ID)	7	12.2	+ve	0.009
scale(Lower_Trunk_Superficial_Neuromasts)+Turbulent/Laminar +scale(Length)+Trial_Order+(1 ID)	7	12.9	+ve	0.006
scale(Lower_Trunk_Canal_Neuromasts)+Turbulent/Laminar +scale(Length)+Trial_Order+(1 ID)	7	13.5	+ve	0.003
scale(Trunk_Superficial_Neuromasts)*Turbulent/Laminar +scale(Length)+Trial_Order+(1 ID)	8	14.1	+ve	0.01
scale(Trunk_Canal_Neuromasts)+Turbulent/Laminar +scale(Length)+Trial_Order+(1 ID)	7	14.2	-ve	2E-04
scale(Tail_Neuromasts)+Turbulent/Laminar +scale(Length)+Trial_Order+(1 ID)	7	14.2	-ve	0
scale(Lower_Trunk_Superficial_Neuromasts)*Turbulent/Laminar +scale(Length)+Trial_Order+(1 ID)	8	15	+ve	0.006
scale(Lower_Trunk_Canal_Neuromasts)*Turbulent/Laminar				
+scale(Length)+Trial Order+(1 ID)	8	15.7	+ve	0.003
scale(Trunk Canal Neuromasts)*Turbulent/Laminar	6	45.0		0.000
+scale(Length)+Trial_Order+(1 ID)	8	15.9	-ve	0.002
scale(Tail_Neuromasts)*Turbulent/Laminar +scale(Length)+Trial_Order+(1 ID)	8	16.2	+ve	6E-04

Table B.6: Model comparisons using the Akaike Information Criterion scores for neuromast models that explain variability in mean distance to nearest upstream neighbour, for the dataset that includes only hybrids, where total body length is included as a covariate term in all models.

Model Name	df	dAlCc	Associations	LRT
scale(Head_Canal_Neuromasts)*Turbulent/Laminar +scale(Length)+Trial_Order+(1 ID)	8	0	-ve	0.0595
scale(Trunk_Superficial_Neuromasts)+Turbulent/Laminar +scale(Length)+Trial_Order+(1 ID)	7	4	+ve	0.0278
scale(Head_Canal_Neuromasts)+Turbulent/Laminar +scale(Length)+Trial_Order+(1 ID)	7	4.5	-ve	0.0254
scale(Trunk_Superficial_Neuromasts)*Turbulent/Laminar +scale(Length)+Trial_Order+(1 ID)	8	5.9	-ve	0.0291
scale(Head_Superficial_Neuromasts)+Turbulent/Laminar +scale(Length)+Trial_Order+(1 ID)	7	6.5	+ve	0.015
Null	6	7.1	N/A	0
scale(Lower_Trunk_Superficial_Neuromasts)+Turbulent/Laminar +scale(Length)+Trial_Order+(1 ID)	7	8.4	+ve	0.0045
scale(Head_Superficial_Neuromasts)*Turbulent/Laminar +scale(Length)+Trial Order+(1 ID)	8	8.6	+ve	0.015
scale(Tail_Neuromasts)+Turbulent/Laminar +scale(Length)+Trial_Order+(1 ID)	7	9.3	-ve	1.00E-05
scale(Trunk_Canal_Neuromasts)+Turbulent/Laminar +scale(Length)+Trial_Order+(1 ID)	7	9.3	+ve	0
scale(Lower_Trunk_Canal_Neuromasts)+Turbulent/Laminar +scale(Length)+Trial_Order+(1 ID)	7	9.3	-ve	0
scale(Lower_Trunk_Superficial_Neuromasts)*Turbulent/Laminar +scale(Length)+Trial_Order+(1 ID)	8	10.4	+ve	0.0059
scale(Lower_Trunk_Canal_Neuromasts)*Turbulent/Laminar +scale(Length)+Trial_Order+(1 ID)	8	11.1	+ve	0.0018
scale(Trunk_Canal_Neuromasts)*Turbulent/Laminar +scale(Length)+Trial_Order+(1 ID)	8	11.3	-ve	0.0008
scale(Tail_Neuromasts)*Turbulent/Laminar +scale(Length)+Trial_Order+(1 ID)	8	11.5	+ve	1.00E-05

Table B.7: Model comparisons using the Akaike Information Criterion scores for neuromast models that explain variability in mean distance to nearest neighbour in 'field of flow detection', for the dataset that includes all individuals (hybrids and parent species), where total body length is included as a covariate term in all models.

Model Name	df	dAICc	Associations	LRT
scale(Head_Canal_Neuromasts)*Turbulent/Laminar	8	0	-ve	0.0503
+scale(Length)+Trial_Order+(1 ID) scale(Head Canal Neuromasts)+Turbulent/Laminar				
+scale(Length)+Trial_Order+(1 ID)	7	1.4	-ve	0.0354
scale(Head_Superficial_Neuromasts)+Turbulent/Laminar	7	27	+ve	0.0296
+scale(Length)+Trial_Order+(1 ID)	. '	2.1	+ve	0.0290
scale(Head_Superficial_Neuromasts)*Turbulent/Laminar	8	28	+ve	0.0385
+scale(Length)+Trial_Order+(1 ID)	Ū			0.0000
scale(Trunk_Superficial_Neuromasts)+Turbulent/Laminar	7	6.5	+ve	0.0131
+scale(Length)+Trial_Order+(1 ID)				
Null	6	7.4	N/A	0
scale(Lower_Trunk_Superficial_Neuromasts)+Turbulent/Laminar	7	7.6	+ve	0.0084
+scale(Length)+Trial_Order+(1 ID)				
scale(Lower_Trunk_Canal_Neuromasts)+Turbulent/Laminar	7	8.4	+ve	0.0049
+scale(Length)+Trial Order+(1 ID)				
scale(Trunk_Superficial_Neuromasts)*Turbulent/Laminar +scale(Length)+Trial_Order+(1 ID)	8	8.6	+ve	0.0134
scale(Trunk Canal Neuromasts)+Turbulent/Laminar				
+scale(Length)+Trial Order+(1 ID)	7	9.4	+ve	0.0004
scale(Tail_Neuromasts)+Turbulent/Laminar	7	0.5	+ve	0
+scale(Length)+Trial_Order+(1 ID)		9.5	+ve	0
scale(Lower_Trunk_Superficial_Neuromasts)*Turbulent/Laminar	8	0.8	+ve	0.0084
+scale(Length)+Trial_Order+(1 ID)	0	5.0	140	0.0004
scale(Lower_Trunk_Canal_Neuromasts)*Turbulent/Laminar	8	10.3	-Ve	0.0062
+scale(Length)+Trial_Order+(1 ID)		10.0	-10	0.0002
scale(Trunk_Canal_Neuromasts)*Turbulent/Laminar	8	11.2	-ve	0.002
+scale(Length)+Trial_Order+(1 ID)		11.2		0.002
scale(Tail_Neuromasts)*Turbulent/Laminar	8	11.3	+ve	0.0016
+scale(Length)+Trial_Order+(1 ID)				5.0010

Table B.8: Model comparisons using the Akaike Information Criterion scores for neuromast models that explain variability in mean distance to nearest neighbour in 'field of flow detection', for the dataset that includes only hybrids, where total body length is included as a covariate term in all models.

Model Name	df	dAlCc	Associations	LRT
scale(Trunk_Superficial_Neuromasts)+Turbulent/Laminar +scale(Length)+Trial_Order+(1 ID)	7	0	+ve	0.0292
scale(Head_Canal_Neuromasts)*Turbulent/Laminar +scale(Length)+Trial_Order+(1 ID)	8	1.5	-ve	0.0328
scale(Head_Canal_Neuromasts)+Turbulent/Laminar +scale(Length)+Trial_Order+(1 ID)	7	1.7	-ve	0.0206
scale(Trunk_Superficial_Neuromasts)*Turbulent/Laminar +scale(Length)+Trial_Order+(1 ID)	8	2	-ve	0.0301
scale(Head_Superficial_Neuromasts)+Turbulent/Laminar +scale(Length)+Trial_Order+(1 ID)	7	3.2	+ve	0.0126
Null	6	3.4	N/A	0
scale(Lower_Trunk_Superficial_Neuromasts)+Turbulent/Laminar +scale(Length)+Trial_Order+(1 ID)	7	4.4	+ve	0.0062
scale(Head_Superficial_Neuromasts)*Turbulent/Laminar +scale(Length)+Trial Order+(1 ID)	8	5.1	+ve	0.0139
scale(Trunk_Canal_Neuromasts)+Turbulent/Laminar +scale(Length)+Trial_Order+(1 ID)	7	5.4	+ve	0.0007
scale(Lower_Trunk_Canal_Neuromasts)+Turbulent/Laminar +scale(Length)+Trial_Order+(1 ID)	7	5.4	+ve	0.0005
scale(Tail_Neuromasts)+Turbulent/Laminar +scale(Length)+Trial_Order+(1 ID)	7	5.5	-ve	0
scale(Lower_Trunk_Superficial_Neuromasts)*Turbulent/Laminar +scale(Length)+Trial_Order+(1 ID)	8	6.3	+ve	0.0078
scale(Tail_Neuromasts)*Turbulent/Laminar +scale(Length)+Trial_Order+(1 ID)	8	7.5	+ve	0.0011
scale(Lower_Trunk_Canal_Neuromasts)*Turbulent/Laminar +scale(Length)+Trial_Order+(1 ID)	8	7.6	-ve	0.0009
scale(Trunk_Canal_Neuromasts)*Turbulent/Laminar +scale(Length)+Trial_Order+(1 ID)	8	7.6	+ve	0.0007

Table B.9: Model comparisons using the Akaike Information Criterion scores for neuromast models that explain variability in mean nearest neighbour distance, for the dataset that all individuals (hybrids and parent species). Total body length is only considered as a stand-alone main effect.

Model Name	df	dAlCc	Association	LRT
Null	5	0	N/A	0
scale(Length)+Turbulent/Laminar +Trial_Order+(1 ID)	6	0.1	-ve	0.0089
scale(Length)*Turbulent/Laminar +Trial_Order+(1 ID)	7	0.5	+ve	0.0162
scale(Head_Superficial_Neuromasts)+Turbulent/Laminar +Trial_Order+(1 ID)	6	0.7	+ve	0.0061
scale(Tail_Neuromasts)+Turbulent/Laminar +Trial_Order+(1 ID)	6	0.9	-ve	0.0054
scale(Head_Canal_Neuromasts)*Turbulent/Laminar +Trial_Order+(1 ID)	7	1.2	-ve	0.0132
scale(Head_Canal_Neuromasts)+Turbulent/Laminar +Trial_Order+(1 ID)	6	1.4	-ve	0.0031
scale(Head_Superficial_Neuromasts)*Turbulent/Laminar +Trial_Order+(1 ID)	7	1.5	+ve	0.0121
scale(Lower_Trunk_Canal_Neuromasts)+Turbulent/Laminar +Trial_Order+(1 ID)	6	1.8	+ve	0.0016
scale(Trunk_Superficial_Neuromasts)+Turbulent/Laminar +Trial_Order+(1 ID)	6	2	+ve	0.0004
scale(Trunk_Canal_Neuromasts)+Turbulent/Laminar +Trial_Order+(1 ID)	6	2	-ve	0.0004
scale(Lower_Trunk_Superficial_Neuromasts)+Turbulent/Laminar +Trial_Order+(1 ID)	6	2.1	+ve	0.0002
scale(Tail_Neuromasts)*Turbulent/Laminar +Trial_Order+(1 ID)	7	3	+ve	0.0056
scale(Lower_Trunk_Canal_Neuromasts)*Turbulent/Laminar +Trial_Order+(1 ID)	7	3.7	-ve	0.0022
scale(Trunk_Canal_Neuromasts)*Turbulent/Laminar +Trial_Order+(1 ID)	7	3.8	-ve	0.0018
scale(Lower_Trunk_Superficial_Neuromasts)*Turbulent/Laminar +Trial_Order+(1 ID)	7	4	-ve	0.0011
scale(Trunk_Superficial_Neuromasts)*Turbulent/Laminar +Trial_Order+(1 ID)	7	4.1	-ve	0.0004

Table B.10: Model comparisons using the Akaike Information Criterion scores for neuromast models that explain variability in mean nearest neighbour distance radius, for the dataset that includes only hybrids. Total body length is only considered as a stand-alone main effect.

Model Name	df	dAlCc	Association	LRT
Null	5	0	N/A	0
scale(Trunk_Superficial_Neuromasts)+Turbulent/Laminar +Trial_Order+(1 ID)	6	0.4	+ve	0.0093
scale(Length)+Turbulent/Laminar +Trial_Order+(1 ID)	6	0.6	-ve	0.0079
scale(Trunk_Superficial_Neuromasts)*Turbulent/Laminar +Trial_Order+(1 ID)	7	1.2	-ve	0.0166
scale(Taill_Neuromasts)+Turbulent/Laminar +Trial_Order+(1 ID)	6	1.2	-ve	0.0051
scale(Length)*Turbulent/Laminar +Trial_Order+(1 ID)	7	1.5	+ve	0.0148
scale(Head_Canal_Neuromasts)+Turbulent/Laminar +Trial_Order+(1 ID)	6	1.9	-ve	0.0013
scale(Lower_Trunk_Superficial_Neuromasts)+Turbulent/Laminar +Trial_Order+(1 ID)	6	2.1	+ve	0.0002
scale(Head_Superficial_Neuromasts)+Turbulent/Laminar +Trial_Order+(1 ID)	6	2.1	+ve	6.00E-05
scale(Trunk_Canal_Neuromasts)+Turbulent/Laminar +Trial_Order+(1 ID)	6	2.1	+ve	1.00E-05
scale(Lower_Trunk_Canal_Neuromasts)+Turbulent/Laminar +Trial_Order+(1 ID)	6	2.1	-ve	1.00E-05
scale(Tail_Neuromasts)*Turbulent/Laminar +Trial_Order+(1 ID)	7	3.3	-ve	0.0053
scale(Head_Canal_Neuromasts)*Turbulent/Laminar +Trial_Order+(1 ID)	7	3.4	-ve	0.005
scale(Lower_Trunk_Superficial_Neuromasts)*Turbulent/Laminar +Trial_Order+(1 ID)	7	3.7	-ve	0.0032
scale(Lower_Trunk_Canal_Neuromasts)*Turbulent/Laminar +Trial_Order+(1 ID)	7	4.1	-ve	0.0013
scale(Trunk_Canal_Neuromasts)*Turbulent/Laminar +Trial_Order+(1 ID)	7	4.1	-ve	0.0011
scale(Head_Superficial_Neuromasts)*Turbulent/Laminar +Trial_Order+(1 ID)	7	4.3	+ve	0.0001

Table B.11: Model comparisons using the Akaike Information Criterion scores for neuromast models that explain variability in mean group radius, for the dataset that includes all individuals (hybrids and parent species). Total body length is only considered as a stand-alone main effect.

Model Name	df	dAlCc	Association	LRT
scale(Head_Superficial_Neuromasts)+Turbulent/Laminar +Trial_Order+(1 ID)	6	0	+ve	0.0505
scale(Head_Superficial_Neuromasts)*Turbulent/Laminar +Trial_Order+(1 ID)	7	1.8	+ve	0.0512
scale(Trunk_Superficial_Neuromasts)+Turbulent/Laminar +Trial_Order+(1 ID)	6	6.6	+ve	0.0223
scale(Head_Canal_Neuromasts)*Turbulent/Laminar +Trial_Order+(1 ID)	7	7.4	-ve	0.0277
scale(Head_Canal_Neuromasts)+Turbulent/Laminar +Trial_Order+(1 ID)	6	8.2	-ve	0.0238
scale(Trunk_Superficial_Neuromasts)*Turbulent/Laminar +Trial_Order+(1 ID)	7	8.3	-ve	0
Null	5	9.7	N/A	0.0062
scale(Lower_Trunk_Superficial_Neuromasts)+Turbulent/Laminar +Trial_Order+(1 ID)	6	10.3	+ve	0.0011
scale(Trunk_Canal_Neuromasts)+Turbulent/Laminar +Trial_Order+(1 ID)	6	11.5	-ve	0.0004
scale(Lower_Trunk_Canal_Neuromasts)+Turbulent/Laminar +Trial_Order+(1 ID)	6	11.6	+ve	0.0002
scale(Tail_Neuromasts)+Turbulent/Laminar +Trial_Order+(1 ID)	6	11.7	+ve	9.00E-05
scale(Length)+Turbulent/Laminar +Trial_Order+(1 ID)	6	11.7	+ve	0.0076
scale(Length) *Turbulent/Laminar +Trial_Order+(1 ID)	7	12	+ve	0.0069
scale(Lower_Trunk_Superficial_Neuromasts)*Turbulent/Laminar +Trial_Order+(1 ID)	7	12.2	-ve	0.006
scale(Trunk_Canal_Neuromasts)*Turbulent/Laminar +Trial_Order+(1 ID)	7	12.4	-ve	0.0008
scale(Lower_Trunk_Canal_Neuromasts)*Turbulent/Laminar +Trial_Order+(1 ID)	7	13.5	-ve	0.0003
scale(Taill_Neuromasts)*Turbulent/Laminar +Trial_Order+(1 ID)	7	13.7	+ve	0.0154

Table B.12: Model comparisons using the Akaike Information Criterion scores for neuromast models that explain variability in mean group radius, for the dataset that includes only hybrids. Total body length is only considered as a stand-alone main effect.

Model Name	df	dAlCc	Association	LRT
<pre>scale(Head_Superficial_Neuromasts)+Turbulent/Laminar</pre>	6	0	+ve	0.0417
+Trial_Order+(1 ID)		_		
scale(Head_Superficial_Neuromasts)*Turbulent/Laminar	7	1.5	-ve	0.0443
+Trial_Order+(1 ID)				
scale(Trunk_Superficial_Neuromasts)+Turbulent/Laminar +Trial Order+(1 ID)	6	2.8	+ve	0.0272
scale(Trunk Superficial Neuromasts)*Turbulent/Laminar				
+Trial Order+(1 ID)	7	2.8	-ve	0.0376
scale(Head Canal Neuromasts)+Turbulent/Laminar	~	4.0		0.0404
+Trial_Order+(1 ID)	6	4.9	-ve	0.0164
Null	5	6	N/A	0
scale(Head_Canal_Neuromasts)*Turbulent/Laminar	7	6.1	-ve	0.0205
+Trial_Order+(1 ID)	. '	0.1	-ve	0.0205
scale(Lower_Trunk_Superficial_Neuromasts)+Turbulent/Laminar	6	72	+ve	0.0039
+Trial_Order+(1 ID)	0	1.2		0.0005
scale(Trunk_Canal_Neuromasts)+Turbulent/Laminar	6	7.5	-ve	0.0022
+Trial Order+(1 ID)	_			
scale(Length)+Turbulent/Laminar	6	7.7	+ve	0.0015
+Trial_Order+(1 ID) scale(Tail_Neuromasts)+Turbulent/Laminar				
+Trial Order+(1 ID)	6	7.9	+ve	0.0002
scale(Lower Trunk Canal Neuromasts)+Turbulent/Laminar				· · · · · ·
+Trial_Order+(1 ID)	6	7.9	-ve	0.0001
scale(Trunk_Canal_Neuromasts)*Turbulent/Laminar	7	0.4		0.0004
+Trial_Order+(1 ID)		0.4	-ve	0.0081
scale(Length)*Turbulent/Laminar	7	8.0	+ve	0.0057
+Trial_Order+(1 ID)	Ľ	0.9	110	0.0037
scale(Lower_Trunk_Superficial_Neuromasts)*Turbulent/Laminar	7	91	-ve	0.0044
+Trial_Order+(1 ID)		0.1		0.0044
scale(Tail_Neuromasts)*Turbulent/Laminar	7	9.8	-ve	0.0007
+Trial_Order+(1 ID)				
scale(Lower_Trunk_Canal_Neuromasts)*Turbulent/Laminar	7	9.9	-ve	0.0002
+Trial_Order+(1 ID)				

Table B.13: Model comparisons using the Akaike Information Criterion scores for pore size models that explain variability in mean nearest neighbour distance, for the dataset that includes all individuals (hybrids and parent species), where total body length is included as a covariate term in all models.

Model Name	df	dAlCc	Association	LRT
scale(Otic_Canal_Pore)+Turbulent/Laminar	7	0	-ve	0.0269
+scale(Length)+Trial_Order+(1 ID)	'	0	-ve	0.0209
scale(Infraorbital_Canal_Pore)+Turbulent/Laminar	7	0.6	-ve	0.0241
+scale(Length)+Trial_Order+(1 ID)	'	0.0	-ve	0.0241
scale(Preopercular_Canal_Pore)+Turbulent/Laminar	7	15	-ve	0.0206
+scale(Length)+Trial_Order+(1 ID)	'	1.0	-vc	0.0206
scale(Infraorbital_Canal_Pore)*Turbulent/Laminar	8	1.7	VO	0.0288
+scale(Length)+Trial_Order+(1 ID)	0		-ve	0.0200
scale(Mandibular_Canal_Pore)+Turbulent/Laminar	7	17	-ve	0.0194
+scale(Length)+Trial_Order+(1 ID)	'	1.7	-ve	0.0194
scale(Otic_Canal_Pore)*Turbulent/Laminar	8	1.9		0.0281
+scale(Length)+Trial_Order+(1 ID)	0	1.9	-ve	0.0201
scale(Preopercular_Canal_Pore)*Turbulent/Laminar	8	24		0.0257
+scale(Length)+Trial_Order+(1 ID)	0	2.4	-ve	0.0257
scale(Mandibular_Canal_Pore)*Turbulent/Laminar	8		3.3 -ve	0.0217
+scale(Length)+Trial_Order+(1 ID)	0	3.3	-ve	0.0217
Null	6	4	N/A	0

Table B.14: Model comparisons using the Akaike Information Criterion scores for pore size models that explain variability in mean nearest neighbour distance, for the dataset that includes only hybrids, where total body length is included as a covariate term in all models.

Model Name	df	dAlCc	Association	LRT
scale(Otic_Canal_Pore)+Turbulent/Laminar +scale(Length)+Trial_Order+(1 ID)	7	0	-ve	0.0134
Null	6	0.4	N/A	0
scale(Preopercular_Canal_Pore)+Turbulent/Laminar +scale(Length)+Trial_Order+(1 ID)	7	1.6	-ve	0.0049
scale(Otic_Canal_Pore)*Turbulent/Laminar +scale(Length)+Trial_Order+(1 ID)	8	1.8	+ve	0.0155
scale(Mandibular_Canal_Pore)+Turbulent/Laminar +scale(Length)+Trial_Order+(1 ID)	7	2	-ve	0.0027
scale(Infraorbital_Canal_Pore)+Turbulent/Laminar +scale(Length)+Trial_Order+(1 ID)	7	2.4	-ve	0.0005
scale(Preopercular_Canal_Pore)*Turbulent/Laminar +scale(Length)+Trial_Order+(1 ID)	8	3.7	+ve	0.0056
scale(Mandibular_Canal_Pore)*Turbulent/Laminar +scale(Length)+Trial_Order+(1 ID)	8	4.2	-ve	0.0029
scale(Infraorbital_Canal_Pore)*Turbulent/Laminar +scale(Length)+Trial_Order+(1 ID)	8	4.6	-ve	0.0007

Table B.15: Model comparisons using the Akaike Information Criterion scores for pore size models that explain variability in mean group radius, for the dataset that includes all individuals (hybrids and parent species), where total body length is included as a covariate term in all models.

Model Name	df	dAICc	Association	LRT
scale(Preopercular_Canal_Pore)+Turbulent/Laminar +scale(Length)+Trial_Order+(1 ID)	7	0	-ve	0.0183
scale(Otic_Canal_Pore)+Turbulent/Laminar +scale(Length)+Trial_Order+(1 ID)	7	0.2	-ve	0.0173
scale(Preopercular_Canal_Pore)*Turbulent/Laminar +scale(Length)+Trial_Order+(1 ID)	8	1.7	-ve	0.0201
Null	6	2	N/A	0
scale(Otic_Canal_Pore)*Turbulent/Laminar +scale(Length)+Trial_Order+(1 ID)	8	2.4	-ve	0.0173
scale(Mandibular_Canal_Pore)+Turbulent/Laminar +scale(Length)+Trial_Order+(1 ID)	7	3.2	-ve	0.0045
scale(Infraorbital_Canal_Pore)+Turbulent/Laminar +scale(Length)+Trial_Order+(1 ID)	7	3.3	-ve	0.0038
scale(Mandibular_Canal_Pore)*Turbulent/Laminar	8	5.1	-ve	0.0054
+scale(Length)+Trial_Order+(1 ID)				
scale(Infraorbital_Canal_Pore)*Turbulent/Laminar +scale(Length)+Trial_Order+(1 ID)	8	5.1	-ve	0.0052

Table B.16: Model comparisons using the Akaike Information Criterion scores for pore size models that explain variability in mean group radius, for the dataset that includes only hybrids, where total body length is included as a covariate term in all models.

Model Name	df	dAlCc	Association	LRT
scale(Otic_Canal_Pore)+Turbulent/Laminar +scale(Length)+Trial_Order+(1 ID)	7	0	-ve	0.012
Null	6	0.1	N/A	0
scale(Preopercular_Canal_Pore)+Turbulent/Laminar +scale(Length)+Trial_Order+(1 ID)	7	0.5	-ve	0.0094
scale(Infraorbital_Canal_Pore)+Turbulent/Laminar +scale(Length)+Trial_Order+(1 ID)	7	1.4	-ve	0.0044
scale(Otic_Canal_Pore)*Turbulent/Laminar +scale(Length)+Trial_Order+(1 ID)	8	1.9	+ve	0.0135
scale(Mandibular_Canal_Pore)+Turbulent/Laminar +scale(Length)+Trial_Order+(1 ID)	7	2.2	-ve	0.0004
scale(Preopercular_Canal_Pore)*Turbulent/Laminar +scale(Length)+Trial_Order+(1 ID)	8	2.6	+ve	0.0098
scale(Infraorbital_Canal_Pore)*Turbulent/Laminar +scale(Length)+Trial_Order+(1 ID)	8	3.6	+ve	0.0044
scale(Mandibular_Canal_Pore)*Turbulent/Laminar +scale(Length)+Trial_Order+(1 ID)	8	4.3	-ve	0.0005

Table B.17: Model comparisons using the Akaike Information Criterion scores for pore size models that explain variability in mean distance to nearest upstream neighbour, for the dataset that includes all individuals (hybrids and parent species), where total body length is included as a covariate term in all models.

Model Name	df	dAlCc	Associations	LRT
scale(Preopercular_Canal_Pore)+Turbulent/Laminar	7	0	-ve	0.0337
+scale(Length)+Trial_Order+(1 ID)	'	0		0.0007
scale(Otic_Canal_Pore)+Turbulent/Laminar+scale(Leng	7	0	-ve	0.0336
+Trial_Order+(1 ID)	<u> </u>	Ŭ	-vc	0.0000
scale(Mandibular_Canal_Pore)+Turbulent/Laminar	7	10	-ve	0.0253
+scale(Length)+Trial_Order+(1 ID)	'	1.9	-ve	0.0200
scale(Preopercular_Canal_Pore)*Turbulent/Laminar	8	2	-ve	0.0341
+scale(Length)+Trial_Order+(1 ID)	0	2		0.0041
Scale(Otic_Canal_Pore)*Turbulent/Laminar+scale(Leng	8	22	+ve	0.0336
+Trial_Order+(1 ID)	0	2.2		0.0000
scale(Infraorbital_Canal_Pore)+Turbulent/Laminar	7	24	-ve	0.0235
+scale(Length)+Trial_Order+(1 ID)		2.4		0.0200
scale(Mandibular_Canal_Pore)*Turbulent/Laminar	8	11	-ve	0.0254
+scale(Length)+Trial_Order+(1 ID)	0	4.1		0.0204
scale(Infraorbital_Canal_Pore)*Turbulent/Laminar	8	13	4.3 -ve	0.0243
+scale(Length)+Trial_Order+(1 ID)	0	4.5	- 10	
Null	6	5.6	N/A	0

Table B.18: Model comparisons using the Akaike Information Criterion scores for pore size models that explain variability in mean distance to nearest upstream neighbour, for the dataset that includes only hybrids, where total body length is included as a covariate term in all models.

Model Name	df	dAlCc	Associations	LRT
Null	6	0	N/A	0
scale(Otic_Canal_Pore)+Turbulent/Laminar	7	0.1	-ve	0.011
+scale(Length)+Trial_Order+(1 ID)	Ľ	0.1	-vc	0.011
Scale(Otic_Canal_Pore)*Turbulent/Laminar	8	0.4	+ve	0.021
+scale(Length)+Trial_Order+(1 ID)	Ŭ	0.4		0.021
scale(Preopercular_Canal_Pore)+Turbulent/Laminar	7	12	-ve	0.005
+scale(Length)+Trial_Order+(1 ID)	Ĺ	1.2	-ve	0.000
scale(Preopercular_Canal_Pore)*Turbulent/Laminar	8	17	+ve	0.014
+scale(Length)+Trial_Order+(1 ID)	Ŭ	1.7		0.014
scale(Infraorbital_Canal_Pore)+Turbulent/Laminar	7	1 9	+ve	0.0016
+scale(Length)+Trial_Order+(1 ID)	Ĺ	1.5		0.0010
scale(Mandibular_Canal_Pore)+Turbulent/Laminar	7	19	VO	0.0013
+scale(Length)+Trial_Order+(1 ID)	'	1.5	-vc	
scale(Infraorbital_Canal_Pore)*Turbulent/Laminar	8	3.0	+ve	0.0026
+scale(Length)+Trial_Order+(1 ID)	Ŭ	0.5		
scale(Mandibular_Canal_Pore)*Turbulent/Laminar	8	11	1 -ve	0.0013
+scale(Length)+Trial_Order+(1 ID)	0	4.1		

Table B.19: Model comparisons using the Akaike Information Criterion scores for pore size models that explain variability in mean distance to nearest neighbour in 'field of flow detection', for the dataset that includes all individuals (hybrids and parent species), where total body length is included as a covariate term in all models.

Model Name	df	dAlCc	Associations	LRT
scale(Preopercular_Canal_Pore)+Turbulent/Laminar	7	0	-ve	0.0399
+scale(Length)+Trial_Order+(1 ID)	'	0	-ve	0.0399
scale(Otic_Canal_Pore)+Turbulent/Laminar	7	1.5	-ve	0.0337
+scale(Length)+Trial_Order+(1 ID)	ĺ	1.5	-ve	0.0337
scale(Preopercular_Canal_Pore)*Turbulent/Laminar	8	2.1	+ve	0.0402
+scale(Length)+Trial_Order+(1 ID)		2.1	TVC	0.0402
scale(Mandibular_Canal_Pore)+Turbulent/Laminar	7	27	-ve	0.0285
+scale(Length)+Trial_Order+(1 ID)		2.1		0.0205
scale(Infraorbital_Canal_Pore)+Turbulent/Laminar	7	20	-ve	0.0279
+scale(Length)+Trial_Order+(1 ID)	1	2.0		0.0219
Scale(Otic_Canal_Pore)*Turbulent/Laminar	8	2.4	+ve	0.0346
+scale(Length)+Trial_Order+(1 ID)	0	5.4	TVC	0.0340
scale(Mandibular_Canal_Pore)*Turbulent/Laminar	8	12	+ve	0.0308
+scale(Length)+Trial_Order+(1 ID)	0	4.5	+ve	0.0300
scale(Infraorbital_Canal_Pore)*Turbulent/Laminar	8	40	+ve	0.0283
+scale(Length)+Trial_Order+(1 ID)		4.5		
Null	6	7.1	N/A	0

Table B.20: Model comparisons using the Akaike Information Criterion scores for pore size models that explain variability in mean distance to nearest neighbour in 'field of flow detection', for the dataset that includes only hybrids, where total body length is included as a covariate term in all models.

Model Name	df	dAlCc	Association s	LRT
Null	6	0	N/A	0
Scale(Otic_Canal_Pore)*Turbulent/Laminar	8	0.1	+ve	0.0224
+scale(Length)+Trial_Order+(1 ID)	Ŭ	0.1	140	
scale(Preopercular_Canal_Pore)*Turbulent/Laminar	8	0.9	+ve	0.0181
+scale(Length)+Trial_Order+(1 ID)	0	0.5	110	0.0101
scale(Otic_Canal_Pore)+Turbulent/Laminar	7	11	10	0.0056
+scale(Length)+Trial_Order+(1 ID)		1.1	-ve	0.0000
scale(Preopercular_Canal_Pore)+Turbulent/Laminar	7	17	-ve	0.0026
+scale(Length)+Trial_Order+(1 ID)	1	1.7	-ve	0.0020
scale(Infraorbital_Canal_Pore)+Turbulent/Laminar	7	10	+ve	0.0016
+scale(Length)+Trial_Order+(1 ID)	<i>'</i>	1.5	TVC	
scale(Mandibular_Canal_Pore)+Turbulent/Laminar	7	2	-ve	0.0000
+scale(Length)+Trial_Order+(1 ID)	'	2	-ve	0.0009
scale(Infraorbital_Canal_Pore)*Turbulent/Laminar	8	2.0	+ve	0.0075
+scale(Length)+Trial_Order+(1 ID)	0	2.9	tve	0.0075
scale(Mandibular_Canal_Pore)*Turbulent/Laminar	8	2.2	3 +ve	0.0055
+scale(Length)+Trial_Order+(1 ID)	0	3.3	+ve	

Table B.21: Model comparisons using the Akaike Information Criterion scores for pore size models that explain variability in mean nearest neighbour distance, for the dataset that all individuals (hybrids and parent species). Total body length is only considered as a stand-alone main effect.

Model Name	df	dAICc	Associations	LRT
scale(Otic_Canal_Pore)+Turbulent/Laminar	6	0	-ve	0.0349
+Trial_Order+(1 ID)	Ŭ	Ŭ	-10	0.0043
scale(Infraorbital_Canal_Pore)+Turbulent/Laminar	6	0.0	-ve	0.0312
+Trial_Order+(1 ID)	Ľ	0.0	10	0.0012
scale(Preopercular_Canal_Pore)+Turbulent/Laminar	6	18	-ve	0.0272
+Trial_Order+(1 ID)	Ŭ	1.0	-vc	0.0272
Scale(Otic_Canal_Pore)*Turbulent/Laminar	7	1 9	-ve	0.0361
+Trial_Order+(1 ID)	Ľ	1.5	10	0.0001
scale(Infraorbital_Canal_Pore)*Turbulent/Laminar	7	1 9	-ve	0.0359
+Trial_Order+(1 ID)		1.5		0.0000
scale(Mandibular_Canal_Pore)+Turbulent/Laminar	6	19	-ve	0.0267
+Trial_Order+(1 ID)	Ľ	1.0	10	0.0207
scale(Preopercular_Canal_Pore)*Turbulent/Laminar	7	27	-ve	0.0324
+Trial_Order+(1 ID)	`	2.1		
scale(Mandibular_Canal_Pore)*Turbulent/Laminar	7	3.5	Ve	0.029
+Trial_Order+(1 ID)	Ľ	0.0		0.020
Null	5	5.9	N/A	0
scale(Length)+Turbulent/Laminar	6	A	-ve	0.0089
+Trial_Order+(1 ID)				0.0003
scale(Length)*Turbulent/Laminar	7	6.5	+ve	0.0162
+Trial_Order+(1 ID)	1	0.0	ive	0.0102

Table B.22: Model comparisons using the Akaike Information Criterion scores for pore size models that explain variability in mean nearest neighbour distance, for the dataset that includes only hybrids. Total body length is only considered as a stand-alone main effect.

Model Name	df	dAICc	Associations	LRT
scale(Otic_Canal_Pore)+Turbulent/Laminar	6	0	-ve	0.0212
+Trial_Order+(1 ID)	0	Ŭ	-ve	0.0212
scale(Preopercular_Canal_Pore)+Turbulent/Laminar	6	17	-ve	0.0124
+Trial_Order+(1 ID)		1.7	-vc	0.0124
Scale(Otic_Canal_Pore)*Turbulent/Laminar	7	1.8	+ve	0.0233
+Trial_Order+(1 ID)	,	1.0	TVC	0.0200
Null	5	1.9	N/A	0
scale(Mandibular_Canal_Pore)+Turbulent/Laminar	6	23	-ve	0.009
+Trial_Order+(1 ID)	0	2.0		0.009
scale(Length)+Turbulent/Laminar	6	25	-ve	0.0079
+Trial_Order+(1 ID)	Ŭ	2.0	10	0.0073
scale(Infraorbital_Canal_Pore)+Turbulent/Laminar	6	3.1	-ve	0.005
+Trial_Order+(1 ID)	0	0.1	-ve	
scale(Length)*Turbulent/Laminar	7	3.4	+ve	0.0148
+Trial_Order+(1 ID)	Ľ	5.4		0.0146
scale(Preopercular_Canal_Pore)*Turbulent/Laminar	7	37	+ve	0.0132
+Trial_Order+(1 ID)	'	0.7		0.0132
scale(Mandibular_Canal_Pore)*Turbulent/Laminar	7	11	-ve	0.0093
+Trial_Order+(1 ID)		4.4	-ve	0.0093
scale(Infraorbital_Canal_Pore)*Turbulent/Laminar	7	5.0	5.2 -ve	0.0051
+Trial_Order+(1 ID)		0.2	-ve	0.0051

Table B.23: Model comparisons using the Akaike Information Criterion scores for pore size models that explain variability in mean group radius, for the dataset that includes all individuals (hybrids and parent species). Total body length is only considered as a stand-alone main effect.

Model Name	df	dAlCc	Associations	LRT
scale(Preopercular_Canal_Pore)+Turbulent/Laminar	6	0	-ve	0.0156
+Trial_Order+(1 ID)	Ŭ	, v		0.0100
scale(Otic_Canal_Pore)+Turbulent/Laminar	6	0.5	-ve	0.0136
+Trial_Order+(1 ID)	Ŭ	0.0	10	0.0100
Null	5	1.4	N/A	0
scale(Preopercular_Canal_Pore)*Turbulent/Laminar	7	17	-ve	0.0174
+Trial_Order+(1 ID)	<i>'</i>	1.7	-vc	0.0174
Scale(Otic_Canal_Pore)*Turbulent/Laminar	7	7 2.6	-VP	0.0136
+Trial_Order+(1 ID)	'		-vc	0.0150
scale(Mandibular_Canal_Pore)+Turbulent/Laminar	6	2.8	-ve	0.0034
+Trial_Order+(1 ID)		2.0		0.0004
scale(Infraorbital_Canal_Pore)+Turbulent/Laminar	6	20	9 -ve	0.0031
+Trial_Order+(1 ID)	0	2.9		0.0001
scale(Length)+Turbulent/Laminar	6	35	+ve	9.00E-05
+Trial_Order+(1 ID)	0	5.5	TVC	9.00L-03
scale(Length)*Turbulent/Laminar	7	4	+ve	0.0076
+Trial_Order+(1 ID)	'	-		0.0070
scale(Infraorbital_Canal_Pore)*Turbulent/Laminar	7	47	7 -ve	0.0045
+Trial_Order+(1 ID)	Ľ	4.1	-ve	0.0045
scale(Mandibular_Canal_Pore)*Turbulent/Laminar	7	47	-ve	0.0043
+Trial_Order+(1 ID)		4.7	-ve	0.0043

Table B.24: Model comparisons using the Akaike Information Criterion scores for pore size models that explain variability in mean group radius, for the dataset that includes only hybrids. Total body length is only considered as a stand-alone main effect.

Model Name	df	dAICc	Associations	LRT
Null	5	0	N/A	0
scale(Infraorbital_Canal_Pore)+Turbulent/Laminar	6	1	+ve	0.0059
+Trial_Order+(1 ID)	0		TVC	0.0009
scale(Otic_Canal_Pore)+Turbulent/Laminar	6	1 /	-ve	0.0041
+Trial_Order+(1 ID)	0	1.4	-ve	0.0041
scale(Preopercular_Canal_Pore)+Turbulent/Laminar	6	1.8	-ve	0.002
+Trial_Order+(1 ID)	Ŭ	1.0	-vc	0.002
scale(Length)+Turbulent/Laminar	6	10	+ve	0.0015
+Trial_Order+(1 ID)	0	1.9		0.0015
scale(Mandibular_Canal_Pore)+Turbulent/Laminar	6	21	+ve	0.0001
+Trial_Order+(1 ID)	Ŭ	2.1		0.0001
scale(Infraorbital_Canal_Pore)*Turbulent/Laminar	7	30	+ve	0.0059
+Trial_Order+(1 ID)	'	0.2		0.0005
scale(Length)*Turbulent/Laminar	7	30	+ve	0.0057
+Trial_Order+(1 ID)	<i>'</i>	0.2	TVC	0.0007
Scale(Otic_Canal_Pore)*Turbulent/Laminar	7	33	+ve	0.0055
+Trial_Order+(1 ID)	1	0.0		0.0000
scale(Preopercular_Canal_Pore)*Turbulent/Laminar	7	3.8	8 +ve	0.0025
+Trial_Order+(1 ID)				0.0020
scale(Mandibular_Canal_Pore)*Turbulent/Laminar	7	1.2	-ve	0.0001
+Trial_Order+(1 ID)		4.3	-ve	0.0001



APPENDIX C

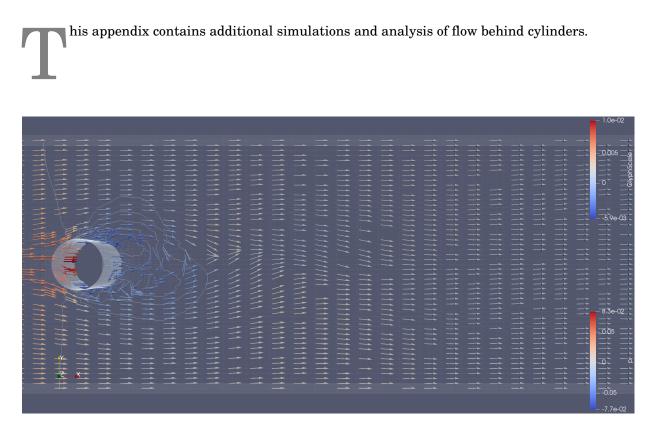


Figure C.1: Simulated flow behind a cylinder with 100mm diameter at 0.1m/s, with glyphs showing the flow velocities and contour lines showing the different pressure levels.

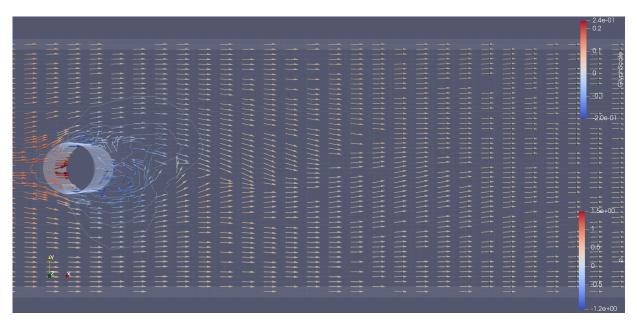


Figure C.2: Simulated flow behind a cylinder with 100mm diameter at 0.5m/s, with glyphs showing the flow velocities and contour lines showing the different pressure levels.

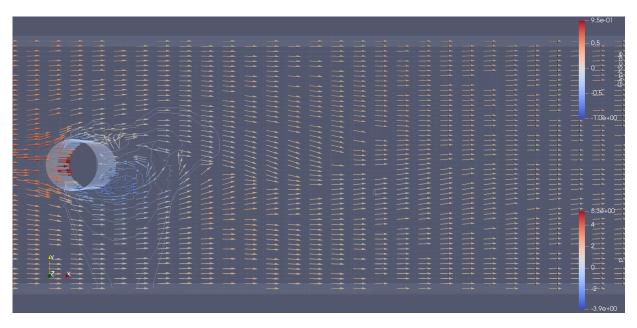


Figure C.3: Simulated flow behind a cylinder with 100mm diameter at 1m/s, with glyphs showing the flow velocities and contour lines showing the different pressure levels.



Figure C.4: Simulated flow behind a cylinder with 150 mm diameter at 0.5 m/s, with glyphs showing the flow velocities and contour lines showing the different pressure levels.



Figure C.5: Simulated flow behind a cylinder with 150mm diameter at 0.5m/s, with glyphs showing the flow velocities and contour lines showing the different pressure levels.



Figure C.6: Simulated flow behind a cylinder with 150mm diameter at 0.5m/s, with glyphs showing the flow velocities and contour lines showing the different pressure levels.



APPENDIX D

his appendix contains preliminary designs of ways to adapt the current physical sensor to improve utility.



Figure D.1: Preliminary CAD design showing (a) an enclosure containing an elastic and conductive haircell and bearing strips of wiring embedded in one wall and (b) the haircell deflecting in response to a flow stimuli affecting its other end (not pictured) and being pressed against the strips of wiring. This action then complets the circuit and allows resistance to be measured, with that being dependent on how many strips of wiring in the wall the haircell crosses.



Figure D.2: Preliminary CAD design showing an enclosure containing a haircell made from a magnetic material positioned between two magnetic field sensors. As the haircell deflects in response to flows affecting its other end (not pictured), the magnetic field sensors detect and measure this.

BIBLIOGRAPHY

[1] Developing a Novel Robotic Fish With Antagonistic Artificial Muscle Actuators, vol. Volume 1: Aerospace Applications; Advances in Control Design Methods; Bio Engineering Applications; Advances in Non-Linear Control; Adaptive and Intelligent Systems Control; Advances in Wind Energy Systems; Advances in Robotics; Assistive and Rehabilitation Robotics; Biomedical and Neural Systems Modeling, Diagnostics, and Control; Bio-Mechatronics and Physical Human Robot; Advanced Driver Assistance Systems and Autonomous Vehicles; Automotive Systems of Dynamic Systems and Control Conference, 10 2017.

V001T30A011.

- [2] 57. SKAUG H AND FOURNIER D AND NIELSEN A AND MAGNUSSON A AND BOLKER B, Generalized Linear Mixed Models using AD Model Builder, R package version 0.7.5, 2019.
- [3] A. T. ABDULSADDA AND X. TAN, An artificial lateral line system using ipmc sensor arrays, International Journal of Smart and Nano Materials, 3 (2012), pp. 226–242.
- [4] A. T. ABDULSADDA AND X. TAN, Nonlinear estimation-based dipole source localization for artificial lateral line systems, Bioinspiration & Biomimetics, 8 (2013), p. 026005.
- [5] C. ABELS, A. QUALTIERI, M. D. VITTORIO, W. M. MEGILL, AND F. RIZZI, A bio-inspired real-time capable artificial lateral line system for freestream flow measurements, Bioinspiration & Biomimetics, 11 (2016), p. 035006.
- [6] A. AHRARI, H. LEI, M. A. SHARIF, K. DEB, AND X. TAN, Reliable underwater dipole source characterization in 3d space by an optimally designed artificial lateral line system, Bioinspiration & Biomimetics, 12 (2017), p. 036010.
- B. ALLOTTA, A. CAITI, M. COCCO, C. COLOMBO, W. DAVIDDI, L. GUALDESI, D. MONICA, D. MORONI, G. PIERI, O. SALVETTI, AND M. TAMPUCC, Thesaurus: Techniques for underwater exploration and archeology through swarms of autonomous vehicles, 10 2011.
- [8] M. ASADNIA, A. G. P. KOTTAPALLI, R. HAGHIGHI, A. CLOITRE, P. V. Y ALVARADO, J. MIAO, AND M. TRIANTAFYLLOU, MEMS sensors for assessing flow-related control of

an underwater biomimetic robotic stingray, Bioinspiration & Biomimetics, 10 (2015), p. 036008.

- M. ASADNIA, A. G. P. KOTTAPALLI, D. KARAVITAKI, M. EBRAHIMI WARKIANI, J. MIAO, D. COREY, AND M. TRIANTAFYLLOU, From biological cilia to artificial flow sensors: Biomimetic soft polymer nanosensors with high sensing performance, Scientific Reports, 6 (2016), p. 32955.
- [10] M. ASADNIA, A. G. P. KOTTAPALLI, J. MIAO, M. E. WARKIANI, AND M. S. TRIANTAFYL-LOU, Artificial fish skin of self-powered micro-electromechanical systems hair cells for sensing hydrodynamic flow phenomena, Journal of The Royal Society Interface, 12 (2015), p. 20150322.
- [11] J. AYERS, P. ZAVRACKY, N. MCGRUER, D. MASSA, W. VORUS, R. MUKHERJEE, AND S. CURRIE, A modular behavioral-based architecture for biomimetic autonomous underwater robots, Proceedings of the Autonomous Vehicles in Mine Countermeasures Symposium, 5 (1998), pp. 15–21.
- [12] F. AZIS, M. ARAS, M. RASHID, M. OTHMAN, AND S. ABDULLAH, Problem identification for underwater remotely operated vehicle (rov): A case study, Procedia Engineering, 41 (2012), pp. 554 – 560.

International Symposium on Robotics and Intelligent Sensors 2012 (IRIS 2012).

- [13] C. BAKER AND J. MONTGOMERY, Lateral line mediated rheotaxis in the antarctic fish pagothenia borchgrevinki, Polar Biology, 21 (1999), pp. 305–309.
- [14] C. BARRET, Aerobots and hydrobots for planetary exploration.
- [15] D. K. BASSETT, A. G. CARTON, AND J. C. MONTGOMERY, Flowing water decreases hydrodynamic signal detection in a fish with an epidermal lateral-line system, Marine and Freshwater Research, 57 (2006), pp. 611–617.
- [16] E. A. BECKER, N. C. BIRD, AND J. F. WEBB, Post-embryonic development of canal and superficial neuromasts and the generation of two cranial lateral line phenotypes, Journal of morphology, 277 (2016), pp. 1273–1291.
- [17] M. BECKMANN, T. ERÓS, A. SCHMITZ, AND H. BLECKMANN, Number and distribution of superficial neuromasts in twelve common european cypriniform fishes and their relationship to habitat occurrence, International Review of Hydrobiology, 95 (2010), pp. 273–284.
- [18] F. BERLINGER, M. GAUCI, AND R. NAGPAL, Implicit coordination for 3d underwater collective behaviors in a fish-inspired robot swarm, Science Robotics, 6 (2021), p. eabd8668.

- [19] J. BLAXTER, J. GRAY, AND E. DENTON, Sound and startle responses in herring shoals, Journal of the Marine Biological Association of the United Kingdom, 61 (1981), pp. 851– 869.
- [20] J. H. S. BLAXTER AND R. S. BATTY, Herring behaviour in the dark: Responses to stationary and continuously vibrating obstacles, Journal of the Marine Biological Association of the United Kingdom, 65 (1985), p. 1031–1049.
- [21] J. H. S. BLAXTER, J. A. B. GRAY, AND A. C. G. BEST, Structure and development of the free neuromasts and lateral line system of the herring, Journal of the Marine Biological Association of the United Kingdom, 63 (1983), p. 247–260.
- B. BOLKER AND R. D. C. TEAM, bbmle: Tools for General Maximum Likelihood Estimation, 2017.
 R package version 1.0.20.
- [23] F. BONIN-FONT, A. ORTIZ, AND G. OLIVER, Visual navigation for mobile robots: A survey, Journal of Intelligent and Robotic Systems, 53 (2008), p. 263.
- [24] M. BORA, A. G. P. KOTTAPALLI, J. MIAO, AND M. TRIANTAFYLLOU, Biomimetic hydrogelcnt network induced enhancement of fluid-structure interactions for ultrasensitive nanosensors, NPG Asia Materials, 9 (2017), p. e440.
- [25] M. BORA, A. G. P. KOTTAPALLI, J. M. MIAO, AND M. S. TRIANTAFYLLOU, Fish-inspired self-powered microelectromechanical flow sensor with biomimetic hydrogel cupula, APL Materials, 5 (2017), p. 104902.
- [26] P. BRADSHAW AND R. PANKHURST, The design of low-speed wind tunnels, Progress in Aerospace Sciences, 5 (1964), pp. 1–69.
- [27] M. BRAMBILLA, E. FERRANTE, M. BIRATTARI, AND M. DORIGO, Swarm robotics: a review from the swarm engineering perspective, Swarm Intelligence, 7 (2013), pp. 1–41.
- [28] A. D. BROWN, T. D. MUSSEN, J. A. SISNEROS, AND A. B. COFFIN, Reevaluating the use of aminoglycoside antibiotics in behavioral studies of the lateral line, Hearing research, 272 (2011), pp. 1–4.
 21055458[pmid].
- [29] J. M. BUTLER, K. E. FIELD, AND K. P. MARUSKA, Cobalt chloride treatment used to ablate the lateral line system also impairs the olfactory system in three freshwater fishes, PloS one, 11 (2016), pp. e0159521–e0159521.
 27416112[pmid].

- [30] J. M. BUTLER AND K. P. MARUSKA, The mechanosensory lateral line is used to assess opponents and mediate aggressive behaviors during territorial interactions in an african cichlid fish, Journal of Experimental Biology, 218 (2015), pp. 3284–3294.
- [31] P. CAIN, Navigation in familiar environments by the weakly electric elephantnose fish, gnathonemus petersii l. (mormyriformes, teleostei), Ethology, 99 (1995), pp. 332–349.
- [32] D. CARPUTO AND A. BARONE, Ploidy level manipulations in potato through sexual hybridisation, Annals of Applied Biology, 146 (2005), pp. 71–79.
- [33] A. CARRILLO AND M. J. MCHENRY, Zebrafish learn to forage in the dark, Journal of Experimental Biology, 219 (2016), pp. 582–589.
- [34] L. CATTAFESTA, C. BAHR, AND J. MATHEW, Fundamentals of Wind-Tunnel Design, American Cancer Society.
- [35] B. P. CHAGNAUD, H. BLECKMANN, AND J. ENGELMANN, Neural responses of goldfish lateral line afferents to vortex motions, Journal of Experimental Biology, 209 (2006), pp. 327–342.
- [36] B. P. CHAGNAUD, H. BLECKMANN, AND M. H. HOFMANN, Kármán vortex street detection by the lateral line, Journal of Comparative Physiology A, 193 (2007), pp. 753–763.
- [37] A. C. CHAMBERLAIN AND C. C. IOANNOU, Turbidity increases risk perception but constrains collective behaviour during foraging by fish shoals, Animal Behaviour, 156 (2019), pp. 129 – 138.
- [38] J. CHEN, J. ENGEL, AND C. LIU, Development of polymer-based artificial haircell using surface micromachining and 3d assembly, in TRANSDUCERS '03. 12th International Conference on Solid-State Sensors, Actuators and Microsystems. Digest of Technical Papers (Cat. No.03TH8664), vol. 2, 2003, pp. 1035–1038 vol.2.
- [39] N. CHEN, C. TUCKER, J. M. ENGEL, Y. YANG, S. PANDYA, AND C. LIU, Design and characterization of artificial haircell sensor for flow sensing with ultrahigh velocity and angular sensitivity, Journal of Microelectromechanical Systems, 16 (2007), pp. 999– 1014.
- [40] J.-W. CHON, D. H. KIM, J. C. AHN, M. G. KIM, L. G. TRAN, AND W.-T. PARK, Artificial hair cell flow sensor with ball joint, in 2017 19th International Conference on Solid-State Sensors, Actuators and Microsystems (TRANSDUCERS), 2017, pp. 1120–1123.
- [41] S. COOMBS, C. BRAUN, AND B. DONOVAN, The orienting response of lake michigan mottled sculpin is mediated by canal neuromasts, Journal of Experimental Biology, 204 (2001), pp. 337–348.

- [42] S. COOMBS, J. JANSSEN, AND J. F. WEBB, Diversity of lateral line systems: Evolutionary and functional considerations, in Sensory Biology of Aquatic Animals, J. Atema, R. R. Fay, A. N. Popper, and W. N. Tavolga, eds., New York, NY, 1988, Springer New York, pp. 553–593.
- [43] B. CURČIĆ-BLAKE AND S. M. VAN NETTEN, Source location encoding in the fish lateral line canal, Journal of Experimental Biology, 209 (2006), pp. 1548–1559.
- [44] L. DEVRIES, F. D. LAGOR, H. LEI, X. TAN, AND D. A. PALEY, Distributed flow estimation and closed-loop control of an underwater vehicle with a multi-modal artificial lateral line, Bioinspiration & Biomimetics, 10 (2015), p. 025002.
- [45] S. DIJKGRAAF, The functioning and significance of the lateral-line organs, Biological Reviews, 38 (1963), pp. 51–105.
- [46] E. DRUCKER AND G. LAUDER, Experimental hydrodynamics of fish locomotion: Functional insights from wake visualization, Integrative and comparative biology, 42 (2002), pp. 243–57.
- [47] M. DUNBABIN AND L. MARQUES, Robots for environmental monitoring: Significant advancements and applications, IEEE Robotics Automation Magazine, 19 (2012), pp. 24– 39.
- [48] J. DUSEK, A. G. P. KOTTAPALLI, M. E. WOO, M. ASADNIA, J. MIAO, J. H. LANG, AND M. S. TRIANTAFYLLOU, Development and testing of bio-inspired microelectromechanical pressure sensor arrays for increased situational awareness for marine vehicles, Smart Materials and Structures, 22 (2012), p. 014002.
- [49] D. E. EDGLEY AND M. J. GENNER, Adaptive diversification of the lateral line system during cichlid fish radiation, iScience, 16 (2019), pp. 1 – 11.
- [50] H. EHRLICH, Fish skin: from clothing to tissue engineering, in Biological Materials of Marine Origin, Springer, 2015, pp. 263–276.
- [51] J. ELDER AND S. COOMBS, The influence of turbulence on the sensory basis of rheotaxis, Journal of comparative physiology. A, Neuroethology, sensory, neural, and behavioral physiology, 201 (2015), p. 667–680.
- [52] J. ENGEL, J. CHEN, C. LIU, AND D. BULLEN, Polyurethane rubber all-polymer artificial hair cell sensor, Journal of Microelectromechanical Systems, 15 (2006), pp. 729–736.
- [53] J. ENGELMANN, W. HANKE, AND H. BLECKMANN, Lateral line reception in still- and running water, Journal of comparative physiology. A, Neuroethology, sensory, neural, and behavioral physiology, 188 (2002), pp. 513–26.

- [54] Z. FAN, J. CHEN, J. ZOU, D. BULLEN, C. LIU, AND F. DELCOMYN, Design and fabrication of artificial lateral line flow sensors, Journal of Micromechanics and Microengineering, 12 (2002), pp. 655–661.
- [55] K. FAUCHER, E. PARMENTIER, C. BECCO, N. VANDEWALLE, AND P. VANDEWALLE, Fish lateral system is required for accurate control of shoaling behaviour. animal behaviour, 79, 679-687, vol. 79, 01 2010, pp. 679–687.
- [56] K. FEITL, V. NGO, AND M. MCHENRY, Are fish less responsive to a flow stimulus when swimming?, The Journal of experimental biology, 213 (2010), pp. 3131–7.
- [57] M. FERRERA, J. MORAS, P. TROUVÉ-PELOUX, AND V. CREUZE, Real-time monocular visual odometry for turbid and dynamic underwater environments, Sensors, 19 (2019).
- [58] F. FISH, Swimming strategies for energy economy, Fish Locomotion: An Eco-ethological Perspective, (2010).
- [59] D. A. FOURNIER, H. J. SKAUG, J. ANCHETA, J. IANELLI, A. MAGNUSSON, M. N. MAUN-DER, A. NIELSEN, AND J. SIBERT, Ad model builder: Using automatic differentiation for statistical inference of highly parameterized complex nonlinear models, Optimization Methods and Software, 27 (2012), p. 233–249.
- [60] F. B. GESSNER, The origin of secondary flow in turbulent flow along a corner, Journal of Fluid Mechanics, 58 (1973), p. 1–25.
- [61] P. H. GREENWOOD, The haplochromine fishes of the east african lakes; collected papers on their taxonomy, biology and evolution (with an introduction and species index), (1981).
- [62] L. GUO, K. XU, J. LI, AND C. LIU, A mems flow sensor based on fish lateral line sensing system, Microsystem Technologies, (2021).
- [63] Z. GUO ZHOU AND Z. WEN LIU, Biomimetic cilia based on mems technology, Journal of Bionic Engineering, 5 (2008), pp. 358 – 365.
- [64] H. R. GÜTTINGER, The integration of learnt and genetically programmed behaviour, Zeitschrift für Tierpsychologie, 49 (1979), pp. 285–303.
- [65] A. HACKBARTH, E. KREUZER, AND E. SOLOWJOW, *Hippocampus: A micro underwater vehicle for swarm applications*, in 2015 IEEE/RSJ International Conference on Intelligent Robots and Systems (IROS), 2015, pp. 2258–2263.
- [66] E. HAN, K. HO OH, S. PARK, Y. CHAN RAH, H.-C. PARK, S. KOUN, AND J. CHOI, Analysis of behavioral changes in zebrafish (danio rerio) larvae caused by aminoglycoside-induced damage to the lateral line and muscles, NeuroToxicology, 78 (2020), pp. 134–142.

- [67] S. HAUERT AND S. N. BHATIA, Mechanisms of cooperation in cancer nanomedicine: towards systems nanotechnology, Trends in Biotechnology, 32 (2014), pp. 448–455.
 Special Issue: Next Generation Therapeutics.
- [68] C. C. HEMMINGS, Olfaction and vision in fish schooling, Journal of Experimental Biology, 45 (1966), pp. 449–464.
- [69] D. HOEKSTRA AND J. JANSSEN, Lateral line receptivity in the mottled sculpin (cottus bairdi), Copeia, 1986 (1986), pp. 91–96.
- [70] E. HONARY, F. MCQUADE, R. WARD, I. WOODROW, A. SHAW, D. BARNES, AND M. FYFE, Robotic experiments with cooperative aerobots and underwater swarms, Robotica, 27 (2009), pp. 37 – 49.
- [71] Q. HU, C. WEI, Y. LIU, AND Z. ZHAO, A review of biomimetic artificial lateral line detection technology for unmanned underwater vehicles, in Intelligent Robotics and Applications, H. Yu, J. Liu, L. Liu, Z. Ju, Y. Liu, and D. Zhou, eds., Cham, 2019, Springer International Publishing, pp. 501–516.
- [72] C. D. HULSEY, *Cichlid genomics and phenotypic diversity in a comparative context*, Integrative and Comparative Biology, 49 (2009), pp. 618–629.
- [73] C. C. IOANNOU, Swarm intelligence in fish? the difficulty in demonstrating distributed and self-organised collective intelligence in (some) animal groups, Behavioural Processes, 141 (2017), pp. 141 151.
 The Cognition of Fish.
- [74] C. C. IOANNOU, F. ROCQUE, J. E. HERBERT-READ, C. DUFFIELD, AND J. A. FIRTH, Predators attacking virtual prey reveal the costs and benefits of leadership, Proceedings of the National Academy of Sciences, 116 (2019), pp. 8925–8930.
- [75] J. JAFFE AND C. SCHURGERS, Sensor networks of freely drifting autonomous underwater explorers, vol. 2006, 01 2006, pp. 93–96.
- [76] J. S. JAFFE, P. J. S. FRANKS, P. L. D. ROBERTS, D. MIRZA, C. SCHURGERS, R. KASTNER, AND A. BOCH, A swarm of autonomous miniature underwater robot drifters for exploring submesoscale ocean dynamics, Nature Communications, 8 (2017), p. 14189.
- [77] P. JAIN AND B. GOEL, Shedding of vortices behind a circular cylinder, Computers Fluids, 4 (1976), pp. 137 – 142.
- [78] J. JANSSEN, *Toxicity of co2+: Implications for lateral line studies*, Journal of comparative physiology. A, Sensory, neural, and behavioral physiology, 186 (2000), pp. 957–60.

- [79] J. JANSSEN AND J. CORCORAN, Distance determination via the lateral line in the mottled sculpin, Copeia, 1998 (1998), pp. 657–662.
- [80] J. JANSSEN, W. R. JONES, A. WHANG, AND P. OSHEL, Use of the lateral line in particulate feeding in the dark by juvenile alewife (alosa pseudoharengus), Canadian Journal of Fisheries and Aquatic Sciences, 52 (1995), pp. 358–363.
- [81] J. JANSSEN, V. SIDELEVA, AND H. BIGA, Use of the lateral line for feeding in two lake baikal sculpins, Journal of Fish Biology, 54 (1999), pp. 404–416.
- [82] M. JI, Y. ZHANG, X. ZHENG, G. LIU, AND J. QIU, A fish-shaped minimal prototype of lateral line system based on pressure sensing, in 2017 IEEE International Conference on Mechatronics and Automation (ICMA), 2017, pp. 596–601.
- [83] Y. JIANG, J. FU, D. ZHANG, AND Y. ZHAO, Investigation on the lateral line systems of two cavefish: Sinocyclocheilus macrophthalmus and s. microphthalmus (cypriniformes: Cyprinidae), Journal of Bionic Engineering, 13 (2016), pp. 108–114.
- [84] Y. JIANG, Z. MA, J. FU, AND D. ZHANG, Development of a flexible artificial lateral line canal system for hydrodynamic pressure detection, Sensors, 17 (2017), p. 1220.
- [85] J. M. JØRGENSEN, On the fine structure of lateral-line canal organs of the herring (clupea harengus), Journal of the Marine Biological Association of the United Kingdom, 65 (1985), pp. 751–758.
- [86] S. KALANTAR AND U. ZIMMER, Distributed shape control of homogeneous swarms of autonomous underwater vehicles, Auton. Robots, 22 (2007), pp. 37–53.
- [87] A. M. KAMAT, Y. PEI, AND A. G. KOTTAPALLI, Bioinspired cilia sensors with graphene sensing elements fabricated using 3d printing and casting, Nanomaterials, 9 (2019).
- [88] M. J. KANTER AND S. COOMBS, Rheotaxis and prey detection in uniform currents by lake michigan mottled sculpin (cottus bairdi), Journal of Experimental Biology, 206 (2003), pp. 59–70.
- [89] H. E. KARLSEN AND O. SAND, Selective and reversible blocking of the lateral line in freshwater fish, Journal of Experimental Biology, 133 (1987), pp. 249–262.
- [90] E. KELASIDI, P. LILJEBACK, K. Y. PETTERSEN, AND J. T. GRAVDAHL, Innovation in underwater robots: Biologically inspired swimming snake robots, IEEE Robotics Automation Magazine, 23 (2016), pp. 44–62.
- [91] A. KLEIN AND H. BLECKMANN, Determination of object position, vortex shedding frequency and flow velocity using artificial lateral line canals, Beilstein journal of nanotechnology, 2 (2011), pp. 276–283.

21977440[pmid].

- [92] A. KONINGS, Malawi cichlids in their natural habitat, 5th edn cichlid press, El Paso, Texas.[Google Scholar], (2016).
- [93] A. G. P. KOTTAPALLI, M. ASADNIA, H. HANS, J. MIAO, AND M. TRIANTAFYLLOU, Harbor seal inspired mems artificial micro-whisker sensor, in 2014 IEEE 27th International Conference on Micro Electro Mechanical Systems (MEMS), 2014, pp. 741–744.
- [94] A. G. P. KOTTAPALLI, M. ASADNIA, J. MIAO, AND M. TRIANTAFYLLOU, Touch at a distance sensing: lateral-line inspired MEMS flow sensors, Bioinspiration & Biomimetics, 9 (2014), p. 046011.
- [95] A. G. P. KOTTAPALLI, M. ASADNIA, J. M. MIAO, G. BARBASTATHIS, AND M. S. TRI-ANTAFYLLOU, A flexible liquid crystal polymer MEMS pressure sensor array for fish-like underwater sensing, Smart Materials and Structures, 21 (2012), p. 115030.
- [96] A. G. P. KOTTAPALLI, M. ASADNIA, Z. SHEN, V. SUBRAMANIAM, J. MIAO, AND M. TRI-ANTAFYLLOU, Mems artificial neuromast arrays for hydrodynamic control of soft-robots, in 2016 IEEE 11th Annual International Conference on Nano/Micro Engineered and Molecular Systems (NEMS), 2016, pp. 504–507.
- [97] A. G. P. KOTTAPALLI, M. BORA, M. ASADNIA, J. MIAO, S. VENKATRAMAN, AND M. TRI-ANTAFYLLOU, Nanofibril scaffold assisted mems artificial hydrogel neuromasts for enhanced sensitivity flow sensing, Scientific Reports, 6 (2016), p. 19336.
- [98] N. KOTTEGE, Underwater Acoustic Localisation in the context of Autonomous Submersibles, PhD thesis, 06 2009.
- [99] A. B. KROESE AND N. A. SCHELLART, Velocity- and acceleration-sensitive units in the trunk lateral line of the trout, Journal of Neurophysiology, 68 (1992), pp. 2212–2221.
 PMID: 1491267.
- [100] C. LEXER, R. A. RANDELL, AND L. H. RIESEBERG, Experimental hybridization as a tool for studying selection in the wild, Ecology, 84 (2003), pp. 1688–1699.
- [101] G. LI, X. CHEN, F. ZHOU, Y. LIANG, Y. XIAO, X. CAO, Z. ZHANG, M. ZHANG, B. WU, S. YIN, ET AL., Self-powered soft robot in the mariana trench, Nature, 591 (2021), pp. 66–71.
- [102] J. C. LIAO, The role of the lateral line and vision on body kinematics and hydrodynamic preference of rainbow trout in turbulent flow, Journal of Experimental Biology, 209 (2006), pp. 4077–4090.

- [103] J. C. LIAO, A review of fish swimming mechanics and behaviour in altered flows, Philosophical Transactions of the Royal Society B: Biological Sciences, 362 (2007), pp. 1973–1993.
- [104] M. LISTAK, G. MARTIN, D. PUGAL, A. AABLOO, AND M. KRUUSMAA, Design of a semiautonomous biomimetic underwater vehicle for environmental monitoring, in 2005 International Symposium on Computational Intelligence in Robotics and Automation, 2005, pp. 9–14.
- [105] G. LIU, S. GAO, T. SARKODIE-GYAN, AND Z. LI, A novel biomimetic sensor system for vibration source perception of autonomous underwater vehicles based on artificial lateral lines, 29 (2018), p. 125102.
- [106] E. LLOYD, C. OLIVE, B. A. STAHL, J. B. JAGGARD, P. AMARAL, E. R. DUBOUÉ, AND A. C. KEENE, Evolutionary shift towards lateral line dependent prey capture behavior in the blind mexican cavefish, Developmental Biology, 441 (2018), pp. 328 337. Cavefish Development.
- [107] Z. MA, Y. JIANG, P. WU, Y. XU, X. HU, Z. GONG, AND D. ZHANG, Constriction canal assisted artificial lateral line system for enhanced hydrodynamic pressure sensing, Bioinspiration & Biomimetics, 14 (2019), p. 066004.
- [108] D. MAALOUF, I. TAMANAJA, E. CAMPOS, A. CHEMORI, V. CREUZE, J. TORRES, AND R. LOZANO, From pd to nonlinear adaptive depth-control of a tethered autonomous underwater vehicle, IFAC Proceedings Volumes, 46 (2013), pp. 743 – 748.
 5th IFAC Symposium on System Structure and Control.
- [109] M. A. MACIVER, E. FONTAINE, AND J. W. BURDICK, Designing future underwater vehicles: principles and mechanisms of the weakly electric fish, IEEE Journal of Oceanic Engineering, 29 (2004), pp. 651–659.
- [110] A. E. MAGURRAN, The adaptive significance of schooling as an anti-predator defence in fish, Annales Zoologici Fennici, 27 (1990), pp. 51–66.
- [111] M. MALINSKY AND W. SALZBURGER, Environmental context for understanding the iconic adaptive radiation of cichlid fishes in lake malawi, Proceedings of the National Academy of Sciences, 113 (2016), pp. 11654–11656.
- [112] M. MALINSKY, H. SVARDAL, A. M. TYERS, E. A. MISKA, M. J. GENNER, G. F. TURNER, AND R. DURBIN, Whole-genome sequences of malawi cichlids reveal multiple radiations interconnected by gene flow, Nature Ecology & Evolution, 2 (2018), pp. 1940–1955.
- [113] P. MANNAM AND P. KRISHNANKUTTY, Biological Propulsion Systems for Ships and Underwater Vehicles, 10 2019.

- [114] B. MANSOURI, A. MALEKI, S. A. JOHARI, AND N. RESHAHMANISH, Effects of cobalt oxide nanoparticles and cobalt ions on gill histopathology of zebrafish (danio rerio), AACL Bioflux, 8 (2015), pp. 438–444.
- [115] S. MARRAS, S. S. KILLEN, J. LINDSTRÖM, D. J. MCKENZIE, J. F. STEFFENSEN, AND P. DOMENICI, Fish swimming in schools save energy regardless of their spatial position, Behavioral Ecology and Sociobiology, 69 (2015), pp. 219–226.
- [116] M. E. MCCONNEY, N. CHEN, D. LU, H. A. HU, S. COOMBS, C. LIU, AND V. V. TSUKRUK, Biologically inspired design of hydrogel-capped hair sensors for enhanced underwater flow detection, Soft Matter, 5 (2009), pp. 292–295.
- [117] M. J. MCHENRY, K. E. FEITL, J. A. STROTHER, AND W. J. VAN TRUMP, Larval zebrafish rapidly sense the water flow of a predator's strike, Biology letters, 5 (2009), pp. 477–479. 19324627[pmid].
- [118] L. M. MEDINA, C. GARCIA, A. F. URBINA, J. MANJARREZ, AND A. MOYAHO, Female vibration discourages male courtship behaviour in the amarillo fish (girardinichthys multiradiatus), Behavioural Processes, 100 (2013), pp. 163–168.
- [119] P. J. MEKDARA, M. A. B. SCHWALBE, L. L. COUGHLIN, AND E. D. TYTELL, The effects of lateral line ablation and regeneration in schooling giant danios, Journal of Experimental Biology, 221 (2018).
- [120] S. MINTCHEV, E. DONATI, S. MARRAZZA, AND C. STEFANINI, Mechatronic design of a miniature underwater robot for swarm operations, in 2014 IEEE International Conference on Robotics and Automation (ICRA), 2014, pp. 2938–2943.
- [121] D. MIRZA AND C. SCHURGERS, Collaborative localization for fleets of underwater drifters, in OCEANS 2007, 2007, pp. 1–6.
- [122] J. MOGDANS AND I. NAUROTH, The oscar, astronotus ocellatus, detects and discriminates dipole stimuli with the lateral line system, Journal of comparative physiology. A, Neuroethology, sensory, neural, and behavioral physiology, 197 (2011), pp. 959–68.
- [123] J. MONTGOMERY AND A. CARTON, The senses of fish: Chemosensory, visual and octavolateralis, 01 2008, pp. 3–31.
- [124] J. MONTGOMERY, F. MCDONALD, C. BAKER, A. CARTON, AND N. LING, Sensory integration in the hydrodynamic world of rainbow trout, Proc. R. Soc. Lond. B, 270 (2003), pp. S195–S197.
- [125] J. MONTGOMERY AND N. PANKHURST, Sensory physiology, in Deep-Sea Fishes, D. J. Randall and A. P. Farrell, eds., vol. 16 of Fish Physiology, Academic Press, 1997, pp. 325-349.

- [126] J. C. MONTGOMERY, Lateral line detection of planktonic prey, in The Mechanosensory Lateral Line, S. Coombs, P. Görner, and H. Münz, eds., New York, NY, 1989, Springer New York, pp. 561–574.
- [127] J. C. MONTGOMERY, C. F. BAKER, AND A. G. CARTON, The lateral line can mediate rheotaxis in fish, Nature, 389 (1997), pp. 960–963.
- [128] J. C. MONTGOMERY AND R. C. MILTON, Use of the lateral line for feeding in the torrentfish (cheimarrichthys fosteri), New Zealand Journal of Zoology, 20 (1993), pp. 121–125.
- [129] C. MORICONI, G. CUPERTINO, S. BETTI, AND M. TABACCHIERA, Hybrid acoustic / optic communications in underwater swarms, in OCEANS 2015 - Genova, 2015, pp. 1–9.
- [130] I. NAUROTH AND J. MOGDANS, Goldfish and oscars have comparable responsiveness to dipole stimuli, Die Naturwissenschaften, 96 (2009), pp. 1401–9.
- [131] J. NELSON, T. GRANDE, AND M. WILSON, Fishes of the World, Fifth Edition, 03 2016.
- [132] A. W. NOLTE AND H. D. SHEETS, Shape based assignment tests suggest transgressive phenotypes in natural sculpin hybrids (teleostei, scorpaeniformes, cottidae), Frontiers in Zoology, 2 (2005), p. 11.
- [133] F. OLEARI, D. LODI RIZZINI, F. KALLASI, J. ALEOTTI, AND S. CASELLI, Issues in high performance vision systems design for underwater interventions, 10 2016.
- [134] C. OSTERLOH, T. PIONTECK, AND E. MAEHLE, Monsun ii: A small and inexpensive auv for underwater swarms, in ROBOTIK 2012; 7th German Conference on Robotics, 2012, pp. 1–6.
- [135] S. PALANI, Toxicological effect of cobalt chloride on freshwater fish oreochromis mossambicus, Journal of Advanced Applied Scientific Research, 1 (2015), pp. 331–340.
- [136] B. PARTRIDGE AND T. PITCHER, The sensory basis of fish schools: Relative roles of lateral line and vision, Journal of comparative physiology, 135 (1980), pp. 315–325.
- [137] D. PAVLOV, A. KASUMYAN, ET AL., Patterns and mechanisms of schooling behavior in fish: a review, Journal of Ichthyology, 40 (2000), p. S163.
- [138] S. PELESHANKO, M. JULIAN, M. ORNATSKA, M. MCCONNEY, M. LEMIEUX, N. CHEN, C. TUCKER, Y. YANG, C. LIU, J. HUMPHREY, AND V. TSUKRUK, Hydrogel-encapsulated microfabricated haircells mimicking fish cupula neuromast, Advanced Materials, 19 (2007), pp. 2903–2909.

- [139] A. PÉREZ-ESCUDERO, J. VICENTE-PAGE, R. C. HINZ, S. ARGANDA, AND G. G. DE POLAVIEJA, idtracker: tracking individuals in a group by automatic identification of unmarked animals, Nature Methods, 11 (2014), pp. 743–748.
- [140] S. B. PICKETT, E. D. THOMAS, J. Y. SEBE, T. LINBO, R. ESTERBERG, D. W. HAILEY, AND D. W. RAIBLE, Cumulative mitochondrial activity correlates with ototoxin susceptibility in zebrafish mechanosensory hair cells, Elife, 7 (2018), p. e38062.
- [141] T. PITCHER AND B. PARTRIDGE, Fish school density and volume, Marine Biology, 54 (1979), pp. 383–394.
- [142] T. PITCHER, B. PARTRIDGE, AND C. WARDLE, A blind fish can school, Science, 194 (1976), pp. 963–965.
- [143] T. J. PITCHER, Heuristic definitions of fish shoaling behaviour., Animal Behaviour, 31 (1983), pp. 611–613.
- [144] T. J. PITCHER, Functions of Shoaling Behaviour in Teleosts, Springer US, Boston, MA, 1986, pp. 294–337.
- [145] V. PÄRSSINEN, K. HULTHÉN, C. BRÖNMARK, C. SKOV, J. BRODERSEN, H. BAKTOFT, B. B. CHAPMAN, L.-A. HANSSON, AND P. A. NILSSON, Maladaptive migration behaviour in hybrids links to predator-mediated ecological selection, Journal of Animal Ecology, 89 (2020), pp. 2596–2604.
- [146] R CORE TEAM, R: A Language and Environment for Statistical Computing, R Foundation for Statistical Computing, Vienna, Austria, 2020.
- [147] A. R. RAZALI AND Y. QIN, A review on micro-manufacturing, micro-forming and their key issues, Procedia Engineering, 53 (2013), pp. 665–672.
 - Malaysian Technical Universities Conference on Engineering amp;amp; Technology 2012, MUCET 2012.
- [148] M. REN, C. RINDT, AND A. STEENHOVEN, VAN, 3d vortices in the wake flow behind a heated cylinder, in Eurotherm 74 on Heat Transfer in Unsteady and Transitional Flows, H. Lange, de and A. Steenhoven, van, eds., Eindhoven University of Technology, 2003, pp. 141–146.
- [149] L. H. RIESEBERG, M. A. ARCHER, AND R. K. WAYNE, Transgressive segregation, adaptation and speciation, Heredity, 83 (1999), pp. 363–372.
- [150] R. L. ROBINSON AND G. F. TURNER, Comparison of the social behaviour of an endemic lake malawi cichlid in the field and laboratory, Journal of Fish Biology, 36 (1990), pp. 615–616.

- [151] M. ROMENSKYY, J. HERBERT-READ, C. IOANNOU, A. SZORKOVSZKY, A. WARD, AND D. SUMPTER, Quantifying the structure and dynamics of fish shoals under predation threat in three dimensions, Behavioral Ecology, 31 (2019), p. arz197.
- [152] D. ROWE, T. DEAN, E. WILLIAMS, AND J. SMITH, Effects of turbidity on the ability of juvenile rainbow trout, oncorhynchus mykiss, to feed on limnetic and benthic prey in laboratory tanks, New Zealand Journal of Marine and Freshwater Research - N Z J MAR FRESHWATER RES, 37 (2003), pp. 45–52.
- [153] S. G. RUBIN, *Incompressible flow along a corner*, Journal of Fluid Mechanics, 26 (1966), p. 97–110.
- [154] N. SAEED, A. CELIK, T. Y. AL-NAFFOURI, AND M.-S. ALOUINI, Underwater optical wireless communications, networking, and localization: A survey, Ad Hoc Networks, 94 (2019), p. 101935.
- [155] S. S. SAEEDI SARAVI, S. KARAMI, B. KARAMI, AND M. SHOKRZADE, Toxic effects of cobalt chloride on hematological factors of common carp (cyprinus carpio), Biological trace element research, 132 (2009), pp. 144–52.
- [156] E. ŞAHIN AND A. WINFIELD, Special issue on swarm robotics, Swarm Intelligence, 2 (2008), pp. 69–72.
- [157] T. SALUMÄE AND M. KRUUSMAA, Flow-relative control of an underwater robot, Proceedings of the Royal Society A: Mathematical, Physical and Engineering Sciences, 469 (2013), p. 20120671.
- [158] W. SALZBURGER, T. MACK, E. VERHEYEN, AND A. MEYER, Out of tanganyika: Genesis, explosive speciation, key-innovations and phylogeography of the haplochromine cichlid fishes, BMC evolutionary biology, 5 (2005), p. 17.
- [159] J. SARGISON, A. BARTON, G. WALKER, AND P. BRANDNER, Design and calibration of a water tunnel for skin friction research, Australian Journal of Mechanical Engineering, 7 (2009), pp. 111–124.
- [160] F. SCHILL, A. BAHR, AND A. MARTINOLI, Vertex: A New Distributed Underwater Robotic Platform for Environmental Monitoring, 03 2018, pp. 679–693.
- [161] T. SCHMICKL, R. THENIUS, C. MOSLINGER, J. TIMMIS, A. TYRRELL, M. READ, J. HILDER, J. HALLOY, A. CAMPO, C. STEFANINI, L. MANFREDI, S. OROFINO, S. KERNBACH, T. DIPPER, AND D. SUTANTYO, *Cocoro – the self-aware underwater swarm*, in 2011 Fifth IEEE Conference on Self-Adaptive and Self-Organizing Systems Workshops, 2011, pp. 120–126.

- [162] A. SCHMITZ, H. BLECKMANN, AND J. MOGDANS, Organization of the superficial neuromast system in goldfish, carassius auratus, Journal of Morphology, 269 (2008), pp. 751–761.
- [163] M. A. SCHWALBE AND J. F. WEBB, Sensory basis for detection of benthic prey in two lake malawi cichlids, Zoology, 117 (2014), pp. 112 – 121.
- [164] M. A. B. SCHWALBE, D. K. BASSETT, AND J. F. WEBB, Feeding in the dark: lateralline-mediated prey detection in the peacock cichlid aulonocara stuartgranti, Journal of Experimental Biology, 215 (2012), pp. 2060–2071.
- [165] M. A. B. SCHWALBE, B. J. SEVEY, AND J. F. WEBB, Detection of artificial water flows by the lateral line system of a benthic feeding cichlid fish, Journal of Experimental Biology, 219 (2016), pp. 1050–1059.
- [166] M. A. B. SCHWALBE AND J. F. WEBB, The effect of light intensity on prey detection behavior in two lake malawi cichlids, aulonocara stuartgranti and tramitichromis sp., Journal of Comparative Physiology A, 201 (2015), pp. 341–356.
- [167] J. S. SCHWARZ, T. REICHENBACH, AND A. J. HUDSPETH, A hydrodynamic sensory antenna used by killifish for nocturnal hunting, Journal of Experimental Biology, 214 (2011), pp. 1857–1866.
- [168] D. SENGUPTA, D. TRAP, AND A. G. P. KOTTAPALLI, Piezoresistive carbon nanofiber-based cilia-inspired flow sensor, Nanomaterials, 10 (2020).
- [169] E. SHAW, The schooling of fishes, Scientific American, 206 (1962), pp. 128–141.
- [170] J. SHINTAKE, V. CACUCCIOLO, H. SHEA, AND D. FLOREANO, Soft biomimetic fish robot made of dielectric elastomer actuators, Soft Robotics, 5 (2018), pp. 466–474.
 PMID: 29957131.
- [171] J. SHINTAKE, D. ZAPPETTI, T. PETER, Y. IKEMOTO, AND D. FLOREANO, Bio-inspired tensegrity fish robot, in 2020 IEEE International Conference on Robotics and Automation (ICRA), 2020, pp. 2887–2892.
- [172] M. SHOAIB, N. H. HAMID, A. F. MALIK, N. B. ZAIN ALI, AND M. TARIQ JAN, A review on key issues and challenges in devices level mems testing, Journal of Sensors, 2016 (2016).
- [173] J. SNOEKS, G. CARVALHO, AND G. L. M. B. C. PROJECT, The Cichlid Diversity of Lake Malawi/Nyasa/Niassa: Identification, Distribution and Taxonomy, Cichlid Press, 2004.
- [174] J. SONG, H. Y. YAN, AND A. N. POPPER, Damage and recovery of hair cells in fish canal (but not superficial) neuromasts after gentamicin exposure, Hearing Research, 91 (1995), pp. 63–71.

- [175] V. A. SOVRANO, D. POTRICH, A. FOÀ, AND C. BERTOLUCCI, Extra-visual systems in the spatial reorientation of cavefish, Scientific Reports, 8 (2018), p. 17698.
- [176] R. R. STEPHENS, The lateral line system of the gizzard shad, dorosoma cepedianum lesueur (pisces: Clupeidae), Copeia, 1985 (1985), pp. 540–556.
- [177] W. J. STEWART, J. L. JOHANSEN, AND J. C. LIAO, A non-toxic dose of cobalt chloride blocks hair cells of the zebrafish lateral line, Hearing Research, 350 (2017), pp. 17–21.
- [178] A. SULI, G. M. WATSON, E. W. RUBEL, AND D. W. RAIBLE, Rheotaxis in larval zebrafish is mediated by lateral line mechanosensory hair cells, PLOS ONE, 7 (2012), pp. 1–6.
- [179] D. SUTANTYO AND P. LEVI, Decentralized underwater multi-robot communication using bio-inspired approaches, Artificial Life and Robotics, 20 (2015), pp. 152–158.
- [180] H. SVARDAL, F. X. QUAH, M. MALINSKY, B. P. NGATUNGA, E. A. MISKA, W. SALZBURGER, M. J. GENNER, G. F. TURNER, AND R. DURBIN, Ancestral Hybridization Facilitated Species Diversification in the Lake Malawi Cichlid Fish Adaptive Radiation, Molecular Biology and Evolution, 37 (2019), pp. 1100–1113.
- [181] S. A. TADIGADAPA AND N. NAJAFI, Developments in microelectromechanical systems (mems): A manufacturing perspective, Journal of Manufacturing Science and Engineering, 125 (2003), pp. 816–823.
- [182] Z. TANG, Z. WANG, J. LU, G. MA, AND P. ZHANG, Underwater robot detection system based on fish's lateral line, Electronics, 8 (2019).
- [183] H. TERMARSCH AND J. WARD, Body-generated hydrodynamic flows influence male-male contests and female mate choice in a freshwater fish, Animal Behaviour, 169 (2020), pp. 119–128.
- [184] L.-G. TRAN AND W.-T. PARK, Biomimetic flow sensor for detecting flow rate and direction as an application for maneuvering autonomous underwater vehicle, International Journal of Precision Engineering and Manufacturing-Green Technology, (2020).
- [185] E. TREWAVAS, Tilapiine fishes of the genera sarotherodon, oreochromis and danakilia, (1983).
- [186] V. C. TWITTY, Second-generation hybrids of the species of taricha, Proceedings of the National Academy of Sciences, 47 (1961), pp. 1461–1486.
- [187] W. J. VAN TRUMP, S. COOMBS, K. DUNCAN, AND M. J. MCHENRY, Gentamicin is ototoxic to all hair cells in the fish lateral line system, Hearing research, 261 (2010), p. 42–50.
- [188] B. VENABLES AND B. RIPLEY, Modern Applied Statistics With S, 01 2002.

- [189] R. VENTURELLI, O. AKANYETI, F. VISENTIN, J. JEŽOV, L. D. CHAMBERS, G. TOMING, J. BROWN, M. KRUUSMAA, W. M. MEGILL, AND P. FIORINI, Hydrodynamic pressure sensing with an artificial lateral line in steady and unsteady flows, Bioinspiration & Biomimetics, 7 (2012), p. 036004.
- [190] R. VOIGT, A. CARTON, AND J. MONTGOMERY, Responses of anterior lateral line afferent neurones to water flow, Journal of Experimental Biology, 203 (2000), pp. 2495–2502.
- [191] E.-J. WAGENMAKERS AND S. FARRELL, Aic model selection using akaike weights, Psychonomic Bulletin & Review, 11 (2004), pp. 192–196.
- [192] W. WANG, X. ZHANG, J. ZHAO, AND G. XIE, Sensing the neighboring robot by the artificial lateral line of a bio-inspired robotic fish, 09 2015.
- [193] A. R. WARK, M. G. MILLS, L.-H. DANG, Y. F. CHAN, F. C. JONES, S. D. BRADY, D. M. ABSHER, J. GRIMWOOD, J. SCHMUTZ, R. M. MYERS, D. M. KINGSLEY, AND C. L. PEICHEL, Genetic architecture of variation in the lateral line sensory system of threespine sticklebacks, G3 (Bethesda, Md.), 2 (2012), pp. 1047–1056. 22973542[pmid].
- [194] J. F. WEBB, Gross morphology and evolution of the mechanoreceptive lateral-line system in teleost fishes., Brain, behavior and evolution, 33 1 (1989), pp. 34–53.
- [195] J. F. WEBB, Morphological diversity, development, and evolution of the mechanosensory lateral line system, in The lateral line system, Springer, 2013, pp. 17–72.
- [196] J. F. WEBB AND J. B. RAMSAY, New Interpretation of the 3-D Configuration of Lateral Line Scales and the Lateral Line Canal Contained within Them, Copeia, 105 (2017), pp. 339 – 347.
- [197] J. F. WEBB AND J. E. SHIREY, Postembryonic development of the cranial lateral line canals and neuromasts in zebrafish, Developmental dynamics: an official publication of the American Association of Anatomists, 228 (2003), pp. 370–385.
- [198] B. WIESMAYR, M. HÖGLINGER, M. KRIEGER, P. LINDNER, W. BAUMGARTNER, AND A. T. STADLER, A polydimethylsiloxane (pdms) waveguide sensor that mimics a neuromast to measure fluid flow velocity, Sensors, 19 (2019).
- [199] J. WILLIS, Wake sorting, selective predation and biogenic mixing: potential reasons for high turbulence in fish schools, PeerJ, 1 (2013), pp. e96–e96.
 23825796[pmid].
- [200] S. P. WINDSOR AND M. J. MCHENRY, The influence of viscous hydrodynamics on the fish lateral-line system, Integrative and comparative biology, 49 (2009), pp. 691–701.

- [201] B. J. WOLF, J. A. S. MORTON, W. N. MACPHERSON, AND S. M. VAN NETTEN, Bio-inspired all-optical artificial neuromast for 2d flow sensing, Bioinspiration & Biomimetics, 13 (2018), p. 026013.
- [202] B. J. WOLF, P. PIRIH, M. KRUUSMAA, AND S. M. VAN NETTEN, Shape classification using hydrodynamic detection via a sparse large-scale 2d-sensitive artificial lateral line, IEEE Access, 8 (2020), pp. 11393–11404.
- [203] R. B. WYNN, V. A. HUVENNE, T. P. LE BAS, B. J. MURTON, D. P. CONNELLY, B. J. BETT, H. A. RUHL, K. J. MORRIS, J. PEAKALL, D. R. PARSONS, E. J. SUMNER, S. E. DARBY, R. M. DORRELL, AND J. E. HUNT, Autonomous underwater vehicles (auvs): Their past, present and future contributions to the advancement of marine geoscience, Marine Geology, 352 (2014), pp. 451 – 468.
 50th Anniversary Special Issue.
- [204] D. XU, Z. LV, H. ZENG, H. BESSAIH, AND B. SUN, Sensor placement optimization in the artificial lateral line using optimal weight analysis combining feature distance and variance evaluation, ISA Transactions, 86 (2019), pp. 110–121.
- [205] Y. XU AND K. MOHSENI, A pressure sensory system inspired by the fish lateral line: Hydrodynamic force estimation and wall detection, IEEE Journal of Oceanic Engineering, 42 (2017), pp. 532–543.
- [206] Y. YANG, J. CHEN, J. ENGEL, S. PANDYA, N. CHEN, C. TUCKER, S. COOMBS, D. L. JONES, AND C. LIU, Distant touch hydrodynamic imaging with an artificial lateral line, Proceedings of the National Academy of Sciences, 103 (2006), pp. 18891–18895.
- [207] Y. YANG, N. NGUYEN, N. CHEN, M. LOCKWOOD, C. TUCKER, H. HU, H. BLECKMANN, C. LIU, AND D. JONES, Artificial lateral line with biomimetic neuromasts to emulate fish sensing, Bioinspiration biomimetics, 5 (2010), p. 16001.
- [208] W.-K. YEN, C.-F. HUANG, H.-R. CHANG, AND J. GUO, Localization of a leading robotic fish using a pressure sensor array on its following vehicle, Bioinspiration & Biomimetics, 16 (2020), p. 016007.
- [209] M. ZAPETIS AND A. SZESCIORKA, Cetacean Navigation, 01 2018, pp. 1–7.
- [210] X. ZHANG, X. SHAN, Z. SHEN, T. XIE, AND J. MIAO, A new self-powered sensor using the radial field piezoelectric diaphragm in d33 mode for detecting underwater disturbances, Sensors, 19 (2019).
- [211] X. ZHENG, C. WANG, R. FAN, AND G. XIE, Artificial lateral line based local sensing between two adjacent robotic fish, Bioinspiration & Biomimetics, 13 (2017), p. 016002.